In compliance with the
Canadian Privacy Legislation
some supporting forms
may have been removed from
this dissertation.

While these forms may be included
in the document page count,
their removal does not represent
any loss of content from the dissertation.

MONTE CARLO STUDY OF ION CHAMBER RESPONSE IN LOW ENERGY PHOTON BEAMS

by

FADI HOBEILA

Medical Physics Unit
McGill University, Montreal
February 2003

A thesis submitted to McGill University
in partial fulfilment of the requirements
of the degree of Master of Science

Your file Votre référence
ISBN: 0-612-88213-6
Our file Notre référence
ISBN: 0-612-88213-6

Abstract

^{192}Ir is one of the most popular radiation sources used for brachytherapy treatments. However, ^{192}Ir emits a wide photon spectrum (10 keV to 900 keV) which impedes the creation of an ^{192}Ir primary standard. The ^{192}Ir air kerma calibration factor is derived by interpolating between ^{60}Co, ^{137}Cs and hard orthovoltage air kerma calibration factors obtained from a standards laboratory. The EGSnrc Monte Carlo package was used to calculate the response in low energy photon beams of a commercial parallel-plate chamber to assess useability as a ^{192}Ir and kilovoltage photon beam calibration tool. XCOM photoeffect cross-sections were implemented in EGSnrc to improve kerma calculation agreement at low energies. The response calculations were compared to experimental data from PTB (Germany). Overall, agreement between calculations and measurement is good and represents an improvement to results from the literature. However, discrepancies exist at the lowest energies which may be caused by differences in the measurement and calculation geometries.

Résumé

L'^{192}Ir est une source de radiation dont l'utilisation en curiethérapie est répandue. Malgré cela, aucun étalon primaire n'est disponible pour la calibration de l'^{192}Ir. Le facteur de calibration de l'^{192}Ir est obtenu par interpolation des facteurs du ^{137}Cs, ^{60}Co et de faisceaux de rayons X de basses énergies. Le logiciel Monte Carlo EGSnrc fut utilisé afin de calculer la courbe de réponse en basses énergies d'une chambre à ionisation commerciale et de jauger son utilité pour la calibration d'^{192}Ir et de faisceaux de photons de basses énergies. Les sections efficaces de l'effet photoélectrique provenant de la base de données XCOM furent implantées dans EGSnrc pour améliorer l'accord des calculs de kerma en basses énergies. Les calculs de réponses furent comparés aux données expérimentales provenant de PTB (Allemagne). En général, l'accord entre les calculs et les mesures est bon et représente une amélioration par rapport aux résultats de la littérature.

Acknowledgements

I would like to thank my supervisor Dr Jan P. Seuntjens for his unending support through thick and thin. His endless patience and enlightened guidance are deeply appreciated. My gratitude also goes to Dr Ervin B. Podgorsak who strives to get the best out of his students but also helps them become better persons.

I would like to thank Standard Imaging for providing the geometry of the Exradin A11 parallel-plate chamber. Dr Ludwig Buërmann (Physikalisch-Technische Bundesanstalt) for providing the ion chamber response measurements of the Exradin A11 and the PTB kilovoltage X-ray spectra.

I would like to thank Dr Francois Deblois and Wamied Abdel-Rahman whom assistance on Monte Carlo matters was important; Kamen Paskalev my mentor and friend whose insights on physics (and life) were in invaluable; Yanic Bercier for his programming help and friendship and my fellow students who've supported me all along.

This thesis is dedicated to my parents Jean and Lisette Hobeila who have always believed in me and gave me so much support over the years.

A warm shout out to my brothers (Sach, Ximeng, JoelDrole) without whom life would not be as good.

Infinite TLC goes to Anaick my love without whom I would not have a reason to live.

Anaick, I'm home!

Table of contents

List of figures and tables

Chapter 1

Introduction

1. Radiation therapy

The use of ionizing radiation is of one the main three methods in the treatment of cancer. The aim of radiation therapy is to deliver a prescribed dose to a tumour through the use of ionizing radiation while sparing healthy tissues surrounding the tumour.

Ionizing radiation is of two types: directly or indirectly ionizing. Directly ionizing radiation deposit energy directly into a medium by ionizing the medium's atoms through Coulomb interactions. This implies that only charged particles like electrons, positrons and protons can ionize matter directly. Neutral particles like photons and neutrons can only ionize matter through the production of directly ionizing radiation and so are qualified as indirectly ionizing radiation.

Ionizing radiation provokes biological cellular effects. The ionization of cellular water molecules results in the production of free radicals which can damage DNA. Direct ionization of DNA molecules is possible and often creates double-strand breaks in the DNA which renders the DNA impossible to repair. Damage induced to DNA molecules of a cell can result in cellular mutation and/or cellular death.

The most commonly used types of ionizing radiation for the treatment of cancer are photons and electrons. Delivery of ionizing radiation to a tumour is done through external beam radiotherapy or brachytherapy. External beam radiotherapy is the most widely used delivery method. External photon beam radiotherapy is possible over a wide range of

photon energies which suit particular needs. High energy photon beams, ^{60}Co (average photon energy=1.25 MeV) or higher energies, are used to treat deep seated tumors while orthovoltage photon beams (300 kV or less) are used to treat surface or low-lying tumours.

Brachytherapy is the clinical use of small encapsulated radioactive sources at a short distance from or inserted in the target volume for irradiation of malignant tumors or non-malignant lesions. It plays an important role in the treatment of cancers of several sites, including the brain, head and neck, uterine cervix and prostate. Recently, there has been growing interest in using brachytherapy for reducing restenosis after angioplasty treatment for vascular diseases.

2. *Radiation dosimetry*

Radiation dosimetry is interested in the measurement of relevant dosimetric quantities such as dose (energy absorbed per unit mass) or kerma (energy transferred per unit mass). Dosimeters are categorized as either reference dosimeters or relative dosimeters. A reference dosimeter when suitably calibrated can measure dose or absorbed dose in a given volume of material in absolute terms, while a relative dosimeter is used to measure the variation of absorbed dose relative to some reference point.

There are few dosimeters that qualify as absolute dosimeters. The most absolute dosimeter is the calorimeter because it is the only dosimeter which can be fully characterized without the use of ionizing radiation. Other reference dosimeters rely on the knowledge of different parameters which can be determined only in a radiation field. For example, free-air ionization chambers and cavity ionization chambers rely on the mean

energy necessary to create an ion pair in air $\left(\bar{W}/e\right)_{air}$ to determine kerma while Fricke dosimeters rely on the knowledge of the radiation chemical yield G.

Clinically important relative dosimeters are cavity ionization chambers, films, diodes and thermoluminescent dosimeters. Ionization chambers are the most widely used dosimeters because of their precision and stability.

In order for the prescribed amount of dose to be delivered to the tumour, it is important to have proper calibration of the source of radiation. Proper calibration of the treatment beams or radiation sources ensures that the prescribed dose for the treatment plan is actually delivered to the patient. Calibration of a radiation source is based on a calibrated dosimeter which is traceable to the primary standards of a standards laboratory. The National Research Council of Canada (NRCC) is the purveyor of ionizing radiation primary standards for Canada.

3. Motivation for this work

Various radionuclides are used as radiation sources for brachytherapy treatments. Some of the more commonly utilized radionuclides are iodine-125 (^{125}I), palladium-103 (^{103}Pd) and iridium-192 (^{192}Ir). The vast majority of interstitial brachytherapy is performed using ^{125}I or ^{192}Ir. ^{192}Ir is also the most employed radionuclide in high dose rate brachytherapy. ^{192}Ir owes its popularity to its relatively high specific activity (~450 Ci/g), its mechanical flexibility (easy to produce wires) and its useful energy range ($h\bar{\nu} \approx 370\ keV$). However, ^{192}Ir has a wide photon energy range from around 10 keV up to 900 keV[1-3] (see Figure 6-1) which impedes the creation of an ^{192}Ir primary standard.

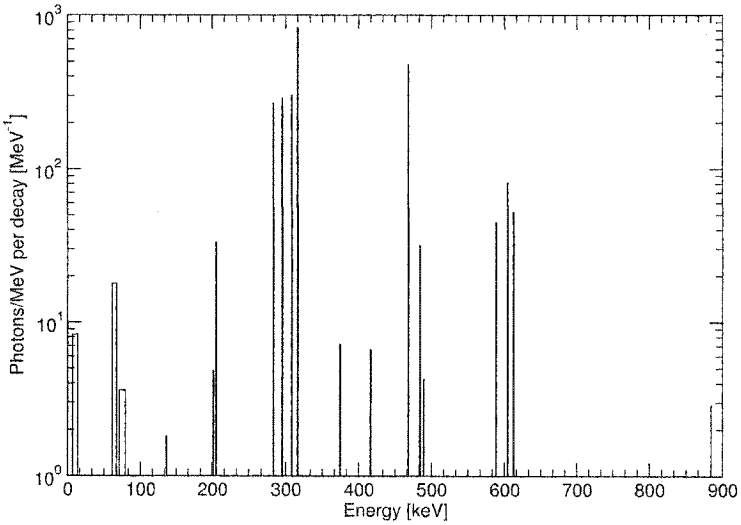

Figure 1-1. ^{192}Ir photon spectrum. Number of photons per bin is normalized by the bin width. Data taken from Duchemin and Coursol, 1993[2].

Air kerma primary standards for low-energy photons are usually based on free-air ionization chambers which directly measure the charge released in air. Free-air chambers can not be used above 300 keV because the range of electrons created would be too long for the dimensions of a free-air chamber[4]. At high energies, air kerma primary standards are based on graphite cavity ionization chambers on the basis of the Spencer-Attix[5] cavity theory. It was shown that for lower photon energies, 3% (at 300 keV) and 30% (at 100 keV) of the dose to the gas of an ion chamber is due to photon interactions in the cavity[6]. These results invalidate the use of Spencer-Attix[5] theory since the first Bragg-Gray condition is not met (see Chapter 4). To summarize, the high energies of the ^{192}Ir spectrum forbid the use of a free-air ionization chamber based air kerma primary standard while the low energies invalidate Spencer-Attix cavity theory, hence the absence of an ^{192}Ir primary standard. To palliate this situation, an interpolative free-air secondary standard method[7, 8] has been developed and is the interim de facto standard for measurement of high intensity ^{192}Ir. The ^{192}Ir air kerma calibration factor is derived by

interpolating between ^{137}Cs and hard orthovoltage air kerma calibration factors obtained from a standards laboratory (see Chapter 4, Section 3.4).

4. *Aim of the thesis*

The use of Monte Carlo simulation software is seen as a way to overcome the difficulties in developing air kerma standards for low energy photon emitters. Monte Carlo methods are described as statistical simulation methods and as such are well suited to reproduce the stochastic nature of particle interactions. Monte Carlo codes can directly simulate particle interactions without making use of cavity theories which are inadequate at low energies. Providing the Monte Carlo software is consistent with basic dosimetry theorems, calculations can provide insight and results when analytical solutions are inadequate.

We will present EGSnrc[9] (Electron Gamma Shower) Monte Carlo calculations of ion chamber response for a commercially available parallel-plate cavity ionization chamber in low energy photon beams. The calculations will be compared to experimental data and we will try to assess the usefulness of commercial parallel-plate chambers for low energy photon beams air kerma measurements as well as test the accuracy of the EGSnrc Monte Carlo code at very low energies.

5. References

[1] Loftus, T.P., Standardization of iridium-192 gamma ray sources in terms of exposure. J. Res. NBS, 1980. **85**: p. 19-25.

[2] Duchemin, B. and N. Coursol, Réévalution de l'^{192}Ir., Technical Note LPRI/93/018, DAMRI, CEA, France (1993).

[3] Borg, J. and D.W.O. Rogers, Monte Carlo calculations of photon spectra in air from ^{192}Ir sources, NRC Report PIRS-629r, (1998).

[4] Attix, F.H., Introduction to radiological physics and radiation dosimetry. 1986, New York: Wiley & Son.

[5] Spencer, L.V. and F.H. Attix, A theory of cavity ionization. Radiat. Res., 1955. **3**: p. 239.

[6] Ma, C.M. and A.E. Nahum, Bragg-Gray theory and ion chamber dosimetry for photon beams. Phys. Med. Biol., 1991. **36**: p. 413-428.

[7] Goetsch, S.J., et al., Calibration of ^{192}Ir high-dose-rate afterloading systems. Med. Phys., 1991. **18**: p. 462-467.

[8] Verhaegen, F., et al., Calibration of low activity ^{192}Ir brachytherapy sources in terms of reference air kerma rate with large volume spherical ionization chambers. Phys. Med. Biol., 1992. **37**: p. 2071-2081.

[9] Kawrakow, I., Accurate condensed history Monte Carlo simulation of electron transport. I. EGSnrc, the new EGS4 version. Med Phys, 2000. **27**(3): p. 485-98.

Chapter 2

Photon interactions with matter

1. Introduction

In this study, photon beams covering a range of energies from a few keV to Cobalt-60 energies ($h\bar{\nu} = 1.25\ MeV$) are used. In this energy range, various interactions are possible between photons and the atoms of a medium. This chapter introduces the different photon interactions applicable to the energy range of focus, specifically, photoelectric absorption (or photoeffect), coherent (Rayleigh) and incoherent (Compton) scattering and pair production. The description of each photon interaction will take place in two steps: (1) a description of the kinematics of the interaction and (2) a description of the probabilistic aspects of the interaction, i.e. interaction cross-sections and dependencies on energy and atomic number of the medium (Z).

2. Kinematics of photon interactions

The interaction of photon with matter results either in the photon being absorbed by the interacting atom or the photon being scattered with or without losing energy.

Photon elastic scattering, scatter with no significant energy transfer, is achieved through coherent scattering and Thomson scattering. Photoelectric absorption and pair production result in a transfer of energy and the absorption of the photon by the atom while incoherent scattering transfers energy to an electron through inelastic collision.

2.1. Rayleigh scattering (coherent scattering)

Rayleigh scattering is the process by which a photon is elastically scattered by a whole atom. The incoming photon drives the electrons of the atom into momentary oscillation. The oscillating electrons emit a wave of the same wavelength as that of the original photon. The scattered wave (photon) is the sum of all the waves radiated by the electrons. Since this is a cooperative process, Rayleigh scattering is also known as coherent scattering.

2.2. Thomson scattering

Thomson scattering is a process by which a photon is scattered by a stationary free electron. The electric field of the incident photon puts the electron in an oscillatory motion and the electron emits the incident energy as dipole radiation. The scattered photon has the same wavelength as the incoming photon. No energy is transferred from the photon to the electron (elastic scattering).

2.3. Photoelectric absorption (photoeffect)

In the photoelectric absorption process, a photon collides with an atom and is absorbed by the atom. An orbital (bound) electron is ejected from the atom and is called a photoelectron. To comply with the laws of conservation of energy and momentum, photoelectric absorption can only take place with a bound electron. An electron is considered *bound* when it's binding energy is comparable to the energy of the incoming photon. Because of this, photoeffect is most probable with inner shell electrons. The kinetic energy T_{e^-} of the photoelectron is equal to the energy of the incoming photon, $h\nu$, minus the necessary energy expended by the electron to free itself from the atom, ψ. In

general, $T_{e^-} = h\nu - |E_b|$ where $|E_b|$ is the binding energy of the electronic shell from which the photoelectron originates.

The ejection angle of photoelectrons is dependent on the photon energy. At low energies ($h\nu \leq 20\ keV$), photoelectrons are ejected at a right angle from the photon's trajectory while at higher energies ($h\nu \geq 1\ MeV$), they are emitted in the forward direction.

The photoeffect interaction leaves the absorbing atom with a vacancy in one of its electronic shells. This vacancy sets the stage to post-interaction processes (relaxations) which are discussed later in this chapter.

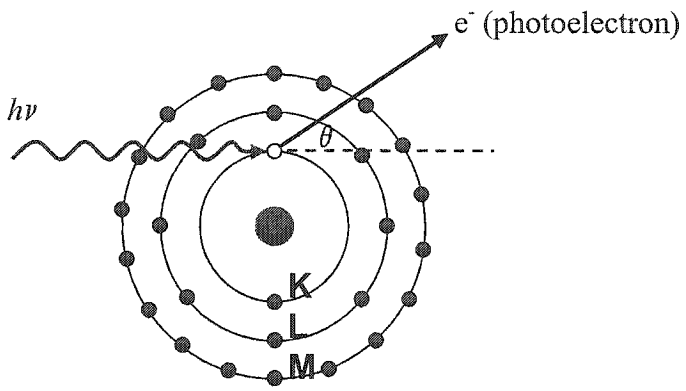

Figure 2-1. Schematic diagram of the photoelectric absorption process. A photon of energy $h\nu$ interacts with a K-shell electron which is emitted with a kinetic energy $T_{e^-} = h\nu - |E_b|$ and angle θ. The net result is the absorption of the incident photon, the emission of a photoelectron and the creation of a vacancy in the K-shell.

2.4. Compton scattering

Compton scattering is the process by which a photon of energy $h\nu$ is scattered off of a free and stationary electron. The electron is considered *free* when the photon's energy is several orders of magnitude greater than its binding energy. Compton effect is an inelastic scattering process since energy is transferred from the photon to the electron. Under this

impulse, the electron recoils from the collision at an angle ϕ with an energy T_{e^-} while the photon is scattered at an angle θ with energy $h\nu$'. Since the photon is scattered by an independent electron, as opposed to coherent scattering, Compton scattering is also called incoherent scattering. As for, photoelectric absorption, a vacancy is created in one of the electronic shells of the atom. Figure 2-2 schematically describes Compton scattering.

The kinematics of Compton scattering are described adequately by the application of the principles of conservation of energy and momentum which give:

$$T_{e^-} = h\nu \frac{\varepsilon(1-\cos\theta)}{1+\varepsilon(1-\cos\theta)} \tag{2.1}$$

$$h\nu' = \frac{h\nu}{1+\varepsilon(1-\cos\theta)} \tag{2.2}$$

$$\cot\varphi = (1+\varepsilon)\tan\frac{\theta}{2} \tag{2.3}$$

Where T_{e^-}, $h\nu$, $h\nu$' are the energies of the recoil electron, the incoming and scattered photon respectively. The parameter ε is the ratio of the energy of the incoming photon to the rest mass of the electron (m_0c^2=0.511 MeV), $\varepsilon = h\nu / m_0c^2$.

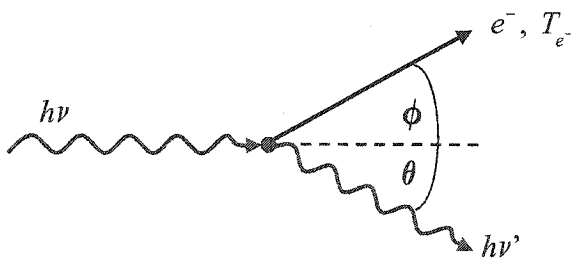

Figure 2-2. Schematic representation of Compton scattering. An incident photon of energy $h\nu$ interacts with a free and stationary electron. The photon is scattered at an angle θ with energy $h\nu$' while the electron recoils at angle ϕ with an energy T_{e^-}.

2.5. Pair production

When a photon passes near the nucleus of an atom and is subjected to the nucleus' strong Coulomb field, it may disappear and an electron-positron pair (e^-, e^+) created (see Figure 2-3). The nucleus recoils to conserve momentum. This interaction is only possible if the photon's energy is greater than the energy needed to create the electron-positron pair. The threshold energy is given by $h\nu_{thresh.} = 2m_o c^2(1+m_o/m_A)$ where m_0 is the rest mass of the electron and m_A is the rest mass of the nucleus. Because the mass of the nucleus is large compared to the electron's, $h\nu_{thresh.} \approx 2m_o c^2 = 1.022\ MeV$.

This process can also occur in the Coulomb field of an orbital electron. The result is the production of an electron-positron pair and the ejection of the orbital electron. Since three particles are produced, this interaction is called *triplet production*. The photon threshold energy for this process is $h\nu_{thresh.} = 2.044\ MeV$. Since the threshold energy of this interaction is greater than the maximum energy used in this work, we will not study this process more thoroughly.

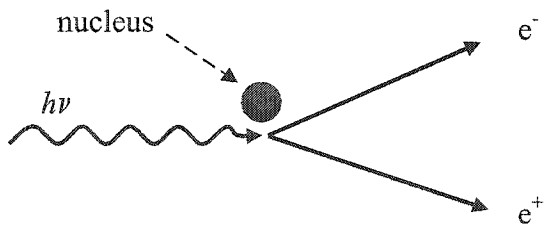

Figure 2-3. Schematic representation of the pair production process. An incident photon of energy $h\nu$ interacts with the Coulomb field of a nucleus. The photon is absorbed and an electron-positron pair (e-,e+) is created.

3. *Post-interaction processes*

We have seen that photoelectric absorption and Compton scattering will produce a vacancy in an atom's electronic shells. The produced vacancy is filled by higher-shell

electrons (shells with lower binding energy). The energy difference between the two shells is expanded either through the emission of a photon (characteristic radiation) or is transferred to an electron which is ejected from the atom (Auger effect). Vacancies are also produced by triplet production, Coulomb interaction (charged particle interaction), electron capture by the nucleus (K-capture) and internal conversion (nucleus).

3.1. Characteristic radiation

Characteristic radiation, or fluorescent radiation, is the emission of a photon through the transition of an outer shell electron to a vacancy in an inner shell. The emitted photon's energy is given by the difference of binding energies of the final and initial transition shells, i.e. $h\nu = |E_f| - |E_i|$. A K-shell vacancy filled by an electron from the L-shell will result in the emission of a photon of energy $h\nu = |E_K| - |E_L|$. The filling of the initial vacancy (K-shell in our example) produces a vacancy in an outer shell (L-shell). This latter vacancy can be filled in the same way, again producing an outer shell vacancy. Gradually, the vacancy *moves* to outer shells until it can be filled by a thermal or free electron. The process is shown in Figure 2-4.

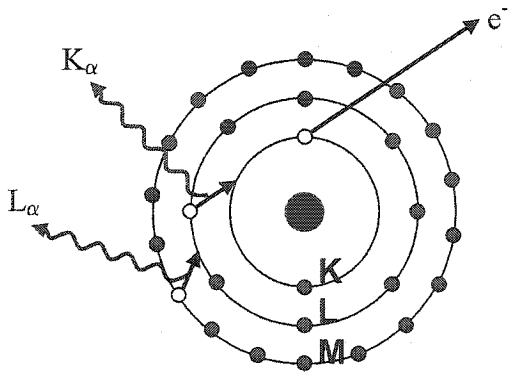

Figure 2-4. Schematic representation of the emission of characteristic radiation. A vacancy in the K-shell is filled by an L-shell electron. A characteristic photon Kα of energy $h\nu = |E_K| - |E_L|$ is emitted following the electron transition. Subsequently, a Lα photon is emitted with energy $h\nu = |E_L| - |E_M|$.

3.2. Auger electrons

The Auger effect is a competing process to the emission of characteristic radiation. The inner shell vacancy is still filled by an atomic electron from a higher shell. The excess energy emerging from the electronic transition is transferred to a third atomic electron. This electron, called the Auger electron, escapes carrying the excess energy in a radiationless process. This leaves the atom doubly ionized. This process of an excited ion decaying into a doubly charged ion by ejection of an electron is called the Auger effect.

The Auger electron will carry a kinetic energy of $T_{e^-} = |E_1| - |E_2| - |E_3|$ where E_1, E_2, E_3 are the binding energies of the vacancy shell, the electron donor shell and the Auger electron shell. For example, a K-shell vacancy filled by an L-shell electron followed by the emission of an M-shell Auger electron (see Figure 2-5) would result in an Auger electron of kinetic energy $T_{e^-} = |E_K| - |E_L| - |E_M|$.

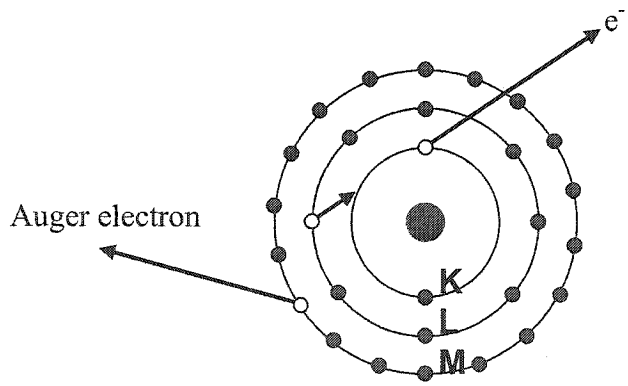

Figure 2-5. Schematic representation of the emission of an Auger electron. A vacancy in the K-shell is filled by an L-shell electron. An Auger electron is emitted from the M-shell (KLM electron) with kinetic energy $T_{e^-} = |E_K| - |E_L| - |E_M|$.

3.3. Fluorescence yield

The relative probability of the emission of characteristic radiation to the emission of an Auger electron is called the *fluorescence yield*, ω. The fluorescence yield is shell

specific and represents, for a given shell, the number of characteristic photons per vacancy in that shell, e.g. $\omega_K = \frac{\text{number of K characteristic photons}}{\text{number of K-shell vacancies}}$ where ω_K is the fluorescence yield of the K-shell. If ω=1, only characteristic radiation is emitted while ω=0 implies the production of Auger electrons only. As seen in Figure 2-6, the K-shell fluorescence yield is negligible when Z<10 but increases rapidly with increasing Z up to almost unity at Z=90. The fluorescence yield of the L-shell is negligible when Z<30 and slowly reaches 0.42 at Z=90.

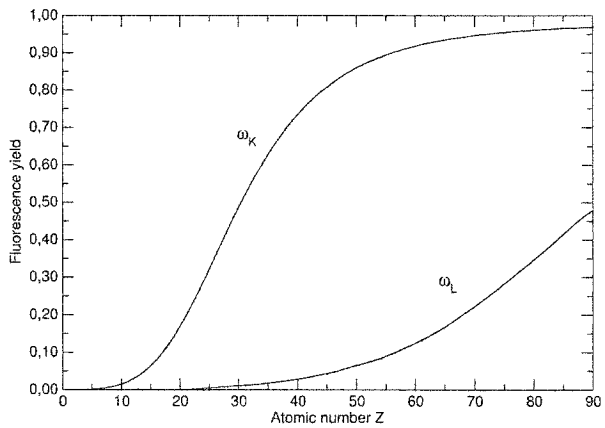

Figure 2-6. Fluorescence yield for K and L shells. Fluorescence yield data from Krause[1].

4. *Interaction cross-sections*

Each of the various processes introduced in Section 2 has a probability of occurring which depends on the photon energy and the atomic number Z of the medium. This probability is expressed in terms of an interaction cross-section σ.

4.1. Cross-section basics

The interaction cross-section concept is different from the geometrical cross-section concept. The geometrical cross-section represents the area of a target presented to incoming radiation e.g. πr^2 for a radius r spherical target. The interaction cross-section

concept symbolizes an *effective* area presented to the incident radiation. It represents an imaginary disc perpendicular to the incident radiation, the higher the interaction probability, the greater the area of the disc. An interaction occurs only when an incident particle hits the disk. For practical reasons, the most widely used cross-section unit is the barn *b* (1 b=10^{-24} cm^2) although its SI unit is the m^2. The total interaction cross-section is the sum of all the individual processes' cross-section.

4.1.1. Atomic and electronic cross-sections

Not all interactions involve the whole atom, some processes such as Compton scattering target electrons. These processes can be described in terms of an electronic cross-section ${}_e\sigma$ (cm^2/electron). The atomic cross-section ${}_a\sigma$ (cm^2/atom) for a medium of atomic number Z is given by multiplying the electronic cross-section by the number of electrons of the atom, ${}_a\sigma = {}_e\sigma \cdot Z$.

4.1.2. Linear attenuation coefficient

When a photon beam travels in a medium, the photons interact through the various processes presented earlier in this chapter. The scattering and absorption of incident photons attenuates the beam. It is useful to know how much the beam is attenuated in function to the thickness of media traveled. This is described by the linear attenuation coefficient μ. This coefficient can be expressed in function of the atomic or electronic cross-sections of the medium, ${}_a\mu = N_a\sigma = NZ_e\sigma$ where N is the number of atoms per cm^3 given by $N = \rho(N_A / A)$; N_A is Avogadro's number (6.023×10^{23} atom/mole), A the atomic mass in g/mole and ρ the medium's density in g/cm^3. The attenuation of a beam can be calculated using

$$\Phi = \Phi_0 e^{-\mu x} \tag{2.4}$$

where $\Phi(x)$ is the photon fluence at depth x in the medium and Φ_o, the initial photon fluence (photon/cm^2). The major drawback of the linear attenuation coefficient is its density dependence. A photon beam will suffer the same attenuation after traveling distance x in a medium of density ρ as traveling distance 2x in a medium of density $\rho/2$.

4.1.3. Mass attenuation coefficient

The attenuation of a photon beam can also be described in term of mass thickness of medium traversed. By replacing the linear attenuation coefficient in Eq. 2.4 by a mass attenuation coefficient (μ/ρ), we get

$$\Phi = \Phi_0 e^{-\left(\frac{\mu}{\rho}\right)x} \tag{2.5}$$

where X= ρx, the mass thickness of the medium in g/cm^2. The use of the mass attenuation coefficient is beneficial since it eliminates the density dependence of the linear attenuation coefficient. The mass attenuation coefficient is expressed in cm^2/g.

4.2. Photoelectric cross-section

Photoelectric cross-sections are difficult to theoretically predict because the solution of the Dirac equation for the ejected electron is complex. The problem is simplified when applied to limiting cases such as small Z or high photon energy. Using a small Z limiting case, Sauter[2] (1931) was able to predict the energy dependence of the K-shell photoelectric cross-section while Hall[3] (1936) predicted the Z dependence in the high energy limit. Since then, numerous photoelectric cross-section tables have been published[4-7]. The latest photoelectric cross-section tabulations are included in the NIST XCOM database[6, 8]. The photoelectric cross sections were obtained by Scofield[9] using his

solution of the Dirac equation for the orbital electrons moving in a static Hartree-Slater central potential. Scofield's results extend only up to 1.5 MeV. At higher energies a semi-empirical formula from Hubbell[7] connects Scofield's values at 1.5 MeV to the high-energy limit values calculated by Pratt[10].

Figure 2-7 shows the photoelectric cross-section τ of lead plotted against photon energy. The saw tooth discontinuities, or absorption edges, occur when the energy of the photon is equal to the binding energies of the electronic shells. When the energy of a photon is below the binding energy of a given shell, no interaction is possible within that shell. Increasing the photon energy equal or higher than the shell binding energy makes the process possibly resulting in instantaneous increase of the cross-section which gives rise to the saw tooth structure in plots of cross-sections as a function of energy.

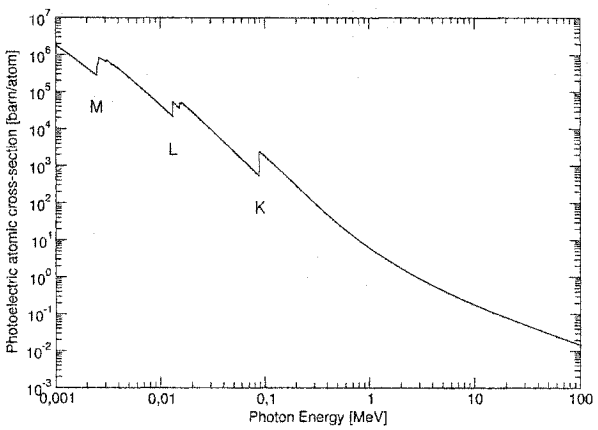

Figure 2-7. Photoelectric cross-section of lead. K, L, M absorption edges are shown. Data from the NIST XCOM photon cross-section database[6].

The photoelectric cross-sections vary roughly as a function of Z^4 and $h\nu^{-3}$, $\tau \propto Z^4/(h\nu)^3$, when the photon energy is low (less than 0.1 *MeV* for lead). When the photon energy is high (5 *MeV* for lead), τ is proportional to $h\nu^{-1}$.

4.3. Thomson scattering cross-section

The classical description of photon-electron scattering (Thomson scattering) is a good approximation at low energies of the correct Compton scattering process. The classical derivation of photon-electron elastic scattering by J.J. Thomson[11] resulted in a formula of the differential cross-section per unit solid angle per electron:

$$\frac{d_e\sigma}{d\Omega} = \frac{r_0^2}{2}(1+\cos\theta^2) \tag{2.6}$$

where

$$r_0 = \frac{e^2}{4\pi\varepsilon_0 c^2} = 2.818\times10^{-13}\,cm \tag{2.7}$$

is the classical radius of the electron. Eq. (2.6) correctly gives the amount of photon scatter for photons of energy zero. Integrating Eq. (2.6) over solid angle gives the total cross-section per electron:

$$_e\sigma = \frac{8\pi r_0^2}{3} = 6.65\times10^{-25}\,cm^2/electron \tag{2.8}$$

The Thomson scattering differential cross-section and total cross-section is the basis for Rayleigh and Compton scattering cross-sections.

4.4. Rayleigh scattering cross-section

The Rayleigh scattering differential cross-section per unit solid angle can be calculated by applying a modifier to Eq. (2.6). The modifier is called the atomic form factor $F(x,Z)$ which is dependent on the atomic number Z and the parameter $x = (\sin\theta/2)/\lambda$, θ is the photon scattering angle and λ the incident photon wavelength.

Atomic form factor values have been tabulated by Plechaty *et al.*[5] and Hubbell[12, 13]. From Eq. (2.6) and the atomic form factor we get:

$$\frac{d\sigma_{coh}}{d\Omega} = \frac{r_0^2}{2}(1+\cos^2\theta)[F(x,Z)]^2 \tag{2.9}$$

For small θ, $F(x,Z)$ approaches Z while at greater angles it tends to zero. This results in a forward peaked photon scatter.

4.5. Compton scattering cross-section

Thomson's classical scattering theory does not correctly represent the scatter process when relativistic effects become noticeable. Klein and Nishina[14] applied Dirac's relativistic theory of the electron to photon-electron scattering. The Klein-Nishina (KN) theory still considers the electron to be free and stationary, which explains some difficulties of the Klein-Nishina theory in very low photon energies. Klein and Nishina showed that the differential cross-section per unit solid angle per electron is given by:

$$\frac{d_e\sigma}{d\Omega} = \frac{r_0^2}{2}(1+\cos^2\theta)F_{KN} \tag{2.10}$$

where

$$F_{KN} = \left[\frac{1}{1+\varepsilon(1-\cos\theta)}\right]^2\left[\frac{\varepsilon^2(1-\cos\theta)^2}{[1+\varepsilon(1-\cos\theta)](1+\cos^2\theta)}\right] \tag{2.11}$$

The parameter $\varepsilon = h\nu / m_0c^2$ and θ is the photon scattering angle. When the photon energy is small ($\varepsilon \ll 1$) or when θ=0 and the electron does not receive energy, F_{KN}=1 which reduces Eq. (2.10) to the classical Thomson equation (Eq. (2.6)) as it should in those limiting cases. By integrating Eq. (2.10) over all scattering angles θ, the Compton cross-section per electron (in cm^2/electron) is obtained:

$$ {}_e\sigma = 2\pi r_0^2 \left[\frac{1+\varepsilon}{\varepsilon^2}\left(\frac{2(1+\varepsilon)}{1+2\varepsilon} - \frac{\ln(1+2\varepsilon)}{2\varepsilon} \right) + \frac{\ln(1+2\varepsilon)}{2\varepsilon} - \frac{1+\varepsilon}{(1+2\varepsilon)^2} \right] \tag{2.12} $$

Compton interactions are not adequately described by the Klein-Nishina theory when the energy of the incident photon is comparable to the target electron's binding energy since KN theory presumes an unbound electron. To palliate this shortcoming, the KN equation is weighted by an incoherent scattering function S(x,Z). Extensive tables of the incoherent scattering function can be found in Hubbell *et al.* (1975)[12]. Bound Compton scattering is then described by

$$ \frac{d\,{}_e\sigma_{inc}}{d\theta} = \frac{d\,{}_e\sigma_{KN}}{d\theta} S(x,Z) \tag{2.13} $$

where ${}_e\sigma_{inc}$ is the bound Compton scattering cross-section and ${}_e\sigma_{KN}$ is the Klein-Nishina cross-section. Figure 2-8 shows the bound and KN cross-section curves for carbon (Z=6) and clearly demonstrates the effect of binding at low energies.

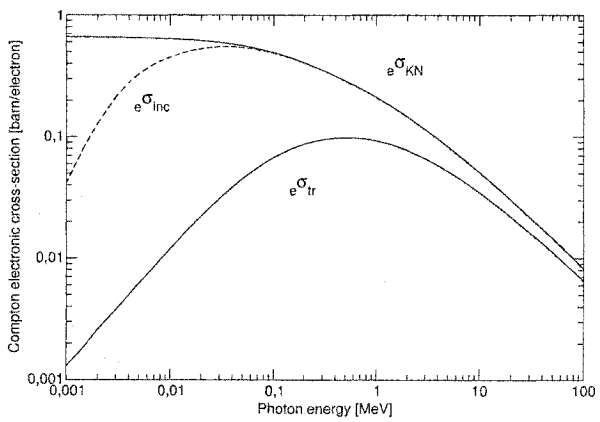

Figure 2-8. Klein-Nishina and bound Compton electronic cross-sections of carbon. Bound Compton data from the XCOM photon cross-section database[6]. Klein-Nishina cross-sections derived from Eq. (2.12). The electronic energy transfer coefficient ${}_e\sigma_{tr}$ is shown (see section 4.8.2).

Figure 2-8 shows as well that Compton electronic cross-sections are inversely proportional to the photon energy when $h\nu$ is large. Compton electronic cross-sections are

Z independent when binding effects are negligible since the Klein-Nishina theory is then applicable.

4.6. Pair production cross-section

The atomic pair production cross-section ${}_a\kappa$ is described by the Bethe-Heitler theory and is given by

$$ {}_a\kappa = \alpha r_0^2 Z^2 \bar{P} \tag{2.14}$$

where $\alpha = \frac{e^2}{4\pi\varepsilon_0 \hbar c} \simeq \frac{1}{137}$ is the fine structure constant and $\bar{P}$ is a function of $h\nu$. Consequently, we see that ${}_a\kappa$ is proportional to Z^2 and increases with $h\nu$ since $\bar{P}$ varies logarithmically with $h\nu$ and levels off at very high energies. Figure 2-9 shows the atomic pair production cross-section of lead as a function of energy.

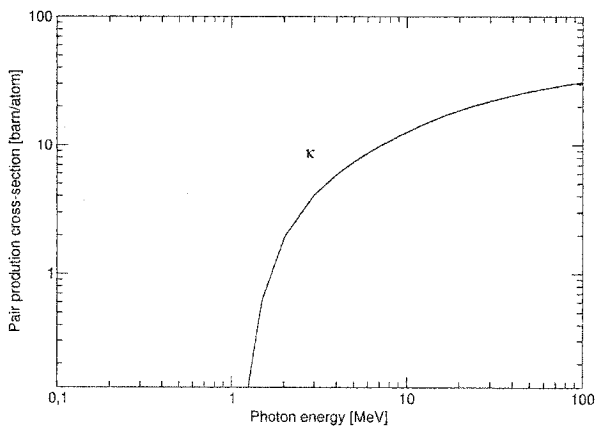

Figure 2-9. Pair production cross-section for lead. Data from the NIST XCOM photon cross-section database[6].

4.7. Total mass attenuation coefficient

Each photon interaction process presented in this chapter contributes to the attenuation of the photon beam. The total mass attenuation coefficient μ/ρ is the sum of the individual processes' coefficient. In the energy range (few keV to ^{60}Co) of interest to

this study, the contributing interactions are photoelectric absorption (τ/ρ), Compton effect (σ/ρ), pair production (κ/ρ) and Rayleigh scattering (σ_{coh}/ρ).

$$\frac{\mu}{\rho} = \frac{\tau}{\rho} + \frac{\sigma}{\rho} + \frac{\sigma_{coh}}{\rho} + \frac{\kappa}{\rho} \tag{2.15}$$

Figure 2-10 shows the mass attenuation curves of the individual interactions and the total mass attenuation coefficient.

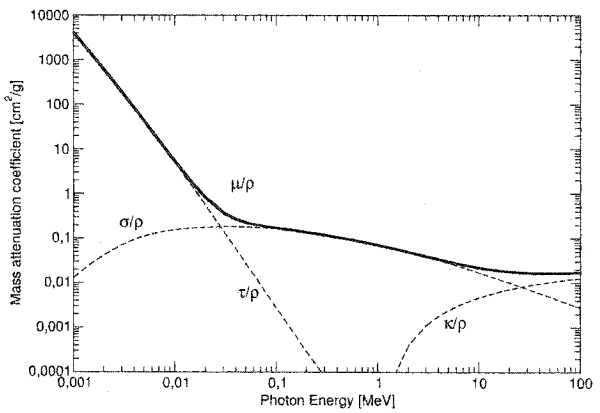

Figure 2-10. Total and partial mass attenuation coefficients of water. Data from the NIST XCOM photon cross-section database[6].

4.8. Mass energy-transfer coefficient

The mass energy-transfer coefficient μ_{tr}/ρ is the fraction of energy transferred from the photon to secondary electrons in the medium. The mass energy-transfer coefficient is calculated from the mass attenuation through $\bar{E}_{tr}$, the mean energy transferred to the electron.

$$\frac{\mu_{tr}}{\rho} = \frac{\mu}{\rho}\frac{\bar{E}_{tr}}{h\nu} \tag{2.16}$$

As per the mass attenuation coefficient, the total mass energy-transfer coefficient is the sum of the coefficients of the energy transferring interactions (photoeffect, Compton, pair production).

$$\frac{\mu_{tr}}{\rho} = \frac{\tau_{tr}}{\rho} + \frac{\sigma_{tr}}{\rho} + \frac{\kappa_{tr}}{\rho} \tag{2.17}$$

4.8.1. Photoelectric absorption mass energy-transfer coefficient

The mean energy transferred to electrons for photoeffect has to take into account the fluorescence yield and the probability of the interaction occurring in a given shell. Considering this, the photoeffect mean mass energy-transfer coefficient is given by

$$\frac{\tau_{tr}}{\rho} = \frac{\tau}{\rho}\left(\frac{h\nu - \sum p_i \omega_i h\overline{\nu}_i}{h\nu}\right) \tag{2.18}$$

where p_i is the probability of an interaction occurring with shell i, ω_i is the fluorescence yield of the ith shell and $h\overline{\nu}_i$ is the mean characteristic photon energy for interactions with the ith shell.

4.8.2. Compton scattering mass energy-transfer coefficient

The fraction of incident photon energy transferred to the recoil electron is $(h\nu - h\nu')/h\nu$. By integrating the product of Eq. (2.10) and $(h\nu - h\nu')/h\nu$ over all scattering angles, we get the energy transfer cross-section ${}_e\sigma_{tr}$. Using ${}_e\sigma_{tr}$ and ${}_e\sigma$ we can calculate the mean energy of the recoil electron:

$$\overline{T}_{e^-} = h\nu \frac{{}_e\sigma_{tr}}{{}_e\sigma} \tag{2.19}$$

The maximum energy transferred is given by setting $\theta = \pi$ in Eq. (2.1) giving

$$T_{e^-,\max} = h\nu \frac{2\varepsilon}{1+2\varepsilon} \tag{2.20}$$

Figure 2-11 shows the maximum $T_{e^-,\max}/h\nu$ and mean $\overline{T}_{e^-}/h\nu$ fraction of energy transferred to the recoil electron. The mean Compton mass energy-transfer coefficient is given by

$$\frac{\sigma_{tr}}{\rho} = \frac{\overline{T}_{e^-}}{h\nu}\frac{\sigma}{\rho} \tag{2.21}$$

where $\overline{T}_{e^-}$ is read off Figure 2-11. Figure 2-11 is known to McGill medical physics students as *The Graph*.

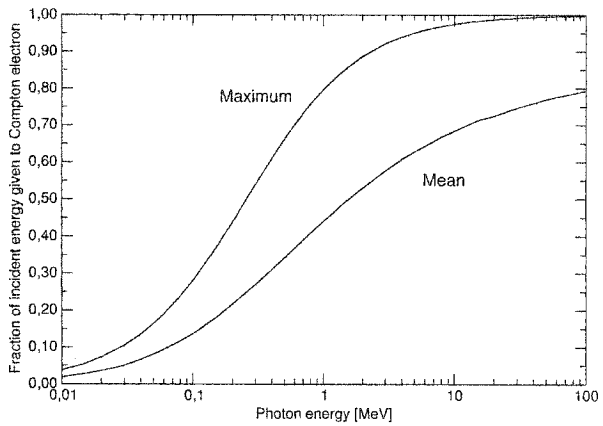

Figure 2-11. *The Graph*. Maximum ($T_{e^-,\max}/h\nu$) and mean ($\overline{T}_{e^-}/h\nu$) fraction of energy transferred to the Compton recoil electron as calculated by Eq. (2.19) and Eq. (2.20).

4.8.3. Pair production mass energy-transfer coefficient

The energy transferred by a photon to the electron-positron pair is always $h\nu - 2m_0c^2$. The mean mass energy-transfer coefficient for pair production is then given by

$$\frac{\kappa_{tr}}{\rho} = \frac{\kappa}{\rho}\left(\frac{h\nu - 2m_0c^2}{h\nu}\right) \tag{2.22}$$

4.9. Mass energy-absorption coefficient

The mass energy-absorption coefficient μ_{en}/ρ represents the fraction of incident photon energy absorbed in the medium. In general, $\mu_{en} \prec \mu_{tr}$ since electrons can radiate energy through the bremsstrahlung radiative process (see Chapter 3). This indicates that the energy transferred to the electron from the incident photon is not entirely deposited in the medium by the electron. The mass energy-absorption and energy-transfer coefficient are related by $\bar{g}$, the fraction of the initial photon energy expended in radiative interactions by the slowing down electrons.

$$\frac{\mu_{en}}{\rho} = \frac{\mu_{tr}}{\rho}(1-\bar{g}) \tag{2.23}$$

The $\bar{g}$ parameter tends to zero when Z and/or $h\nu$ are low and increases with Z and $h\nu$ since bremsstrahlung is dependent on Z and $h\nu$ (see Chapter 3).

5. Summary

We have introduced the dominant photon interactions of the 1 keV to ^{60}Co (1.25 MeV) energy range. The primary interactions in this energy range are photoelectric absorption, Compton effect and pair production. Photoelectric effect and pair production result in the photon being absorbed by the atom while it is scattered in Compton effect. Compton and photoeffect leave the target with a vacancy in one of its electronic shells. This vacancy leads to the emission of characteristic radiation (X-ray) or Auger electrons.

Each process has a probability of occurring described by its interaction cross-section. Attenuation, energy-transfer and energy-absorption coefficients are all directly derived from the interaction cross-section.

6. References

[1] Krause, M.O., *Atomic Radiative and Radiationless Yields for K and L Shells.* J. Phys. Chem. Ref. Data, 1979. **8**: p. 307.

[2] Sauter, F., Ann. Physik, 1931. **11**: p. 454.

[3] Hall, H., Revs. Modern Phys., 1936. **8**: p. 358.

[4] Storm, E. and H.I. Israel, *Photon cross sections from 1 keV to 100 MeV for elements Z=1 to Z=100.* Atomic Data and Nuclear Data Tables, 1970. **7**: p. 565-681.

[5] Plechaty, E.F., D.E. Cullen, and R.J. Howerton, *Tables and Graphs of Photon-Interaction Cross Sections from 0.1 keV to 100 MeV Derived from the LLNL Evaluated-Nuclear-Data Library.* 1978, Lawrence Livermore National Laboratory.

[6] Berger, M.J., et al., *XCOM: Photon cross section database.* 1999.

[7] Hubbell, J.H., *Photon Cross Sections, Attenuation Coefficients, and Energy Absorption Coefficients from 10 keV to 100 GeV.* 1969, National Bureau of Standards.

[8] Berger, M.J. and J.H. Hubbell, *XCOM: photon cross-sections on a personal computer.* 1987, National Bureau of Standards.

[9] Scofield, J.H., *Theoretical Photoionization Cross Sections from 1 to 1500 keV.* 1973, Lawrence Livermore National Laboratory.

[10] Pratt, R.H., *Atomic Photoelectric Effect at High Energies.* Phys. Rev., 1960. **117**: p. 1017-1028.

[11] Thomson, J.J., *Conduction of Electricity Through Gases.* 1906, London: Cambridge Univ. Press. p. 325.

[12] Hubbell, J.H., et al., *Atomic Form Factors, Incoherent Scattering Functions, and Photon Scattering Cross Sections.* J. Phys. Chem. Ref. Data, 1975. **4**: p. 471-539.

[13] Hubbell, J.H. and I. Øverbø, *Relativistic Atomic Form Factors and Photon Coherent Scattering Cross Sections.* J. Phys. Chem. Ref. Data, 1979. **8**: p. 69-105.

[14] Klein, O. and Y. Nishina, *Über die Streuung von Strahlung durch freie Elektronen nach der neuen relativistischen Quantendynamik von Dirac.* Physik, 1929. **52**: p. 853-868.

Chapter 3

Electron interactions with matter

1. Introduction

As seen in Chapter 2, photons can only ionize matter by transferring energy to secondary particles which in turn directly ionize atoms of the medium. The photon interactions described previously all result in the production of electrons or positrons as secondary particles. Electrons and positrons transfer their energy directly to the medium and as such are known as directly ionizing radiation. As the last step in the energy deposition process, electrons and positrons play an important role in dosimetry because the energy they transfer to the medium determines the dose given to the medium.

This chapter describes the various processes by which electrons and positrons interact with matter and introduces the concept of stopping power.

2. Types of electron interactions

As electrons travel in a medium, they transfer energy to that medium and are said to be *slowing down*. By the time a given electron has been stopped (or completely transferred its energy), it will have initiated thousands of interactions while a photon traveling the same distance would have interacted only once or twice. Electrons interact with orbital electrons and nuclei of a medium through the Coulomb force. Electron interactions are often classified by comparing the magnitude of the classical impact parameter b to the magnitude of the classical atomic radius a as illustrated in Figure 3-1. Interactions can be categorized into three types of interactions: (1) soft collisions when

$b \gg a$, (2) hard collisions when $b \approx a$ and (3) nuclei interactions when $b \ll a$. A fourth process is possible for positrons, annihilation. The positron annihilates at rest or in-flight with an electron and produces two photons of energy equal to (at rest) or greater than (in-flight) 0.511 MeV. This last interaction will not be discussed at greater length.

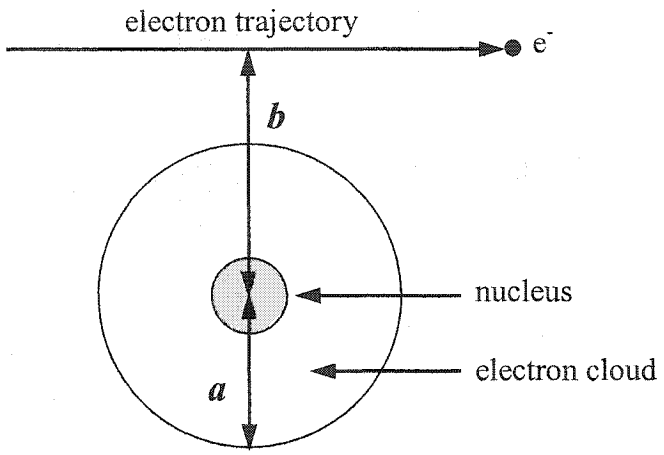

Figure 3-1. Representation of an electron-atom interaction and its collision parameters. Shown are the classical atomic radius a and the impact parameter b.

2.1. Soft collisions (b >> a)

When the impact parameter b is much larger than the atom radius a, the incident electron interacts with the whole atom through the Coulomb force. It can not interact directly with one orbital electron since the distance separating them is too large. Only a small part of the incident electron's energy will be transferred to the atom (typically, a few eV). This energy transfer either sends the atom into an excited state or results in the ejection of a valence electron. The emitted electron can not ionize or excite an atom because of its low kinetic energy. The above described process is known as a soft collision. Even though an electron only loses a small amount of energy per soft collision, this process accounts for about 50% of the electron's energy loss along its track. This is

possible because soft collisions are the most probable electron interactions with a medium.

2.2. Hard collisions (b ≈a)

When the impact parameter b is of the same order of magnitude of the atomic radius a, the incident electron will interact with an atomic orbital electron. The incident electron transfers a large part of its energy to the orbital electron which is ejected from the atom. The ejected atom (called δ-ray) has a large kinetic energy which enables it to travel on its own track and produce atom ionizations or excitations. If the ejected atom originates from an inner shell, characteristic radiation or Auger electrons will be emitted as presented in Chapter 2. Because of the small atomic radius a, hard collisions are rare events when compared to soft collision interactions. This low probability is offset by the large energy transfers made possible by hard collisions. The result is that an electron will lose comparable amounts of energy along its track by both hard and soft collision interactions.

2.3. Radiative collisions (b << a)

When the impact parameter is much smaller than the atomic classical radius, the electron has a high probability of interacting with Coulomb field of the nucleus. In 98% of the cases, the electron is scattered elastically off the nucleus resulting in a change of direction of the incident electron with no occurrence of excitation or ionization of the atom.

In some cases, the electron will undergo a change in direction and acceleration due to the strong nuclear Coulomb field. Classical electromagnetism predicts that an accelerated particle radiates energy according to the Larmor relationship:

$$\frac{dE}{dt} = \frac{e^2 a^2}{6\pi\varepsilon_0 c^3} \tag{3.1}$$

where *dE/dt* is the rate of energy loss and a is the acceleration of the charged particle. The acceleration is proportional to zZ/M where M and z are respectively the mass and charge of the incident particle and Z is the atomic number of the nucleus. According to Eq. (3.1), the rate of energy loss shows a dependency on the mass and charge of the particle and on the nuclear atomic number:

$$\frac{dE}{dt} \propto \left(\frac{zZ}{M}\right)^2 \tag{3.2}$$

It carries that the rate of energy loss will be greater for light incident charged particles $(1/M)$ interacting with high Z atoms. Figure 3-2, illustrates the atomic number dependency of the radiative process as lead's radiative stopping power is an order of magnitude greater than water's. The radiation emitted by the charged particle is known as bremsstrahlung radiation (german for *braking radiation*).

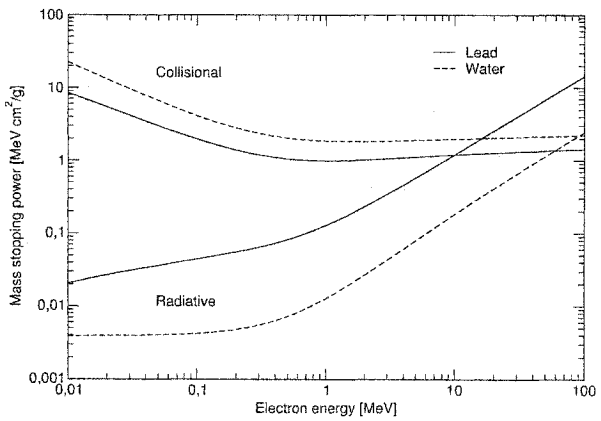

Figure 3-2. Plot of collision and radiative mass stopping power of electrons in lead and water. Data taken from the NIST ESTAR electron stopping power database[1].

3. Stopping power

Stopping power S expresses the average rate of energy loss of a charged particle per unit thickness of material.

$$S = \frac{dT}{dx} \quad [MeV / cm] \tag{3.3}$$

Stopping power being density dependent, it is common practice to use the mass stopping power of a medium S/ρ (in MeV·cm^2/g) to lose this dependency. Since electrons interact with the atom through collisional or radiative processes (see Section 2), it is convenient to split stopping power into a collisional and a radiative component:

$$\frac{S}{\rho} = \frac{S_{coll}}{\rho} + \frac{S_{rad}}{\rho} \; . \tag{3.4}$$

Figure 3-2 presents the collision and radiative mass stopping power components for electrons moving in lead and water. At low energies, collision stopping power is dominant but its value decreases with electron energy to a minimum and starts a slow increase. Radiative stopping power is negligible at low energies but increases rapidly once the electron behaves relativistically (a few hundred keV).

3.1. Mass Collision stopping power

Mass collision stopping power can be written as

$$\left(\frac{S}{\rho}\right)_{coll} = \frac{N_A Z}{A} \int_{W_{min}}^{W_{max}} W \frac{d\sigma}{dW} dW \tag{3.5}$$

where N_A is Avogadro's number, A and Z are the mass and atomic numbers of the medium and $\frac{d\sigma}{dW}$ is the differential electronic cross-section for inelastic scattering in the medium. The value of energy transferred W is found between W_{min}, the minimal energy

necessary to produce ionization or excitation, and W_{max}, the maximal energy transferred. For electron-electron collisions, W_{max} is equal to half the kinetic energy of the incident electron because both particles are indistinguishable. By convention, the faster electron emerging from the collision is said to be the incident electron. When the incident particle is a positron, W_{max} is equal to the total kinetic energy of the positron since both particles can be differentiated. The differential cross-sections describing δ-ray production (or hard collisions) are the Møller[2] cross-sections for electrons and Bhabha[3] cross-sections for positrons. The evaluation of Eq. (3.5) takes into account the differences between soft and hard collision by introducing an energy W_c which separates the two processes. Therefore,

$$\left(\frac{S}{\rho}\right)_{coll} = \frac{N_A Z}{A}\left[\int_{W_{\min}}^{W_c} W\frac{d\sigma}{dW}dW + \int_{W_c}^{W_{\max}} W\frac{d\sigma}{dW}dW\right] \tag{3.6}$$

which gives the Bethe[4, 5] mass stopping power formula:

$$\left(\frac{S}{\rho}\right)_{coll} = \frac{2\pi r_0^2 m_0 c^2}{\beta^2}\left(\frac{N_A Z}{A}\right)\left[\ln\left(T/I\right)^2 + \ln\left(1+\tau/2\right) + F^{\pm}\left(\tau\right) - \delta\right] \tag{3.7}$$

where T is the kinetic energy of the incident particle, $\tau = T/m_0c^2$, r_o is the classical radius of the electron, N_AZ/A is the number of electrons per gram, δ is the *density effect correction* and I is the *mean excitation energy* of the atom. The $F^{\pm}$ term is given by

$$F^{-}\left(\tau\right) = \left(1-\beta^2\right)\left[1+\tau^2/8-\left(2\tau+1\right)\ln 2\right] \tag{3.8}$$

for electrons and by

$$F^{+}\left(\tau\right) = 2\ln 2 - \left(\frac{\beta^2}{12}\right)\left[23 + \frac{14}{\left(\tau+2\right)} + \frac{10}{\left(\tau+2\right)^2} + \frac{4}{\left(\tau+2\right)^3}\right] \tag{3.9}$$

for positrons. The differences in charge and spin between electrons and positrons are taken into account through the $F^{\pm}$ term.

The mean excitation energy I is a parameter derived from experiments which represents the average energy required to provoke an excitation or ionization of the atom. As a rule of thumb, $I = 11.5 \cdot Z\ eV$. Mean excitation energies have been extensively reviewed in the ICRU Report 37[6].

The density effect correction parameter δ takes into account the effect of the polarization of the medium along the charged particles track[7, 8]. This polarization weakens the Coulomb field of atoms near the particle track reducing the stopping power. The density effect is significant only for dense media and increases at high energies. For a review, see ICRU Report 37[6].

3.2. Mass Radiative stopping power

The rate of energy loss due to bremsstrahlung production by electrons or positrons is represented by the mass radiative stopping power (in MeV·cm^2/g) given by the Bethe-Heitler formula[5, 9]:

$$\frac{S_{rad}}{\rho} = \frac{r_0^2}{137}\frac{N_A Z}{A}(T + m_0c^2)\bar{B}_r \tag{3.10}$$

where $\bar{B}_r$ is a function of energy varying from 16/3 to 15 for energies smaller than 0.5 MeV to 100 MeV[10].

3.3. Radiation yield

The radiation yield $Y(T_o)$ of a charged particle of kinetic energy T_o is defined as the fraction of energy lost through radiative processes and is given by:

$$Y(T_o) = \frac{1}{T_o}\int_0^{T_o} \frac{S_{rad}/\rho}{S_{tot}/\rho} dT \tag{3.11}$$

In Chapter 2 Section 4.9, the $\bar{g}$ parameter was introduced to link photon energy-transfer and energy-absorption coefficients. The parameter $\bar{g}$ can be defined as the average value of $Y(T_o)$ for all initial energies of electrons and positrons present in the beam[10].

4. Restricted collision stopping power

We have seen in Section 2.2 that hard collisions can produce δ-rays with enough energy to travel on their own paths away from the original charged particle track. Thus, some energy is carried away and is not deposited locally. If the region of interest is small (like an ionization chamber cavity), the energy deposited outside of the region has to be excluded from the stopping power used for the dose calculation in the cavity as to avoid overestimation of the deposition of energy in the cavity. The restricted collision stopping power L excludes energy transfers to secondary particles over a specified energy threshold Δ and is denoted as L_Δ. For example, a restricted collision stopping power with Δ=10 keV represents the rate of energy loss due to the primary charged particles and all the secondary charged particles produced with kinetic energy less than 10 keV. When Δ is equal to the maximum energy transfer (W_{max}), the restricted collision stopping power is equal to the unrestricted collision stopping power S.

$$\left(\frac{L}{\rho}\right)_{\Delta=W_{max}} = \left(\frac{S}{\rho}\right)_{coll} \tag{3.12}$$

The mass restricted collision stopping power expression for electrons and positrons is obtained by substituting W_{max} by Δ in Eq. (3.6) and is given by[6]:

$$\left(\frac{L}{\rho}\right)_{\Delta} = \frac{2\pi r_o^2 m_o c^2}{\beta^2}\frac{N_A Z}{A}\left[\ln\left(T/I\right)^2 + \ln\left(1+\tau/2\right) + G^{\pm}\left(\tau,\eta\right) - \delta\right]. \qquad (3.13)$$

This expression only differs from the mass unrestricted collision stopping power of Eq. (2.6) by the $G^{\pm}$ terms replacing the $F^{\pm}$ terms:

$$G^{-}\left(\tau,\eta\right) = 1-\beta^2 + \ln\left[4\left(1-\eta\right)\eta\right] + \left(1-\eta\right)^{-1} + \left(1-\beta^2\right)\left[\frac{\eta^2\tau^2}{2} + \left(2\tau+1\right)\ln\left(1-\eta\right)\right], \qquad (3.14)$$

for electrons and by:

$$G^{+}\left(\tau,\eta\right) = \ln 4\eta - \beta^2\left[1 + \left(2-\xi^2\right)\eta - \left(3+\xi^2\right)\left(\xi\tau/2\right)\eta^2 + \left(1+\xi\tau\right)\left(\xi^2\tau^2/3\right)\eta^3 - \left(\xi^3\tau^3/4\right)\eta^4\right] \qquad (3.15)$$

for positrons where $\eta = \Delta/T$, $\xi = (2+\tau)^{-1}$ and $\tau = T/m_0c^2$. Let us point out that $G^{-}\left(\tau,1/2\right) = F^{-}\left(\tau\right)$ and $G^{+}\left(\tau,1\right) = F^{+}\left(\tau\right)$.

5. Summary

Electrons and positrons interact with orbital electrons and nuclei of a medium through the Coulomb force. Interactions can be categorized into three types: soft collisions ($b \gg a$), hard collisions ($b \approx a$) and radiative interactions ($b \ll a$) where b is the classical impact parameter and a is the classical radius of the atom. Soft collisions are the most probable process but individual collisions only amount for small energy transfers to the medium. Hard collisions have a lower probability but individual collisions result in large energy transfers. Hard collisions happen between the incident charged particle and an orbital electron while soft collisions are due to the incident particle interacting with the whole atom. A charged particle will lose comparable amounts of energy through soft and hard collisions. Interactions with nuclei are possible when $b \approx a$. A few of these

interactions (~ 2%) result in the emission of bremsstrahlung photons by the incident charged particle while the majority of particles are elastically scattered by nuclei.

Stopping power is defined as the rate of kinetic energy loss by a charged particle per unit length. Stopping power is divided in collisional and radiative components to reflect the type of interactions possible. Restricted stopping power only represents local energy deposition through the use of a cutoff energy Δ over which the energy is deemed to be transported away.

6. References

[1] Berger, M.J., J.S. Coursey, and M.A. Zucker, *ESTAR, PSTAR, and ASTAR: Computer Programs for Calculating Stopping-Power and Range Tables for Electrons, Protons, and Helium Ions (version 1.21).* 1999, National Institute of Standards and Technology, Gaithersburg, MD.

[2] Møller, C., *Zur Theories des Durchgangs schneller Elektronen durch Materie.* Ann. Phys., 1932. **14**: p. 568.

[3] Bhabba, H.J., *The scattering of positrons by electrons with exchange on Dirac's theory of the positron.* Proc. Roy. Soc. A., 1936. **146**: p. 83.

[4] Bethe, H., *Zur Theorie des Duchgangs schneller Korpuskularstrahlen durch Materie.* Ann. Physik, 1930. **5**: p. 325.

[5] Bethe, H. and W. Heitler, *On the stopping of fast particles and on the creation of positive electrons.* Proc. Roy. Soc. A., 1934. **146**: p. 83-112.

[6] ICRU, *Stopping powers for electrons and positrons*, ICRU Report 37, International Commission on Radiation Units and Measurements, Bethesda, Maryland (1984).

[7] Sternheimer, R.M., *The density effect for the ionization loss in various materials.* Phys. Rev., 1952. **88**: p. 851.

[8] Sternheimer, R.M., S.M. Seltzer, and M.J. Berger, *Density effect for the ionization loss of charged particles.* Phys. Rev., 1982. **B26**: p. 6067.

[9] Evans, R.D., *The atomic nucleus.* 1955: McGraw-Hill.

[10] Attix, F.H., *Introduction to radiological physics and radiation dosimetry.* 1986, New York: Wiley & Son.

Chapter 4

Radiation dosimetry concepts

1. Basic dosimetry quantities

1.1. Fluence

Let N be the expectation value of the number of particles striking an infinitesimal sphere centered at a point P per unit time and da the cross-sectional area of the sphere. The particle fluence ϕ is given by:

$$\varphi = \frac{dN}{da} \tag{4.1}$$

and has units of m^{-2} or cm^{-2}. This definition holds for monoenergetic particle beams. In general, radiation sources exhibit an initial energy distribution. The definition can easily be expanded to non-monoenergetic cases where:

$$\varphi = \int_0^{E_{max}} \frac{d\varphi}{dE}(E)dE \tag{4.2}$$

where $d\varphi/dE$ is the energy differential particle fluence.

Instead of only summing the number of particles, one can sum the energy of the particles crossing da. For monoenergetic beams, energy fluence ψ is given by:

$$\psi = E\frac{dN(h\nu)}{da} = E \cdot \varphi \ , \tag{4.3}$$

and for spectra :

$$\psi = \int_0^{E_{max}} E \cdot \frac{d\varphi}{dE} \cdot dE \ . \tag{4.4}$$

1.2. Kerma

Kerma (Kinetic Energy Released per unit MAss) describes the energy dissipated by indirectly ionizing radiations (photons, neutrons) by determining the energy transferred to charged particles in a specified finite volume V. The energy transferred does not include energy transferred from a charged particle to another. Kerma can be written as:

$$K = \frac{dE_{tr}}{dm} \tag{4.5}$$

where dE_{tr} is the energy transferred and dm represents the mass of volume dV. Kerma is expressed in Gray (Gy) or J/kg.

Kerma is related to the photon fluence by:

$$K = \psi \left(\frac{\mu_{tr}}{\rho} \right) \tag{4.6}$$

where ψ is the photon energy fluence and (μ_{tr}/ρ) is the mass energy-transfer coefficient of the medium. Eq (4.6) is only valid for monoenergetic photons. In case of a poly-energetic beam, we have to integrate over the particle fluence differential in energy of Eq. (4.4):

$$K = \int_0^{E_{max}} E \cdot \frac{d\varphi}{dE} \cdot \left(\frac{\mu_{tr}}{\rho} \right)_E dE \tag{4.7}$$

where the mass energy-transfer coefficient is dependent on the energy E. As mentioned in Chapter 3, once an electron is put in motion it can lose its kinetic energy through Coulomb force interactions or radiative interactions. To differentiate between those two processes, kerma can be divided in a collision and a radiative component:

$$K = K_{coll} + K_{rad} = \left(\frac{\mu_{en}}{\rho} + \bar{g} \frac{\mu_{tr}}{\rho} \right) \varphi E \ . \tag{4.8}$$

1.3. Absorbed dose

The absorbed dose can be defined as the mean stochastic average of energy imparted per unit mass:

$$D = \frac{d\varepsilon}{dm} . \tag{4.9}$$

Dose is also expressed in units of Gy (or J/kg). The difference between kerma and dose is that kerma only dealt with the energy transferred to charged particles in a volume of interest and not necessarily deposited in the volume, i.e. the energy can leave the volume without affecting kerma. Dose on the other hand only takes into account the energy deposited in the medium within the volume of interest through electron interactions.

1.4. Charged particle equilibrium

Charged particle equilibrium (CPE) exists for the volume v if each charged particle of a given type and energy leaving v is replaced by an identical particle of the same energy entering, in terms of expectation values (Attix, 1983)[1].

2. *Cavity theory*

Cavity theory was introduced to solve the problem of measuring absorbed dose to a medium by using a cavity dosimeter inserted in the medium. The dosimeter actually measures the dose to its cavity gas and cavity theory makes it possible to relate that measured dose to dose in the medium at the point of measurement.

Let's assume a monoenergetic beam of charged particle of energy T crossing a boundary separating media m and g (Figure 4-1). Dose to medium m is given by:

$$D_m = \Phi \left(\frac{S_T}{\rho} \right)_{coll,m} \tag{4.10}$$

where Φ is the charged particle fluence and $(S_T/\rho)_{coll,m}$ is the mass collision stopping power of medium m for charged particle of energy T. Assuming that the fluence is constant across the boundary neglecting fluence perturbation caused by, e.g. backscatter, the ratio of doses to each medium is given by:

$$\frac{D_g}{D_m} = \frac{(S_T/\rho)_{coll,g}}{(S_T/\rho)_{coll,m}} = \left(\frac{S_T}{\rho}\right)_m^g \tag{4.11}$$

where $(S_T/\rho)_m^g$ is the ratio of stopping powers of media g and m. In the case of a charged particle spectrum, the stopping power is replaced by an average collision stopping power specified as:

$$\left(\frac{\bar{S}}{\rho}\right)_{coll,m} = \frac{\int_0^{T_{max}} \Phi_T(T)\left(S(T)/\rho\right)_{coll,m} dT}{\int_0^{T_{max}} \Phi_T(T) dT} = \frac{D_m}{\Phi} \tag{4.12}$$

where $\Phi_T(T)$ is the charged particle fluence spectrum differential in energy. The ratio of doses across a boundary is the ratio of collision stopping powers when the fluence is constant in both media. Based on this principle, dose in a cavity can be related to dose in the medium surrounding the cavity.

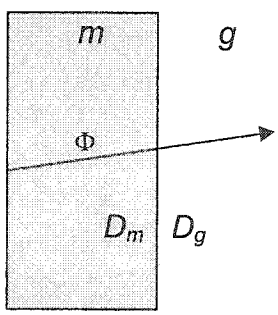

Figure 4-1. Beam of charged particles crossing an interface between media m and g. The particle fluence Φ is assumed constant through the interface. The doses of both sides are related through a stopping power ratio [see Eq. (4.11)].

2.1. Bragg-Gray cavity theory

W. H. Bragg[2] and L. H. Gray[3, 4] applied the concepts of Section 1.5 to relate the dose of a cavity present in a medium to the dose of the medium. Let's suppose an homogeneous medium *m* containing a thin layer of medium *g* as in Figure 4-2.

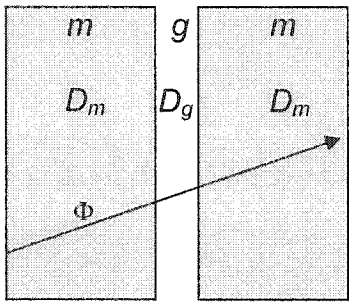

Figure 4-2. Charged particles crossing a cavity of medium *g* embedded in a homogeneous medium *m*.

Two conditions need to be met in order for the Bragg-Gray theory to be applied. These assumptions are:

- The thickness of the *g*-layer is assumed to be so small in comparison with the range of the charged particles crossing it that its presence does not perturb the charge particle field.
- The absorbed dose to the cavity is assumed to be deposited entirely by the charged particles crossing it.

The first condition implies that the charged particle fluence in the cavity is equal to the fluence of medium *m*, $\Phi_g = \Phi_m$. The second condition entails that no electron is produced inside the cavity and so electrons crossing the cavity originate from outside the cavity. It also implies that photons do not interact within the cavity. From the Bragg-Gray conditions, it can be said that from the charged particle's perspective the cavity is not present.

When the Bragg-Gray conditions are met, the charged particle fluence is constant across the cavity and the ratio of dose to the medium to dose to the cavity is given by:

$$\frac{D_m}{D_g} = \frac{\left(\bar{S}_T / \rho\right)_{coll,m}}{\left(\bar{S}_T / \rho\right)_{coll,g}} = \left(\frac{\bar{S}_T}{\rho}\right)_g^m . \tag{4.13}$$

Assuming the cavity medium is a gas, the dose to the gas D_g can be determined by measuring the charge Q produced by the radiation. The relationship between D_g and Q is:

$$D_g = \frac{Q}{m}\left(\frac{\bar{W}}{e}\right)_g \tag{4.14}$$

where m is the mass of gas (in kg) of the cavity in which the charge Q (in coulombs) was produced. $\left(\frac{\bar{W}}{e}\right)_g$ is the mean energy required to produce an ion pair in the gas. As electrons travel in a gas, they lose energy through ionization of the gas' atoms, effectively creating pairs of positive and negative ions. Ionization chambers measure the charge created in the gas and this measure can be converted to D_g by Eq. (4.14). For dry air, the value $\left(\frac{\bar{W}}{e}\right)_{air}$ is 33.97 J/C. The dose to the medium can be calculated by substituting Eq. (4.14) into Eq. (4.13) giving:

$$D_m = \frac{Q}{m}\left(\frac{\bar{W}}{e}\right)_g \left(\frac{\bar{S}}{\rho}\right)_g^m . \tag{4.15}$$

This last example showed a simple case of the usefulness of the Bragg-Gray theory. It is evident that the fulfillment of the Bragg-Gray conditions depends on the size of the cavity and on the energy of the charged particles involved but the theory has no way of taking into account the size of the cavity. The Bragg-Gray theory also does not account

for the presence of secondary electrons in the slowing down of primary electrons. These shortcomings are addressed in the Spencer-Attix[5] cavity theory.

2.2. CSDA electron fluence

Consider a small cavity filled with medium *g* embedded in medium *m* which contains a homogeneous source of electron of energy T_o. The number of electrons per unit mass is *N*. Assuming that no bremsstrahlung radiation is produced and that charged particle equilibrium exists, the dose deposited to medium *m* is given by:

$$D_m = NT_0 \ . \tag{4.16}$$

Using the integral form of Eq. (4.10) and equating it with Eq. (4.16), dose can be expressed as:

$$D_m = \int_0^{T_0} \Phi_T(T)\left(S(T)/\rho\right)_m dT = NT_0 \tag{4.17}$$

where Φ_T is the equilibrium charged particle fluence. To satisfy the Eq. (4.17), the equilibrium spectrum has to be given by:

$$\Phi_T(T) = \frac{N}{S_m(T)/\rho} \ , \tag{4.18}$$

which indicates that the equilibrium spectrum for a source of initially monoenergetic charged particles is proportional to the number of particles released per unit mass and inversely proportional to the mass stopping power of the medium in which the charged particles slow down. Using this electron spectrum, we can derive dose in the cavity as:

$$D_g = \int_0^{T_0} \frac{N}{\left(S_m(T)/\rho\right)}\left(S_g(T)/\rho\right)dT \tag{4.19}$$

The ratio of doses is derived from this last equation since $D_m = NT_0$, giving:

$$\frac{D_g}{D_m} = \frac{1}{T_0}\int_0^{T_0} \frac{S_g(T)/\rho}{S_m(T)/\rho} dT \ . \tag{4.20}$$

This equation holds under the assumptions of charged particle equilibrium and no bremsstrahlung emission.

A more general case would take into account the possible emission of bremsstrahlung photons by the slowing down electrons. The dose is now given by:

$$D_m = NT_0\left(1 - Y_m(T_0)\right) \ , \tag{4.21}$$

where Y_m is the radiation yield of an electron of kinetic energy T_0. The dose to the medium is now expressed in terms of mass collision stopping power:

$$D_m = \int_0^{T_0} \Phi_T(T)\left(S(T)/\rho\right)_{coll,m} dT \tag{4.22}$$

as is dose to the cavity medium:

$$D_g = \int_0^{T_0} \Phi_T(T)\left(S(T)/\rho\right)_{coll,g} dT \ . \tag{4.23}$$

The equilibrium spectrum is unchanged and given by Eq. (4.18). Using the same procedure as before, the ratio of the doses when bremsstrahlung production is taken into account is:

$$\frac{D_g}{D_m} = \frac{1}{T_0\left(1 - Y_m(T_0)\right)}\int_0^{T_0} \frac{(S(T)/\rho)_{coll,g}}{S_m(T)/\rho} dT \ . \tag{4.24}$$

2.3. Electron spectra including secondaries

The inclusion of secondary electrons in the slowing down process can be achieved through a process similar to the one described above. The equilibrium spectrum including

secondary electrons is expressed in a similar form to Eq. (4.18) and was derived by Spencer and Attix[5]:

$$\Phi_T^{\delta} = \frac{NR(T,T_0)}{S_m(T)/\rho} \quad . \tag{4.25}$$

$R(T,T_0)$ is the ratio of the total electron fluence including δ rays to the primary electron fluence. Monte Carlo techniques are used to calculate electron equilibrium spectra by simulating the electron tracks according to the probability distribution functions obtained from the total and differential cross sections. The calculation of electron slowing down spectra from a monoenergetic primary electron beam can be extended to calculate the spectrum of electrons resulting from an initial photon beam. For each primary electron produced by a photon interaction, an electron spectrum is calculated. All the primary electron spectra are scored to obtain the final spectrum.

2.4. Spencer-Attix cavity theory

The Bragg-Gray theory does not take into account secondary electrons in the slowing down process. The Spencer-Attix theory includes the secondary electrons in the slowing down spectrum as discussed in the previous section. Spencer and Attix[5] expanded the Bragg-Gray theory and as such, the Bragg-Gray conditions still have to be met for Spencer-Attix to be applied. More so, the cavity conditions are now more stringent as Spencer-Attix theory assumes that the cavity does not perturb the total electron fluence (including δ rays) instead of only the primary electron fluence as per the Bragg-Gray approach.

Spencer-Attix theory introduces an energy threshold Δ which corresponds to the mean energy of electrons having projected ranges just large enough to cross the cavity. The energy threshold Δ effectively separates the electrons into two groups:

- ***Fast* electrons:** electrons with $T \geq \Delta$, therefore they can transport energy. They have enough energy to cross the cavity and are part of the electron slowing down spectra.
- ***Slow* electrons:** electrons with $T \prec \Delta$. They deposit their energy locally where their energy falls below Δ. The *slow* electrons are assumed not to transport energy nor to enter the cavity.

The dose is calculated using the electron fluence spectrum which includes secondary electrons of energy greater than Δ and less than $T_0/2$, since the maximum energy transfer in an electron-electron interaction is $T_0/2$. All electrons are allowed to slow down and deposit energy but now energy losses are restricted to a minimum threshold Δ which mandates the use of restricted stopping power ($L_\Delta(T)/\rho$). The dose ratio then becomes:

$$\frac{D_m}{D_g} = \frac{\int_\Delta^{T_0} \Phi_T^\delta \left(L_{\Delta,m}(T)/\rho\right) dT + TE_m}{\int_\Delta^{T_0} \Phi_T^\delta \left(L_{\Delta,g}(T)/\rho\right) dT + TE_g} = \left(\frac{\bar{L}_\Delta}{\rho}\right)_g^m \tag{4.26}$$

where TE_m and TE_g are the *track-end* terms that account for the energy deposition at the end of an electron's track. Electrons having an initial energy included between Δ and 2Δ could see their energy drop below the threshold and therefore have to deposit their remaining energy on the spot. Approximations of the track-end terms were developed by Nahum[6]:

$$TE_m = \Phi_T^\delta(\Delta)\frac{S_m(\Delta)}{\rho}\Delta \ , \tag{4.27}$$

$$TE_g = \Phi_T^{\delta}(\Delta)\frac{S_g(\Delta)}{\rho}\Delta \ . \tag{4.28}$$

These equations indicate that the portion of the track where the electron energy is lower than Δ deposits an amount of energy per unit mass equal to the product of Δ, the stopping power and the total electron fluence both evaluated at Δ. The track-end terms contribute 5% to 10 % of the dose to the medium.

2.5. Photon beams and cavity theory

Both cavity theories introduced in the previous sections assume that no production of electrons occurs in the cavity. This assumption can be broken when irradiating the chamber with photon beams especially if the cavity is large or if the photon energy is low. In the extreme case where electron ranges are very small, the dose ratio D_m/D_g purely depends on the ratio of the mass energy-absorption coefficients:

$$\frac{D_m}{D_g} = \left(\frac{\bar{\mu}_{en}}{\rho}\right)_g^m \tag{4.29}$$

Burlin proposed a weighted method in which the ratio of doses is given by:

$$\frac{D_g}{D_m} = d\left(\frac{\bar{L}_{\Delta}}{\rho}\right)_m^g + (1-d)\left(\frac{\bar{\mu}_{en}}{\rho}\right)_m^g \tag{4.30}$$

where d corresponds to the average value of electron fluence reduction in the medium. Parameter d is formulated as:

$$d = \frac{\int_0^L \Phi^e e^{-\beta l} dl}{\int_0^L \Phi^e dl} \tag{4.31}$$

with L the mean cavity size, l the distance of any point to the cavity wall and β the effective attenuation coefficient that represents the reduction in particle fluence in the medium whereas (1-d) shows the increase in fluence in the cavity.

2.6. Fano theorem

Fano's theorem:

> *In an infinite medium of given atomic composition exposed to a uniform field of indirectly ionizing radiation, the field of secondary radiation is also uniform and independent of the density of the medium, as well as of the density variations from point to point.*

It follows from this theorem that the charged particle fluence at any point where CPE exists is independent of density variations within the volume of origin of the particle. For example, under CSDA conditions, the total electron fluence is given by:

$$\Phi = \int_0^{T_0} \frac{NdT}{S(T)/\rho} = N\rho R_{CSDA} \,, \tag{4.32}$$

where N is the number of electrons per unit mass and R_{CSDA} is the electron CSDA range. Since the product $N\rho$ is expressed in units of volume and R_{CSDA} is given in cm, it then implies that Φ, the total electron fluence in the medium, is independent of the medium's density.

3. Calibration and measurements

The accurate determination of the dose delivered to a tumour and the healthy surrounding tissue is supported, at its most basic level, by the calibration of the radiation source used for the treatment. The measurement of dose and the calibration of radiation sources are presented in the following sections.

3.1. Dosimeter

The most commonly used dosimeter for clinical measurements and calibration is the cavity ionization chamber. Figure 4-3 presents a schematic diagram of a parallel-plate ionization chamber system.

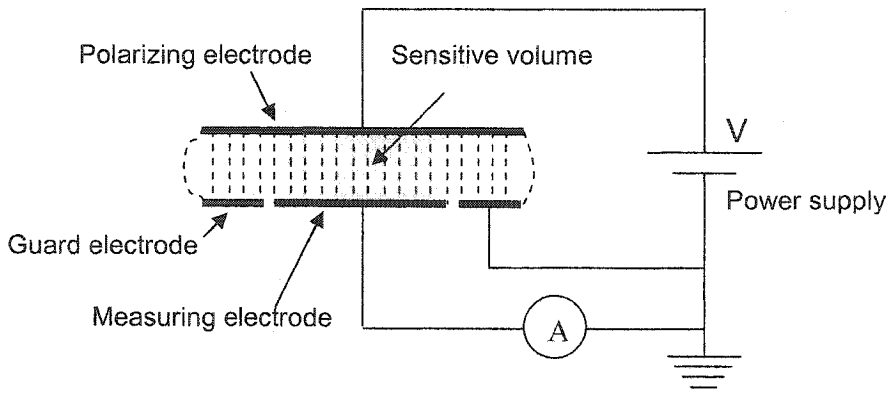

Figure 4-3. Diagram of a parallel-plate cavity ionization chamber and its operating circuit.

The system consists of the ionization chamber itself, a power supply and an electrometer which measures the charge collected in the sensitive volume of the chamber. The chamber has three electrodes with different functions. The polarizing electrode is connected to the power supply and is responsible for the difference of potential across the cavity. The measuring electrode is grounded through a high impedance electrometer and is responsible for collection of radiation created charges in the sensitive volume. The role of the guard electrode is to help define the sensitive volume and to prevent the collection of leakage current. When the chamber is irradiated, ion pairs are created in the cavity gas (typically air) and collected at the measuring electrode. Since the average energy necessary to produce an ion pair in air is well known, $\left(\frac{\bar{W}}{e}\right)_{air}$ = 33.97 J/C, the charge collected can be converted to dose by using the relationship $D_g = \frac{Q}{m}\left(\frac{\bar{W}}{e}\right)_g = \frac{Q}{\rho V}\left(\frac{\bar{W}}{e}\right)_g$,

where ρ is the density of the gas and V the sensitive volume of the cavity chamber. This equation implies the knowledge of the sensitive volume of the cavity chamber. In practice, this volume is not known and must be determined by a standards laboratory.

3.2. Calibration factor

In practice, the standards laboratory does not give the end-user the volume of its chamber but a calibration factor proportional to the sensitive volume of the chamber. In the case of low energy photon beams, the calibration is carried out in terms of air kerma. The calibration factor then relates a corrected meter reading to the value of air kerma at the center of the cavity when the chamber is not there.

$$N_K = \frac{K_{air}}{M^c} \text{ [Gy/C]} \tag{4.33}$$

where N_K is the air kerma calibration factor and M^c the electrometer reading fully corrected for temperature, humidity, recombination, polarity effect and electrometer accuracy.

3.3. Ion chamber response

Ion chamber response R in terms of air kerma is defined as the ratio of the dose to the gas of the cavity to the air kerma measured at the center of the cavity when the chamber is not there:

$$R = \frac{D_{gas}}{K_{air}} \,. \tag{4.34}$$

and is the inverse of the air kerma calibration factor, i.e., $R = N_K^{-1}$. If the photon energy is sufficiently high for cavity theory to be applicable, the response can be linked to the

calibration factor N_K. For a cavity measurement under Bragg-Gray conditions, air kerma is given as

$$K_{air} = \frac{Q}{m_{gas}(1-\bar{g})}\left(\frac{\bar{W}}{e}\right)_{gas}\left(\frac{\bar{\mu}_{en}}{\rho}\right)_{wall}^{air}\left(\frac{\bar{L}}{\rho}\right)_{gas}^{wall} A_{wall}A_{fl}A_{pn}. \qquad (4.35)$$

In this equation A_{wall} is the correction factor for photon scattering and absorption in the chamber wall, A_{fl} the fluence perturbation correction factor and A_{pn} is the point source non-uniformity correction factor.

3.4. Dose to water in a water phantom

The goal of radiation dosimetry, in the context of cancer treatment, is to accurately measure and predict the dose deposition to tissue. Since tissue and water have similar radiological properties, the determination of absorbed dose to water (D_w) is one of the main objectives of radiation dosimetry. Because of the limitations inherent to cavity theory, absorbed dose to water is handled differently depending on the energy of the radiation beam.

3.4.1. High energy photon beams

In high energy photon beams ($h\nu \geq {}^{60}$Co), the Bragg-Gray conditions (section 2.1) are satisfied and cavity theory can be used. Using a cavity ion chamber, D_w is determined from D_{gas}. In practice, D_{gas} is not known so use is made of the dose-to-the-gas-volume calibration factor, N_{gas}. The relationship between these two quantities is given by

$$D_{gas} = M^c N_{gas} \qquad (4.36)$$

where M^c is the fully corrected chamber reading. Using Eq. (4.14), (4.33) and (4.35), one can derive N_{gas} from N_K using cavity theory. The advantage of using N_{gas} is that, through

cavity theory, a chamber calibration factor based on exposure, air kerma or absorbed dose can be recast to N_{gas}.

Now that N_{gas} has been formulated, absorbed dose to water can be determined through Spencer-Attix cavity theory and is given by

$$D_w = M^c N_{gas} \left(\frac{\bar{L}}{\rho} \right)_{air}^{w} P_{wall} P_{repl} P_{cel} \tag{4.37}$$

where P_{wall} is the wall correction factor and accounts for the fact that the wall is not water, P_{repl} corrects for the fluence perturbation due to the presence of the chamber and P_{cel} is a central electrode correction factor since the electrode and the wall materials may be different.

For more details on the absorbed dose calibration of high energy photon beams and its formalism, the reader is referred to the International Atomic Energy Agency's (IAEA) TRS-398[7] report or the American Association of Physicists in Medecine's (AAMP) TG-51[8] protocol. For more details on the air-kerma calibration approach in high energy photon beams, the IAEA TRS-277[9] and AAPM TG-21[10] protocols are recommended reading.

3.4.2. Kilovoltage photon beams

A kilovoltage photon beam is defined as having a kV_p (peak kilovoltage) less than 300 kV. The physics of kilovoltage photon beams differs greatly from the one used in high energy beams. In low energy beams, (1) photoelectric absorption is an important interaction when it is not the dominant interaction while Compton scatter is dominant at high energies, (2) phantom scatter is more important, (3) the range of secondary electrons is extremely short which implies that dose is approximately equal to collision kerma and

(4) radiative processes are almost absent for low Z materials (like water and tissue) which gives that $K \approx K_{coll} \approx D$. But most importantly, the cavity of a high energy beam ion chamber is too large for Bragg-Gray conditions to be met which forbids the use of Spencer-Attix cavity theory at low photon energies.

Even though cavity theory is not appropriate, cavity ionization chambers are still used but they are viewed as *photon-only* or air kerma detectors. Since the secondary electrons have very low energies, they cannot traverse the chamber wall. This means that electrons found in the cavity were produced in the wall by photons.

When measuring D_w in a water phantom using an ion chamber, the first difficulty arises from the fact that the ion chamber air kerma calibration factor N_K (which was measured free-in-air) can not yield air-kerma-in-water $(K_{air})_w$ values since the presence of water modifies the radiation beam. To offset this situation, a correction factor $P_{Q,cham}$ is introduced. This correction factor includes all beam quality (Q) and chamber (cham) dependent corrections. $P_{Q,cham}$ accounts for the change in chamber response due to the change in beam characteristics (due to the greater attenuation and scattering of photons in the phantom) between calibration (N_K) and measurement, and of the change in photon fluence at the point of measurement in the cavity compared to that in water in the absence of the chamber and the chamber stem. Air-kerma measured in water is given by

$$\left(K_{air}\right)_w = M^c N_K P_{Q,cham}. \tag{4.38}$$

Using a mass energy-absorption coefficients ratio, air-kerma-in-water is converted to water-kerma-in-water K_w and since $D_w \approx K_w$, then

$$D_w \approx K_w = M^c N_K P_{Q,cham} \left(\frac{\bar{\mu}_{en}}{\rho}\right)_{air}^{w}. \tag{4.39}$$

The determination of absorbed dose in a medium in low energy beams could benefit from a deeper knowledge of the response of the ion chamber used. Since ion chamber response calculations through cavity theory would be inadequate at these low energies, Monte Carlo simulations can be used to calculate the response. Monte Carlo calculations of ion chamber response could help lower the uncertainty on the $P_{Q,cham}$ correction factor which is estimated to be ~1.5% and the understanding of the different effects included in $P_{Q,cham}$. For more details, please refer to the AAPM TG-61[11] kilovoltage dosimetry protocol.

3.5. Calibration of brachytherapy sources

In brachytherapy, the quantity which specifies source strength in a standards-traceable fashion is related to air kerma rate at some distance in air. The air kerma strength S_K is given by:

$$S_K = \dot{K}l^2 \tag{4.40}$$

where l is the reference distance at which the air kerma rate in free air, $\dot{K}$, is specified. The unit of air kerma strength is μGy $h^{-1}m^2$ and has symbol U. The calibration of a brachytherapy source is simply an in-air air kerma rate ($\dot{K}$) measurement at a large distance in free space on the transverse axis. The calibration does not specify activity.

Sources that encompass a wide energy range pose calibration difficulties. For example, ^{192}Ir does not have a primary standard because of its wide photon spectrum (9 to 900 keV). To palliate this situation, an interpolative free-air secondary standard method[12, 13] has been developed and is the interim de facto standard for measurement of high intensity ^{192}Ir. Verhaegen et al.[13] showed that acceptable calibration (average uncertainty

of 1%) of an ^{192}Ir wire could be attained by weighting N_K over the ^{192}Ir spectrum. They showed that a calibration factor for ^{192}Ir radiation is attainable if the photon fluence spectrum of the source at the position of the ionization chamber and the response of the chamber as a function of photon energy is known. The response function was obtained by calibrating the chamber for different energies across the ^{192}Ir spectrum and by fitting the data. The photon fluence spectrum at the position of the chamber is then weighted by the response function. The weighted response function is then inverted to yield the calibration factor for ^{192}Ir. Although this technique is acceptable, it is evident that the development of a primary standard for ^{192}Ir making use of first principles rather than empirical fit would be an improvement.

For other brachytherapy sources such as ^{125}I (mean energy of 28 keV), free-air ionization chambers are suitable as air kerma standards, but in-phantom measurements require a cavity chamber, and hence, accurate Monte Carlo calculations of ion chamber response are important.

In this thesis, we study the accuracy of Monte Carlo simulation as a method to calculate response for low energy photon beams. Monte Carlo simulations are introduced in the next chapter.

4. References

[1] Attix, F.H., Energy imparted, energy transferred and net energy transferred, Phys Med Biol 28 12 (1983) 1385-90.

[2] Bragg, W.H., Consequences of the corpuscular hypothesis of the gamma and x rays, and the ranges of beta rays, Phil. Mag. 20 (1910) 385.

[3] Gray, L.H., Absorption of penetrating radiation, Proc. Roy. Soc. (London) A122 (1929) 647.

[4] Gray, L.H., Ionization method for the absolute measurement of gamma-ray energy, Proc. Roy. Soc. (London) A156 (1936) 578.

[5] Spencer, L.V., Attix, F.H., A theory of cavity ionization, Radiat. Res. 3 (1955) 239.

[6] Nahum, A.E., ed. *Extension of the Spencer-Attix Cavity Theory to the 3 media situation for Electron beams*. Dosimetry in Radiotherapy, ed. IAEA. Vol. 1. 1988, IAEA: Vienna.

[7] Iaea, Absorbed Dose Determination in External Beam Radiotherapy, An International Code of Practice for Dosimetry Based on Standards of Absorbed Dose to Water, Rep. TRS-398, IAEA, Vienna

[8] Almond, P.R., et al., AAPM's TG-51 protocol for clinical reference dosimetry of high-energy photon and electron beams, Med Phys 26 9 (1999) 1847-70.

[9] Iaea, Absorbed Dose Determination in Photon and Electron Beams; An International Code of Practice, Rep. TRS-277, IAEA, Vienna (1987).

[10] Aapm, T.-. A protocol for the determination of absorbed dose from high-energy photon and electron beams, Med. Phys. 10 (1983) 741-771.

[11] Ma, C.M., et al., AAPM protocol for 40-300 kV x-ray beam dosimetry in radiotherapy and radiobiology, Med Phys 28 6 (2001) 868-93.

[12] Goetsch, S.J., et al., Calibration of 192Ir high-dose-rate afterloading systems, Med. Phys. 18 (1991) 462-467.

[13] Verhaegen, F., et al., Calibration of low activity 192Ir brachytherapy sources in terms of reference air kerma rate with large volume spherical ionization chambers, Phys. Med. Biol. 37 (1992) 2071-2081.

Chapter 5

Monte Carlo calculations

1. *Introduction*

Monte Carlo methods can be generally described as statistical simulation methods, where statistical simulation is to be any method that utilizes sequences of (pseudo-) random numbers to perform the simulation. Random sampling methods have been used for centuries, but only in the past several decades has the Monte Carlo technique gained the status of a full-fledged numerical method capable of addressing the most complex applications. For example, Comte de Buffon[1] in 1777 performed an experiment where a needle was dropped numerous times on a board marked with equidistant parallel lines. Buffon showed that the probability of the needle of length L to intersect a line would converge to $p = 2L/\pi d$, where $d>L$ is the distance separating the lines. A century later, Laplace pointed out that this technique could be used as a crude means of estimating the value of π. An other early application of the Monte-Carlo method was Student's[2] (William Sealy Gosset) 1908 discovery of the form of the t-distribution through a combination of mathematical and empirical work with random numbers. Kalos & Whitlock[3] review other early applications of random number sampling.

The first modern applications of the Monte Carlo method were related to particle physics and particularly to neutron diffusion and the development of thermonuclear weapons. Enrico Fermi in the 1930's used Monte Carlo methods in the calculation of neutron diffusion, and later designed the Fermiac, a Monte Carlo mechanical device used

in the calculation of criticality in nuclear reactors[4]. During the 1940's, John Von Neumann and Stanislaw Ulam established the mathematical basis for probability density functions, inverse cumulative distribution functions, and pseudorandom number generators. In late 1946 at the Los Alamo National Laboratory (LANL), Stanislaw Ulam suggested the use of random sampling to simulate the flight paths of neutrons, and John von Neumann developed a detailed proposal in early 1947[5]. The name "Monte Carlo" was coined by Nicholas Metropolis, also working at LANL, as a reference to the similarities of statistical simulations and games of chance and because the capital of Monaco was renowned for its casinos. The code that was to become the "Monte Carlo" method of calculation originated from a synthesis of the works of Metropolis and Ulam published in 1949[6]. The 1953 Monte Carlo *Metropolis Algorithm*[7], was cited as being one of the top 10 algorithms having the "greatest influence on the development and practice of science and engineering in the 20th century" by *Computing in Science and Engineering*[8]. In 1952, the first application of Monte Carlo methods to study particle shower production was implemented by Wilson[9]. This work served as a basis for the use of Monte Carlo techniques in the field of medical radiation physics.

Statistical simulation methods may be contrasted to conventional numerical discretization methods, which typically are applied to ordinary or partial differential equations that describe some underlying physical or mathematical system. In many applications of Monte Carlo, the physical process is simulated directly, and there is no need to even write down the differential equations that describe the behavior of the system. This can be achieved through the description of the system by probability density functions (PDFs). The accurate knowledge of the PDFs of a system is of extreme importance since the simulation of the system is undertaken by random sampling the

PDFs. Since it is not feasible to achieve perfect random sampling of a function, a pseudo-random number generator (RNG) code is used. The RNG produces sequences of pseudo-random numbers that are dependent on the initial seed of the sequence. A given seed will always produce the exact same sequence, hence the same simulation results. An important quality of a RNG is its periodicity. A longer periodicity lowers the risk of reusing a pseudo-random number in the course of a lengthy simulation, which would skew the results. The evolution of a system from an initial to a final state is called its history. A Monte Carlo simulation is made up of at least one history but generally the number of histories used can be as high as billions in order to attain low statistical uncertainty. In the course of the histories, physical quantities can be calculated be they micro- or macroscopic. Average values of these quantities and their associated variance can be calculated by summing them over a large number of histories.

Monte Carlo simulations are helpful tools in the fields of medical radiation physics and radiation dosimetry as they can model photon and electron interactions with matter accurately since these interactions have been thoroughly studied and understood (see chapters 2 and 3). Monte Carlo techniques are often used in these fields to calculate absorbed dose, kerma, photon or electron fluence and detector-related quantities like ion chamber response. Monte Carlo can also yield results not available through experiment like the fraction of primary and scattered doses to a region of interest, the proportion of the different interactions and the calculation of different correction factors.

Typically, a Monte Carlo software suite tailored for use in medical radiation physics will include the following components: (1) cross-section data for photons, electrons and positrons, (2) transport algorithms, (3) geometry modeling capacity and (4) simulation data analysis tools. Several Monte Carlo systems are suited for use in medical radiation

physics. The best known systems are ETRAN (Electron TRANsport)[10], ITS (Integrated TIGER Series)[11], MCNP (Monte Carlo N-Particle)[12] and the EGS (Electron-Gamma-Shower) series[13-15]. In this study, we used the last iteration of the EGS family, EGSnrc[15].

2. *EGS Monte Carlo Code System*

EGS (Electron-Gamma-Shower) is a Monte Carlo computer software which simulates the interactions of photons, electrons and positrons in matter. It was first developed by Ford and Nelson[16] at the Stanford Linear Accelerator Center (SLAC). The EGS system has gone through several iterations of which EGSnrc is the most recent. EGSnrc was developed by Kawrakow[15] at the National Research Council of Canada (NRCC). EGSnrc is based on the EGS4[14] system, which is widely used in medical physics, but incorporates many improvements pertaining to the condensed history (CH) implementation and underlying cross-sections.

2.1. EGSnrc

EGSnrc is a general purpose Monte Carlo simulation package of coupled photon and electron transport that applies the condensed history (CH) technique. In order to simulate as accurately as possible any cascade of photons and/or electron shower, EGSnrc takes into account numerous physical processes.

For photon transport, EGSnrc takes into account the following interactions:

–Photoelectric absorption;

–Coherent (Rayleigh) scattering;

–Incoherent (Compton) scattering: Klein-Nishina or bound;

–Pair Production.

For electron transport, EGSnrc takes into account the following interactions:

- Bremsstrahlung production;
- Møller (e^-) and Bhabha (e^+) scattering;
- Positron annihilation;
- Continuously slowing down approximation model between discrete interactions.

2.1.1. Photon transport in EGSnrc

Photon transport in EGSnrc can be summarized by a four step process:

(1) determine the distance to the next interaction,

(2) transport on a straight line to the interaction site taking into account the geometry constraints,

(3) decide which interaction takes place,

(4) change energy/direction depending on the corresponding differential cross-section.

The distance the photon has to travel before the next interaction, as seen in Step (1), is sampled by using the mean-free-path λ. The mean-free path is the average distance a particle will travel before undergoing an interaction and is given by

$$\lambda = \frac{1}{\mu} = \frac{A}{N_A \rho_a \sigma_t} \tag{5.1}$$

where μ is the linear attenuation coefficient, A is the molecular mass, N_A is the Avogadro number, ρ is the medium's density and ${}_a\sigma_t$ is the total atomic cross-section. The probability of a photon not interacting over a pathlength s is given by

$$p(s) = e^{-\mu s} \tag{5.2}$$

One then samples s from $p(s)$. This is done by integrating the probability over s

$$c(s) = \int_0^s p(s')ds' = \frac{1-e^{-\mu s}}{\mu} \tag{5.3}$$

and solving $c(s) = r_1 c(\infty)$, which gives

$$s = -\frac{\ln(1-r_1)}{\mu} = -\lambda \ln(1-r_1) \tag{5.4}$$

where r_1 is a uniformly distributed random number between 0 and 1. Equation (1.4) gives the pathlength s over which the photon does not interact i.e. the distance the photon has to travel to get to the next interaction point. The EGSnrc RNG provides the random number r_1. If the photon enters a new medium, the mean-free-path has to be recalculated for the new medium. Once the photon reaches the location of interaction, a decision has to be made about which interaction takes place. The RNG produces a new random number, r_2, and this random number is compared to the various interactions' probabilities (branching ratios). The logic is the following:

- If $r_2 \succ w_{pair}$, then pair production occurs
- Else if $r_2 \succ w_{pair} + w_{inc}$, then Compton scattering occurs
- Else if $r_2 \succ w_{pair} + w_{inc} + w_{coh}$, then Rayleigh scattering occurs
- Else, photoelectric absorption occurs.

Where $w_i = \frac{\sigma_i}{\sigma_{total}}$ is the probability of an interaction of type i occurring. The final state of the photon (energy transferred, scatter direction ...) depends on the interaction process taking place.

2.1.2. Electron transport in EGSnrc

Electron transport in EGSnrc uses the same general method as for photon transport. Steps 1, 3 and 4 are done in a similar fashion than for photons but using electron specific interactions. Step 2 is the most difficult part of electron transport and differs quite heavily from the photon transport method. The main differences between electron and photon transport arise from the fact that electrons interact much more frequently with a medium than photons. This renders discrete simulation of every electron interaction impractical since millions of interactions would have to be simulated resulting in typical simulation times of upward of twenty days (based on approximations by Kawrakow, 2001 EGSnrc course). To address this problem, a condensed history technique (CH) was first introduced by Berger[17] in the sixties. This technique can be described as lumping together several track segments of a *real* electron path in one single *step*. The cumulative effect of elastic and inelastic collisions bundled in one step is taken into account at the end of the step by using appropriate multiple scattering theories. The CH approach is justified since the state of the electron undergoes small changes for each single interaction and a large number of small momentum transfers will result in small deviations from the mean. There exist two types of CH technique. In the Class I CH technique, the particle moves on either a predetermined energy loss grid or a predetermined pathlength grid. Class I CH is implemented in ETRAN, ITS and MCNP. EGSnrc uses a Class II CH technique which means that bremsstrahlung processes and Møller interactions are treated discretely as long as the energy of the secondary particle is above a user-determined threshold. When the secondary particle's energy lies below the threshold, the interaction is "grouped" into the condensed step which is governed by a continuous slowing down approximation (CSDA)

model. In EGSnrc, the user-determined thresholds are named AP and AE where AP is the bremsstrahlung threshold energy and AE is the inelastic collision threshold energy.

2.1.3. EGSnrc vs. EGS4

The EGSnrc Monte Carlo package is the result of a substantial reworking of the EGS4 system. This overhaul was deemed necessary because of the limits, incapacities and/or failures of EGS4 to reproduce experimental results in certain conditions. Some of these limits were the step-size dependency of simulation results[18], the incapacity to converge to the right answer for small step-sizes in certain conditions[19], possible incorrect energy deposition near boundaries[20] and other interface artifacts[21, 22]. To correct these shortcomings, modifications were applied to EGS4 along two axes: (1) improvement of the CH technique implementation and (2) improved treatment of various physical processes.

The CH technique implementation was improved in EGSnrc by substituting the EGS4 electron transport algorithm, PRESTA (Parameter Reduced Electron STep Algorithm), with a new one. PRESTA-II is a new electron transport algorithm[15, 23, 24] which uses a new multiple scattering theory based on screened Rutherford scattering cross-sections[15, 23, 25], an exact boundary crossing algorithm[15, 23] and an exact evaluation of energy loss due to sub-threshold processes[15, 23]. The implementation of PRESTA-II in EGSnrc produces step-size independent and artifact free electron transport results[26].

To complement the introduction of PRESTA-II, the implementations of various physical processes were revisited. Electron transport was improved by, the modeling of electron relativistic spin effects, the implementation of NIST bremsstrahlung cross-sections data (yielding ICRU 37 radiative stopping powers[27]) and an improved angular

distribution sampling of bremsstrahlung radiation. Photon transport was also improved, most notably in the low energy range which is of special interest to us. Incoherent scattering in EGSnrc takes into account binding effects through a fictitious cross-section method, while EGS4 only supported the Klein-Nishina treatment of incoherent scattering. Photoelectric absorption has also been modified. When a photoeffect interaction occurs, EGSnrc explicitly samples the element of a mixture, instead of using an effective Z for the mixture as in EGS4, and explicitly samples the shell of interaction of the selected element, while EGS4 takes for granted a K-shell interaction. Incoherent scattering and photoelectric absorption induce vacancies in electronic shells which lead to atomic relaxation processes. EGSnrc's implementation of atomic relaxation allows K, L, M and N-shell relaxations and the production of characteristic X-rays, Auger and Coster-Kronig electrons. EGS4 would only allow K-shell relaxation through characteristic X-rays. In-depth description of EGSnrc improvements are given by Kawrakow and Rogers[23].

2.1.4. EGSnrc structure

EGSnrc is structured as a two-layer Monte Carlo package. The EGSnrc flow chart (Figure 4-1) shows the EGSnrc structure: a core *EGS code* layer on top of which sits a *user code* layer. The *EGS code* layer is the physics engine while the *user code* layer can be seen as the interface through which the user interacts with the EGS code. A user code consists of a MAIN program and the subroutines HOWNEAR, HOWFAR and AUSGAB. HOWFAR and HOWNEAR subroutines specify the geometry of the system while AUSGAB is the scoring and simulation output subroutine. The user's input parameters are entered through MAIN which passes them to the EGS code layer.

The EGSnrc distribution comes with a suite of user codes. In this study, we frequently used the following EGSnrc user codes: DOSRZnrc, CAVRZnrc and FLURZnrc. These codes simulate photon and electron beams in a cylindrical geometry (RZ). The first two user codes are mainly used to score dose or kerma in arbitrary geometries (DOSRZnrc) or in cavities (CAVRZnrc) while FLURZnrc is a fluence scoring code. These user codes require for their execution an input file which contains the parameters necessary for the simulation such as the geometry, radiation source type and the Monte Carlo parameters.

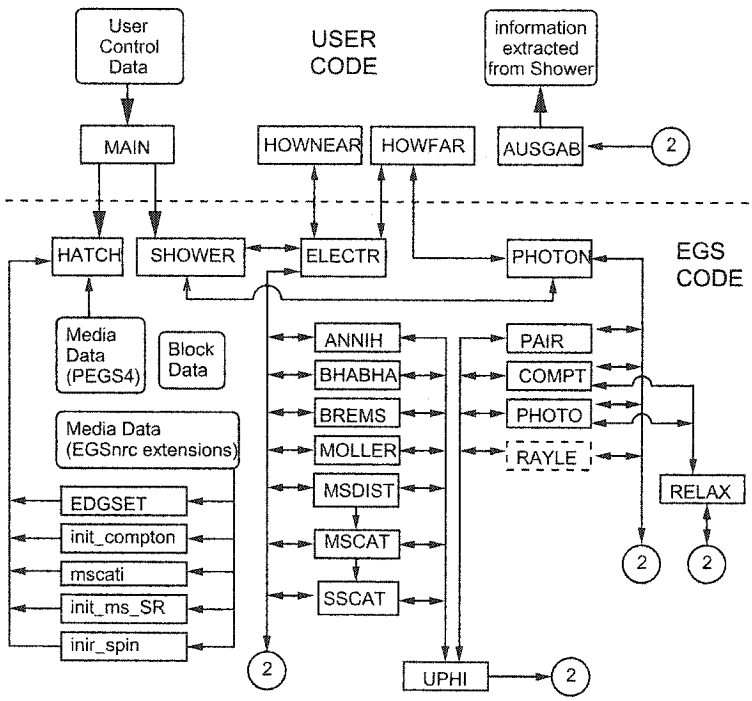

Figure 5-1. The structure of the EGSnrc code system (Kawrakow and Rogers, 2001[23]).

3. *Monte Carlo calculations of ion chamber response*

Calculation of ion chamber response using condensed history Monte Carlo techniques is traditionally considered to be one of the most stringent tests of the way the code handles the electron transport[28]. Inaccuracies in the handling of the electron transport usually show up as dependencies of the result on the electron step size. In EGS4

terminology, one would traditionally perform a study of the results for different values of ESTEPE (the maximum fractional energy loss per step allowed) or impose an SMAX (a maximum step length allowed). With the goal to perform reliable calculations of ion chamber response, the PRESTA algorithm was developed[29, 30] to resolve the so called step-size artifact. For a large class of problems, this algorithm indeed relaxed restrictions on step size that otherwise would provoke calculation errors or a prohibitively intensive CPU time consumption. For a while after PRESTA's development with the limited CPU power available, it seemed that within estimated uncertainties, chamber response could be calculated accurately under appropriate ESTEPE restrictions.

However in 1993, Rogers[19] showed that systematic problems of the order of one percent were still present in chamber response calculations for low Z cavities at ^{60}Co and chamber response was found to be strongly step size dependent for 200 keV photon radiation. The study was performed by comparing Monte Carlo calculated chamber response with Spencer-Attix cavity theory predictions and showed that the Monte Carlo calculations overpredicted the response by 1% for ^{60}Co photons. Contrary to the ^{60}Co results, where it was believed that the Spencer-Attix theory was accurate to better than a few tenths of a percent, an arbitrarily normalized calculation of chamber response at 200 keV was shown, since cavity theory was not expected to be valid at these low energies.

To address these and other known problems (see section 2.1.3 EGSnrc vs EGS4) with the EGS4/PRESTA system, Kawarakow[15, 24-26] developed a new electron transport algorithm and incorporated it, together with other important improvements in photon physics into the new version of EGS, EGSnrc. In an associated paper, Kawrakow[26] proved that, for the ion chamber response problem, EGSnrc produces results consistent at the 0.1% level for Aluminium and Carbon at ^{60}Co energies. The differential effect of

various improvements in the electron transport physics on the calculated chamber response result was studied and quantitative expressions for their magnitudes were given.

To complement this last study, Seuntjens and colleagues[31] published an article in which they discuss the accuracy to which ion chamber response in low energy photon beams can be calculated using the Monte Carlo technique. In that study, they examined the consistency of Monte Carlo calculated ion chamber response in the kilovoltage energy region. To this end they performed ion chamber response calculations for a Fano cavity implementation, where the expected result is known from theory, and they compared EGSnrc with its predecessor EGS4/PRESTA 1.2. On average, EGSnrc was found to be consistent to within 0.03% whereas the former EGS version was stepsize and transport cutoff dependent from anywhere between –5% to +3% in the Fano response calculation. They also studied ion chamber response calculations in comparison with measurements for two types of chambers: the NRC 3C graphite cavity ionization chamber and the Exradin A12 ionization chamber. For average energies of 100 keV or higher they report excellent agreement between measured and calculated ionization chamber response. For energies lower than 100 keV, the calculated response is generally lower than the measured response by an amount that increases with decreasing energy. They also tested the overall effect of the improvements in cross sections in EGSnrc (binding effects, atomic relaxations and spin effects) and found that these improvements affect the response by between 1% and 2 %.

The present study aims to further improve the agreement of ion chamber response Monte Carlo calculations in low energy photon beams when compared to experimental data.

4. Medical Physics Unit Monte Carlo computer cluster

Monte Carlo calculated quantities and their associated variance are obtained by averaging said quantities over a large number of histories. Since histories are independent from one another, it is possible to divide a total number N of histories in n smaller batches with unique random number seeds and run the n different batches (N/n histories/batch) at different times on different computers. Once completed, the batches are combined to obtain the final result for N histories. Computation time is approximately reduced by n.

The Medical Physics Unit possesses a Monte Carlo computer cluster of twelve Pentium III dual-processor computers (24 CPUs with speeds ranging from 450 MHz to 933 MHz) using the Network Queuing System software for distributing jobs over the cluster. A typical cavity (0.2 cm^2 scoring volume) dose simulation of a parallel-plate ionization chamber with a relative uncertainty on the dose per incident fluence of 0.3% takes 15~20 hours to complete using all 24 processors.

5. References

1 Comte de Buffon, G.L.L., *Essai d'arithmétique morale*, in *Supplément à l'Histoire Naturelle*. 1777.

2 Student, *The Probable Error of a Mean.* Biometrika, 1908. **6**: p. 1-25.

3 Kalos, M.H. and P.A. Whitlock, *Monte Carlo methods*. 1986, New-York: J. Wiley & Sons.

4 Anderson, H.L., *Metropolis, Monte Carlo and the MANIAC.* Los Alamos Science, 1986. **14**: p. 96-108.

5 Ulam, S. and J. von Neumann, *On combination of stochastic and deterministic processes.* Bull. Amer. Math. Soc, 1947. **53**: p. 1120.

6 Metropolis, N. and S. Ulam, *The Monte Carlo method.* Journal of the American Statistical Association, 1949. **44**(247): p. 335-341.

7 Metropolis, N., et al., *Equations of state calculations by fast computing machines.* Journal of Chemical Physics, 1953. **21**: p. 101-121.

8 Editors, J. Dongarra, and F. Sullivan, *Top 10 Algorithms of the Century.* Computing in Science and Engineering, 2000. **2**(1): p. 22-79.

9 Wilson, R.R., *Monte Carlo study of shower production.* Phys. Rev., 1952. **86**: p. 261-269.

10 Berger, M.J. and S.M. Seltzer, *ETRAN, Monte Carlo code system for electron and photon transport through extended media*. 1973, Oak Ridge National Laboratory: Oak Ridge, TN.

[11] Halblieb, J.A. and T.A. Melhorn, *ITS: The Integrated TIGER Series of coupled electron/photon Monte Carlo transport codes*, SAND 84-0573, Sandia National Laboratory, (1984).

[12] Briesmeister, J.F., *MCNP - A General Monte Carlo N-Particle Transport Code*, LA-13709-M, Los Alamos National Laboratory, Los Alamos (2000).

[13] Ford, R.L. and W.R. Nelson, *The EGS code system - Version 3*, SLAC-210, Stanford Linear Accelerator Center, Stanford, Ca (1978).

[14] Nelson, W.R., H. Hirayama, and D.W.O. Rogers, *The EGS4 Code system*, SLAC-256, Stanford Linear Accelerator Center, Stanford, Ca (1985).

[15] Kawrakow, I., *Accurate condensed history Monte Carlo simulation of electron transport. I. EGSnrc, the new EGS4 version.* Med Phys, 2000. **27**(3): p. 485-98.

[16] Bielajew, A.F., et al., *History, overview and recent improvements of EGS4*, PIRS-0436, National Research Council of Canada, Ottawa (1994).

[17] Berger, M.J., *Monte Carlo calculations of the penetration and diffusion of fast charged particles*, in *Methods in Comput. Phys.*, B. Alder, S. Fernbach, and M. Rotenberg, Editors. 1963, Academics: New York. p. 135-215.

[18] Bielajew, A.F. and D.W.O. Rogers, *Electron step-size artefacts and PRESTA*, in *Monte Carlo Transport of Electrons and Photons*, T.M. Jenkins and W.R. Nelson, Editors. 1988, Plenum: New York. p. 115-137.

[19] Rogers, D.W.O., *How accurately can EGS4/PRESTA calculate ion chamber response?* Med. Phys., 1993. **20**: p. 319-323.

[20] Bielajew, A.F., D.W.O. Rogers, and A.E. Nahum, *Monte Carlo simulation of ion chamber response to ^{60}Co - Resolution of anomalies associated with interfaces.* Phys. Med. Biol., 1985. **30**: p. 419-428.

[21] Nahum, A.E., *Simulation of dosimeter response and interface effects*, in *Monte Carlo Transport of Electrons and Photons*, W.R. Nelson, Editor. 1988, Plenum: New York. p. 523-547.

[22] Foote, B.J. and V.G. Smyth, *The modelling of electron multiple-scattering in EGS4/PRESTA and its effect on ionization-chamber response.* Nucl. Instrum. Methods Phys. Res., 1995. **B 100**: p. 22-30.

[23] Kawrakow, I. and D.W.O. Rogers, *The EGSnrc Code System: Monte Carlo simulation of electron and photon transport*, PIRS-701, National Research Council of Canada, Ottawa (2001).

[24] Kawrakow, I. and A.F. Bielajew, *On the condensed history technique for electron transport.* Nucl. Instrum. Methods, 1998. **142B**: p. 253-280.

[25] Kawrakow, I. and A.F. Bielajew, *On the representation of electron multiple elastic-scattering distribution for Monte Carlo calculations.* Nucl. Instrum. Methods, 1998. **134B**: p. 325-336.

[26] Kawrakow, I., *Accurate condensed history Monte Carlo simulation of electron transport. II. Application to ion chamber response simulations.* Med Phys, 2000. **27**(3): p. 499-513.

[27] ICRU, *ICRU Report 37*, International Commission on Radiation Units and Measurements, Washington D.C. (1984).

[28] Nahum, A.E., *Simulation of dosimeter response and interface effects*, in *Monte Carlo Transport of Electrons and Photons*, T.M. Jenkins and W.R. Nelson, Editors. 1989, Plenum: New York. p. 523-547.

[29] Bielajew, A.F. and D.W.O. Rogers, *PRESTA: The Parameter Reduced Electron-Step Transport Algorithm for electron Monte Carlo transport.* Nuclear Instruments and Methods, 1987(B18): p. 165 – 181.

[30] Bielajew, A.F. and D.W.O. Rogers, *PRESTA: The Parameter Reduced Electron-Step Transport Algorithm for electron Monte Carlo transport*, PIRS-0042, National Research Council of Canada, Ottawa (1986).

[31] Seuntjens, J.P., et al. *Calculated and measured air-kerma response of ionization chambers in low and medium energy photon beams.* in *International Workshop on Recent Developments in Accurate Radiation Dosimetry*. 2002. Montreal, Quebec, Canada: Medical Physics Publishing, Madison.

Chapter 6

Monte Carlo study of ion chamber response in low energy photon beams

1. Introduction

In this chapter, we will present EGSnrc[1] Monte Carlo calculations of ion chamber response for a commercially available parallel-plate cavity ionization chamber in low energy photon beams. The calculations will be compared to experimental data and we will try to assess the usefulness of commercial parallel-plate chambers for low energy photon air kerma measurements as well as test the accuracy of the EGSnrc Monte Carlo code at very low photon energies.

2. Ion chamber response and Monte Carlo calculations

Ion chamber response is defined as the average absorbed dose to the cavity gas of an ionization chamber, D_{gas}, positioned with its effective point of measurement at a reference point divided by air-kerma measured free-in-air ($K_{free\text{-}air}$) at that same reference point.

$$R = \frac{D_{gas}}{K_{free-air}} \tag{5.5}$$

For chambers fulfilling Bragg-Gray conditions, ion chamber response is traditionally calculated using the Spencer-Attix cavity theory. At low photon energies however, Spencer-Attix cavity theory breaks down and Monte Carlo response calculations constitute an important alternative.

Calculation of ion chamber response using condensed history Monte Carlo techniques is traditionally considered to be one of the most stringent tests of the way the code

handles the electron transport[2]. Up until recently, chamber response calculations using condensed-history Monte Carlo systems were inaccurate due to various approximations in the electron transport physics. Recently however, the accuracy of EGSnrc calculated response was tested for gas-filled cavities under Fano conditions (see Chapter 4, Section 2.6), that is, the cavity being filled with gaseous wall material and attenuation and scattering of the primary beam in the chamber wall being corrected for. In such test, the consistency of the transport was tested, independently of underlying cross-section data, and shown to be in agreement with the Fano theorem[3, 4]. For realistic air-filled chambers, however, the air-kerma response is also affected by (1) the accuracy of the cross section data used; (2) the accuracy of the chamber material specification and (3) the accuracy of the radiation source. Borg *et al.*[5] reported discrepancies of about 3% for energies below 100 keV between EGSnrc calculated mass energy-absorption coefficients of air and graphite with the accepted values of Hubbell and Seltzer[6] while values above 300 keV agree within 0.4% with the Hubbell and Seltzer data. It appears that photoeffect is an important interaction in air and graphite at energies below 100 keV. The standard EGSnrc distribution uses photoeffect cross-sections from the Storm and Israel (S&I) tables[7] while the mass energy-absorption coefficients from Hubbell and Seltzer are based on the XCOM[8] photon cross-section database[9] which uses different photoeffect cross-sections. In order to meet condition (1) for realistic Monte Carlo calculated air kerma ion chamber response, we have implemented XCOM photoelectric cross-sections in EGSnrc.

3. *Implementation of XCOM photoelectric cross-section in EGSnrc*

EGSnrc uses different approaches to gather the total cross-sections for the different possible photon interactions. Whereas total Compton cross-sections are calculated at run

time, the total photoeffect cross-section is interpolated from data stored in a preparation file with a sometimes inadequate energy grid. More importantly, in the standard EGSnrc distribution, these latter data use a data package by Storm and Israel (S&I) dating back to the early 70's. We now present a simple implementation of NIST XCOM-based photoeffect cross-sections in EGSnrc and study the effect on relevant dosimetric quantities calculated with EGSnrc, *i.e.*, mass energy-absorption coefficients, absorbed dose from point sources and ion chamber response.

3.1. Material and methods

Implementation of new photoeffect data requires modification of the pgs4pepr.dat file which contains these basic data along with pair production cross-sections for elements Z=1 to Z=100. In the standard version of EGSnrc, the pgs4pepr.dat file contains photoeffect cross-sections as tabulated by Storm & Israel in 1970[7]. The file is laid out as follows: a header containing information on the number of bins available for each element (maximum is 61 bins/element), the full list of element specific energy grids spanning a 1 keV to 100 MeV range and the last section contains the list of element specific photoeffect cross-sections. For all elements, we updated the photoeffect cross-section values of the pgs4pepr.dat file with the XCOM total photoeffect absorption cross-sections taken from the NIST web version[9] of the XCOM software. The updated pgs4pepr.dat file is labeled pgs4pepr_xcom.dat.

It has to be understood that the cross-section file pgs4pepr.dat is not used at runtime by EGSnrc. Instead, it is the *master* elemental cross-section data file used by the PEGS4 preprocessor which will actually compose the cross-section data for each necessary material (compounds or mixtures) used for a given simulation. The different material

photoelectric cross-sections are read from the pegs4dat file (created by PEGS4) of the said materials and loaded by EGSnrc through the HATCH process. This implies that the photoelectric data used at runtime by EGSnrc is solely contained by the .pegs4dat media files. It is then possible for multiple photoelectric cross-section datasets to coexist in EGSnrc. One only has to produce materials through the PEGS4 routine using either the standard pgs4pepr.dat file or a modified cross-section data file, pgs4pepr_xcom.dat in our case. This would result in two files prepared for the same medium with different photoelectric data, e.g. water.pegs4dat and waterXCOM.pegs4dat.

3.1.1. Cross-section datasets

Comparison of the two photoeffect datasets was undertaken for all 100 elements contained in the data files. Figure 6-1 presents cross-section ratios S&I/XCOM of dosimetrically important low-Z elements in an energy range (1 keV to 100 keV) where photoeffect absorption is an important photon interaction. This figure shows the XCOM photoeffect cross-sections being systematically larger by up to 5% when compared to the S&I cross-sections for energies higher than 6 keV. This behavior extends to the 100 elements and over the complete energy range (up to 100 MeV) contained in the data files. For higher Z elements, the increase in cross-section can be as high as 10% when going from S&I to XCOM dataset. The uncertainties associated with the S&I/XCOM cross-section ratio can be as high as 0.5% and is mainly due to the low number of significant digits given by the XCOM database cross-sections. The differences between datasets near absorption edges, as shown by the 3.203 keV argon K-edge, can be as high as 6% to 10%. The ratio curve for hydrogen ends at 10.5 keV since no cross-section values were contained for higher energies in the S&I pgs4pepr.dat file.

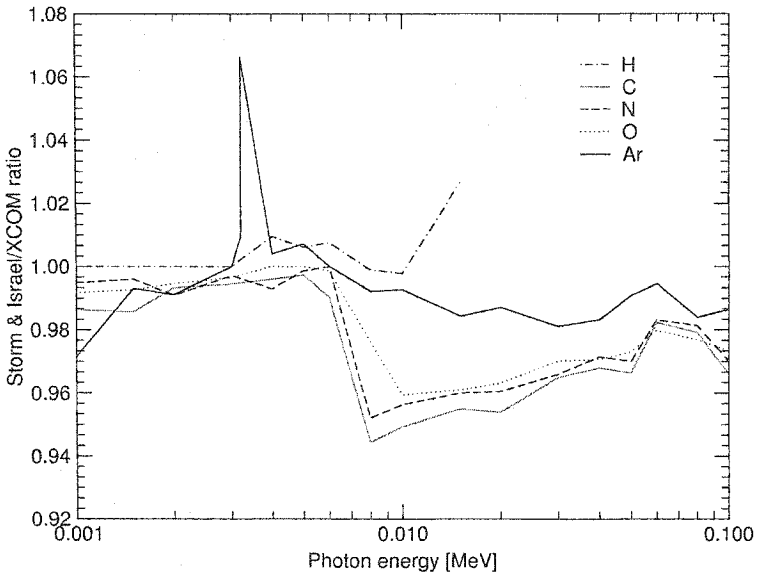

Figure 6-1. Ratio of Storm & Israel (S&I) over XCOM photoeffect cross-sections for low-Z dosimetrically important elements. XCOM cross-sections are larger than S&I by up to 5%. Discrepancies between datasets are maximal around absorption edges, here 3.203 keV argon K-edge.

3.1.2. Validation

The implementation of XCOM photoelectric cross-sections in EGSnrc was validated in two ways. Firstly, the content of the pgspepr_xcom.dat file was verified and compared with the original file. This verification resulted in the correction of a small number (3) of missing or shifted values. Secondly, PHOTXsection, an EGSnrc user code, was written to quantify the overall accuracy of the implemented new data within the constraints of EGSnrc. These constraints are the availability of only a limited number of intervals to fit and interpolate the cross-section data in EGSnrc which also leads to systematic errors not discussed in this study. PHOTXsection calculates the absorption coefficients of the different photon interactions: coherent (Rayleigh) scattering, incoherent scattering (Klein-Nishina or bound), photoelectric absorption and pair production. It does so by counting the number of primary photon interactions in a thin slab of medium and the number of primary photons coming through the slab without interacting. The thickness of the slab is

automatically chosen as a function of the gamma mean free path for any given energy. This is done to optimize statistical uncertainties by balancing the number of primary photons traversing the slab and the number of photon interactions in the slab. Appendix A contains the source code of the PHOTXsection user code and a more detailed description of its operation. As shown in Figure 6-2, the photoeffect cross-sections calculated by PHOTXsection using XCOM data agree within ±1% with the NIST XCOM cross-sections for compounds or elements when an interval [AP=1 keV, UP=2 MeV] is used. This result slightly improves when an interval [AP=1 keV, UP=150 keV] is used. The high differences between calculated and XCOM values can be partly explained by the low number of significant digits given in the XCOM cross-section database (significant digits uncertainty can be of the order of 0.5%).

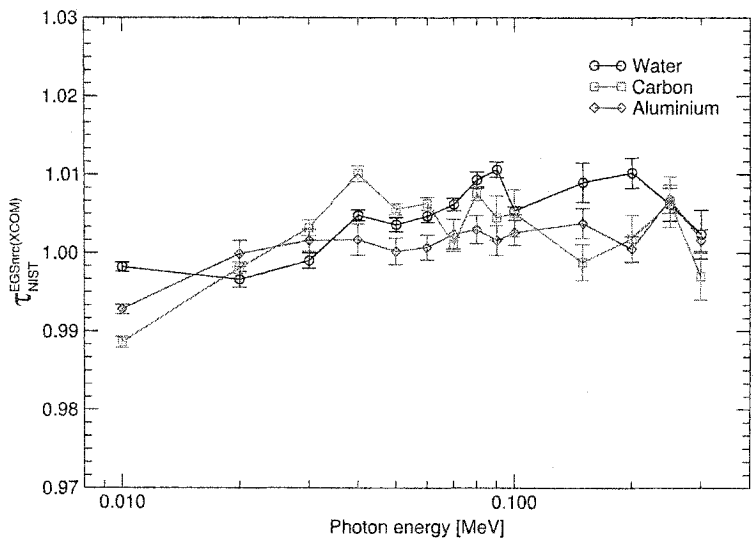

Figure 6-2. Ratio of EGSnrc(XCOM) calculated photoeffect cross-sections by NIST database cross-sections. The calculated cross-sections with AP=1 keV, UP=2 MeV agree within ±1% with the NIST cross-sections.

3.1.3. Dosimetric quantities

3.1.3.A. Mass energy-absorption coefficients

Using the XCOM data in EGSnrc, mass-energy transfer and mass-energy absorption coefficients were calculated. Kerma was obtained by calculating energy deposition by a broad-parallel monoenergetic photon beam in a thin (2 μm) slab of medium of infinite lateral extent. Primary photons are forced to interact in the medium and electron transport is turned off resulting in no energy escaping the slab through bremsstrahlung radiation or electron transport, which implies the scoring of kerma. Mass energy absorption coefficients were derived from mass-energy transfer coefficients using the relation $\mu_{en}/\rho = (\mu_{tr}/\rho)(1-\bar{g})$, where $\bar{g}$ is the fraction of the initial energy expended in radiative interactions upon electron slowing down in an infinite medium. The $\bar{g}$ value is calculated as the ratio of all the energy radiated by the electrons created from the monoenergetic photons and the energy transferred from the photons to the electrons.

3.1.3.B. Inverse square corrected radial dose distributions

Point sources emitting very low monoenergetic photons (10 keV to 50 keV) were simulated in water using a spherical scoring user code named KERNEL. This user code outputs radial depth dose distributions corrected for the inverse-square law fluence reduction.

3.1.3.C. Calculation of ion chamber response

Response was calculated for an Exradin A11 parallel-plate ion chamber for which detailed drawings were obtained from the manufacturer (Standard Imaging, Middleton). The chamber mainly consists of C552 air-equivalent plastic, in particular the entrance window (1 mm thickness) and the collecting plate, and its nominal collection volume is 0.6 cm^3. Monoenergetic photon point sources of energy 15 keV to 200 keV and a source to cavity distance of 100 cm yielding a field radius of 2.2225 cm at the chamber plane were used. The user code CAVRZnrc was used to calculate dose to the cavity gas, D_{gas}. Air kerma free in air, $K_{free\text{-}air}$, at one meter in air was obtained by determining the photon energy fluence spectrum at the point of measurement using FLURZnrc and calculating $K_{free\text{-}air}$ by integrating the energy fluence spectrum and mass-energy transfer coefficients (from the appropriate dataset) over the energy range of the spectrum.

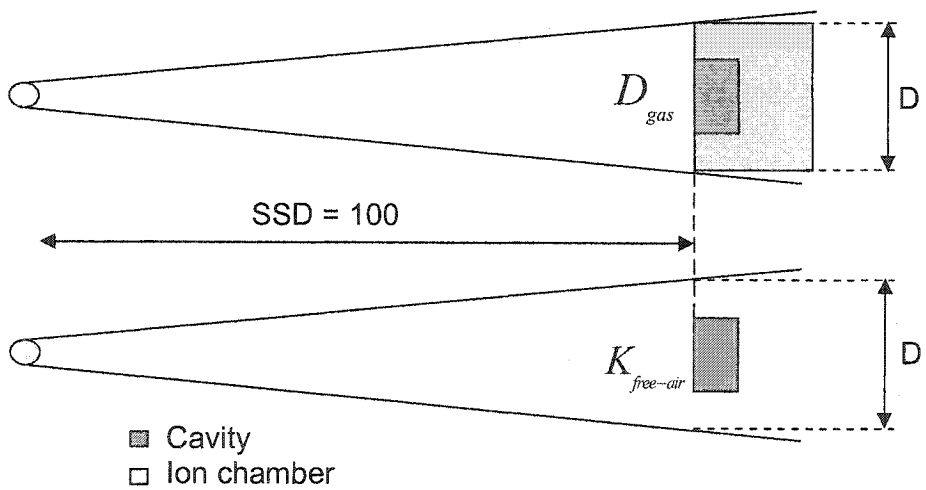

Figure 6-3. Ion chamber response simulation geometry. Shown are the geometries used to calculate D_{gas} and $K_{free\text{-}air}$. In both cases, air is the surrounding medium. The D_{gas} calculation involves the whole ion chamber while $K_{free\text{-}air}$ is calculated at the same position but without the actual chamber (measured free in air).The diameter of the radiation field (D=4.445 cm) is equal to the chamber diameter.

3.1.4. EGSnrc transport parameters

All EGSnrc calculations used the following photon transport parameters: AP=PCUT=1 keV, bound Compton scattering, Rayleigh scattering and atomic relaxations after all photon interactions. Electron transport was simulated by the PRESTA-II algorithm with the parameters: AE=1 keV, ECUT=512 keV, photo-electron angular sampling and spin effects turned on. Point source radial dose distribution calculations used the above parameters while mass-energy transfer calculations did not use electron transport (ECUT=20.512 MeV).

3.2. Results and discussion

3.2.1. Mass-energy absorption coefficients

Figure 6-3 shows the ratio of mass-energy absorption coefficients of air calculated using EGSnrc with either the S&I [EGSnrc(S&I)] or the XCOM [EGSnrc(XCOM)] cross-section datasets to the Hubbell and Seltzer NIST (μ_{en}/ρ) tables. Consistent with the differences in basic photoeffect data, in the 6 keV to 100 keV energy range, the EGSnrc(S&I) calculated (μ_{en}/ρ) show discrepancies of up to 4% with the NIST database in agreement with results by Borg *et al.*[5] . When using EGSnrc(XCOM), calculated (μ_{en}/ρ) show excellent agreement, within ±0.5% in air and ±1% in water (result not shown), with the NIST data over the same energy range. The 3.2 keV peak in Figure 6-3 is due to EGSnrc interpolation artefacts close to the absorption edge (argon in this case).

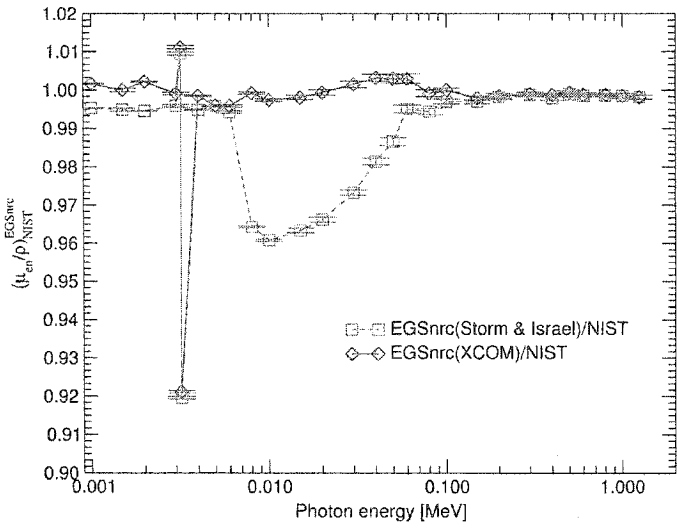

Figure 6-4. Comparison of mass energy-absorption coefficients of air calculated using EGSnrc(S&I) and EGSnrc(XCOM) to the NIST database. EGSnrc(S&I) coefficients are off by up to 4% from the NIST data in the 6 keV to 100 keV range while EGSnrc(XCOM) results are in excellent agreement with NIST data.

3.2.2. Inverse-square corrected dose distributions from point sources

Since low photon energy brachytherapy is a domain for which the implementation of XCOM photoeffect cross-sections in EGSnrc should be beneficial, we calculated and compared kernel radial-depth dose distributions using both photoeffect datasets. We simulated monoenergetic point sources immersed in water over a photon energy range of 10 keV to 50 keV using KERNEL. Figure 6-4 shows the unnormalized calculated radial-depth dose distributions. EGSnrc(XCOM) calculated distributions are shown in solid lines while the dotted lines represent EGSnrc(S&I) distributions. Figure 6-4 demonstrates that EGSnrc(XCOM) calculated doses near the source (r~0 cm) are 3% larger for the 10 keV source when compared to the EGSnrc(S&I) doses. This difference decreases down to 1% at 50 keV as Compton scattering interactions become more frequent. This result is explained by the XCOM photoeffect cross-sections being larger than their S&I counterparts which leads to an increase in photoeffect interactions and in turn to an increase in dose near the source. The larger XCOM cross-sections also lead to a higher

attenuation effect which renders the EGSnrc(XCOM) calculated distributions less penetrating than the EGSnrc(S&I) distributions. This is seen in Figure 6-4 when the XCOM and S&I distributions cross-over (see Fig 6-5, inset).

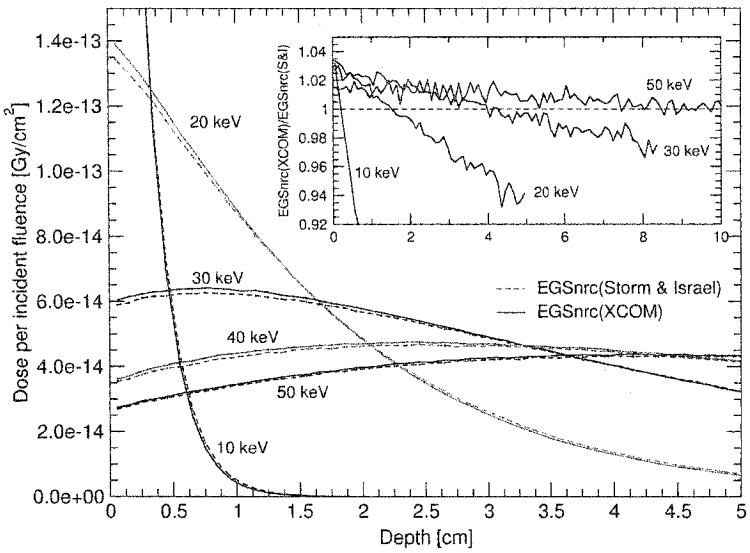

Figure 6-5. Comparison of calculated, inverse-square corrected, radial-dose curves for monoenergetic point sources in water using EGSnrc(S&I) and EGSnrc(XCOM). Doses calculated near the source with XCOM are 1% to 3% higher compared to EGSnrc(S&I) calculated doses.

3.2.3. Ion chamber response

In the present section, where we focus on the effect of changing cross-section datasets, we compare EGSnrc(XCOM) and EGSnrc(S&I) calculated ion chamber responses for the Exradin A11 parallel-plate chamber in 15 to 200 keV monoenergetic photon beams in air. Figure 6-5 shows the result for an Exradin A11 chamber, consisting of pure C552 plastic[10]. EGSnrc(XCOM) responses are represented by diamond symbols and solid line, EGSnrc(S&I) responses are shown by circle symbols and dotted line. The inset shows the ratio EGSnrc(XCOM)/EGSnrc(S&I) of calculated responses. At the lower energies, EGSnrc(XCOM) calculated responses are up to 1% lower than EGSnrc(S&I) calculated responses.

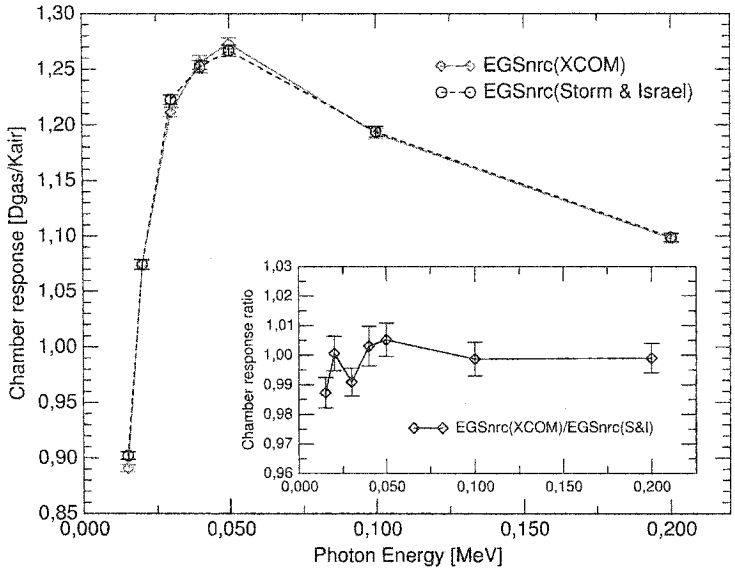

Figure 6-6. Ion chamber response of an Exradin A11 chamber for monoenergetic photon beams calculated using EGSnrc(S&I) and EGSnrc(XCOM). Insert: ratio (XCOM/S&I) of chamber response. Chamber C552 plastic is not contaminated with high-Z impurities.

Since the response calculations are executed at very low energies, any trace of high-Z impurities in the chamber materials potentially has effects on the chamber response because the photoeffect cross-sections rapidly increase with Z. In an investigation by Barnard *et al.* (1964) at the National Physical Laboratory (UK), it was found that trace impurities resulting from the machining process of the ion chamber play a dramatical role in the chamber response[11]. Seuntjens *et al.* (2002) submitted a C552 fragment of an Exradin A12 parallel-plate chamber to a mass spectrometry analysis in order to estimate the effect of impurities on the response of the A12 chamber[4]. The analysis revealed that the amount of impurities with Z values ranging from 10 to 82 was 90 μg/g. The incorporation, by Seuntjens *et al.*, of the high-Z impurities in C552 improved their overall agreement between response calculations and experiments[4]. We have incorporated the high-Z impurities revealed in that analysis to the C552 plastic of the A11 chamber. Figure 6-6 shows that response in the presence of high-Z impurities is increased by 2% or less at

30 – 50 kV and this conclusion is not significantly altered by the data set used: $EGSnrc(XCOM)_{imp}$ responses are up to 1% lower than $EGSnrc(S\&I)_{imp}$ calculated responses.

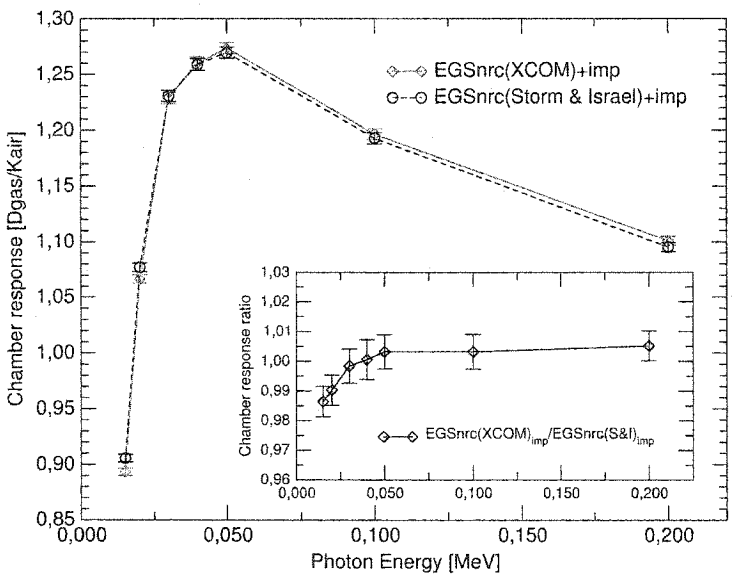

Figure 6-7. Ion chamber response of an Exradin A11 chamber for monoenergetic photon beams calculated using EGSnrc(S&I) and EGSnrc(XCOM).). Insert: ratio (XCOM/S&I) of chamber response. Presence of high-Z impurities (90 μg/g) in the chamber's C552 plastic.

3.3. Summary: Implementation of XCOM photoelectric cross-sections in EGSnrc

XCOM photoeffect cross-sections were implemented in the EGSnrc Monte-Carlo system. We have shown that this implementation modifies EGSnrc calculated results of various low energy dosimetric quantities. Mass-energy absorption coefficients calculated using Storm & Israel cross-sections show differences of up to 4% compared to the NIST absorption coefficient database while XCOM calculated mass-energy absorption coefficients are in agreement with NIST data. EGSnrc(XCOM) radial-depth dose distributions of monoenergetic sources (10 to 50 keV) in water are less penetrating (by 1% to 2%) but have higher dose near the source (1% to 3%) when compared to

EGSnrc(S&I). Ion chamber responses calculated using XCOM and pure materials are 1% lower than S&I calculated responses and this conclusion is not modified when a realistic amount of high-Z impurities are uniformly present in the chamber's C552 plastic. In order to further improve the use of up-to-date cross-section data in EGSnrc, the interpolation of data in general and around absorption edges in particular needs to be addressed.

4. Monte Carlo calculated and experimental ion chamber response

Ion chamber response was calculated using EGSnrc and the results were compared to experimental data measured at Physikalisch-Technische Bundesanstalt (PTB) by Dr Ludwig Buërmann. PTB is the national institute of natural and engineering sciences and the highest technical authority for metrology and physical safety engineering of the Federal Republic of Germany.

4.1. Material and methods

The Exradin A11 parallel-plate ionization chamber was used for the Monte Carlo calculations and the experimental measurements. Experimental air kerma calibration factors, N_K ($N_K = R^{-1}$), for the Exradin A11 (SN 92701) were measured for the X radiation qualities and gamma sources listed in Table 1. The *A* series of X-ray qualities was produced by the PTB DEBYEFLEX 3000 X-ray unit with PHILIPS PW 2184/00 (W-Anode) and the *B* series spectra were produced by an ISOVOLT 320 X-ray unit with MB 350/1. The Exradin A11 chamber was calibrated against the PTB's air kerma primary standards for each radiation quality. For the chamber response measurements, the chamber was positioned at 100 cm from the source and the field diameter in the plane of the chamber was 10 cm for X-ray measurements and 20 cm for gamma ray

measurements. The chamber was fitted with a C552 cap providing an additional buildup thickness of 2 mm for ^{137}Cs and ^{60}Co measurements.

The EGSnrc Monte Carlo chamber response calculations were completed using the protocol as described in Section 3.1.3.C. EGSnrc transport parameters from Section 3.1.4 were used except the *pair production angular sampling* switch has been turned on for ^{60}Co calculations. The radiation sources used in the Monte Carlo simulations were modeled as point sources using the PTB X-ray spectra (see Table 1 and Appendix B), the PTB ^{60}Co spectrum and ^{137}Cs was approximated as a 662 keV monoenergetic photon beam.

Radiation quality	Mean energy [keV]
A10	8.5
A15	12
A20	15.8
A25	19.6
A30	24
A40	32.7
A60	47
B40	27.9
B60	42.8
B80	55.1
B110	79.7
B150	107.7
B200	142.8
B250	181.8
B300	216.2
Cs-137	662
Co-60	1250

Table 1. List of PTB X-ray spectra used and their mean photon energy. Peak kilovoltage for each X-ray spectra is given as the number following the series identifier, e.g. B60= 60 kVp. PTB spectra are found in Appendix B.

4.2. Results and discussion

Figure 6-7 shows the experimental and EGSnrc calculated air kerma calibration factors normalized to ^{137}Cs for the Exradin A11 chamber using bare ICRU composition C552 plastic[10] (no impurities). At extremely low energies, hv_{ave} is 8.5 keV, the Monte Carlo calculations do not agree with the measurements. But the agreement in the intermediate energy range is better.

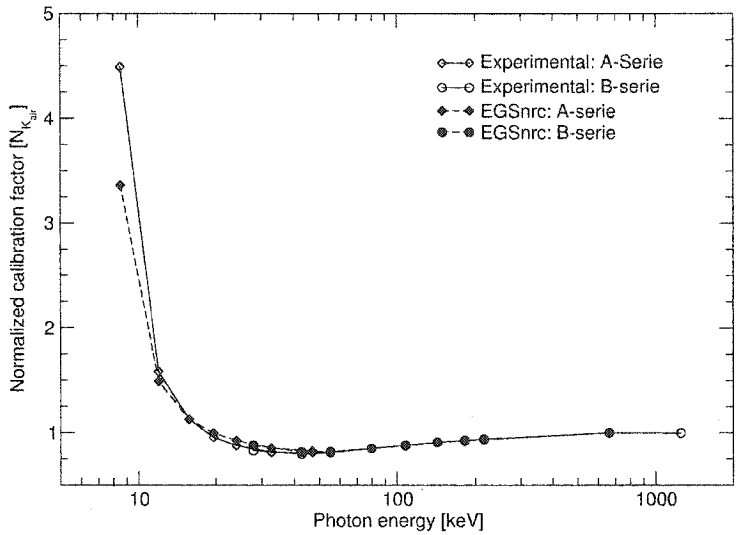

Figure 6-8. Measured and calculated air kerma calibration factors normalized to the value at ^{137}Cs.

Figure 6-8 presents the same series of results but with a finer view of the 11 keV to 200 keV photon energy range. The agreement between calculations and measurements is within ±0.5% until hv_{ave} is 79.7 keV (B110 spectrum) and around ±1% at hv_{ave} 55.1 keV (B80). The agreement then worsens up to 6% at hv_{ave} 27.9 keV (B60 spectrum) and 12 keV (B15 spectrum).

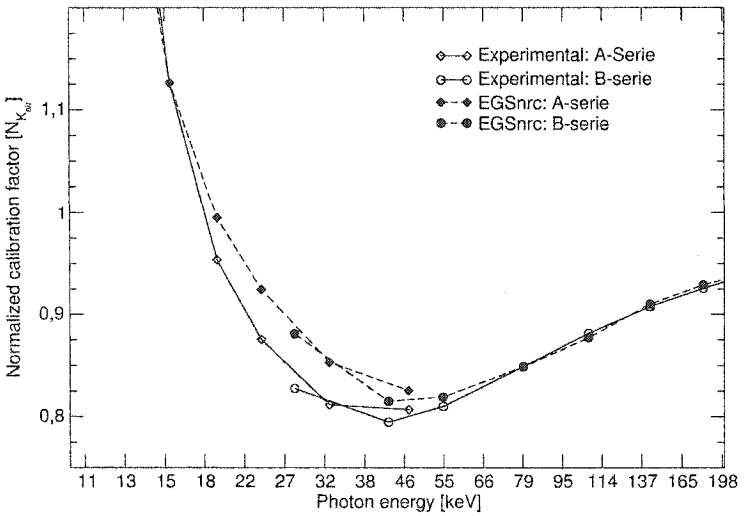

Figure 6-9. Measured and calculated air kerma calibration factors normalized to the value at ^{137}Cs.

Figure 6-9 presents the ion chamber results when high-Z impurities are incorporated in the chamber's C552 plastic. The agreement of the calculations with the measurements seems to have slightly worsened at higher energies but is better at low energies.

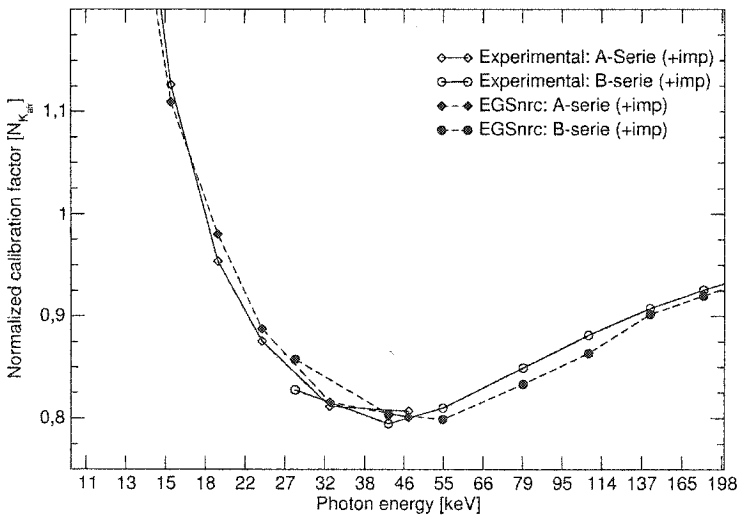

Figure 6-10. Measured and calculated air kerma calibration factors normalized to the value at ^{137}Cs. High-Z impurities are incorporated in the chamber's C552 plastic.

In order to compare the calculations and the measurements more directly, Figure 6-10 presents ratios of calibration factors $N_k(EGSnrc)/N_k(\exp)$. Figure 6-10, shows the EGSnrc(imp) calculations agreeing to a higher degree with experiment at lower energies.

The largest discrepancy between the EGSnrc(imp) calculations and the measurements for the B-series of spectra is 3.6% at B40 ($h\nu_{ave}$ = 27.9 keV) while the EGSnrc(pure) calculations show a disagreement of the order of 6%. The same behavior is witnessed at the lower energy A-series of spectra. It is evident from Figure 6-10 that the incorporation of high-Z impurities in the chamber's material leads to a more realistic Monte Carlo calculation and better general agreement with experiment.

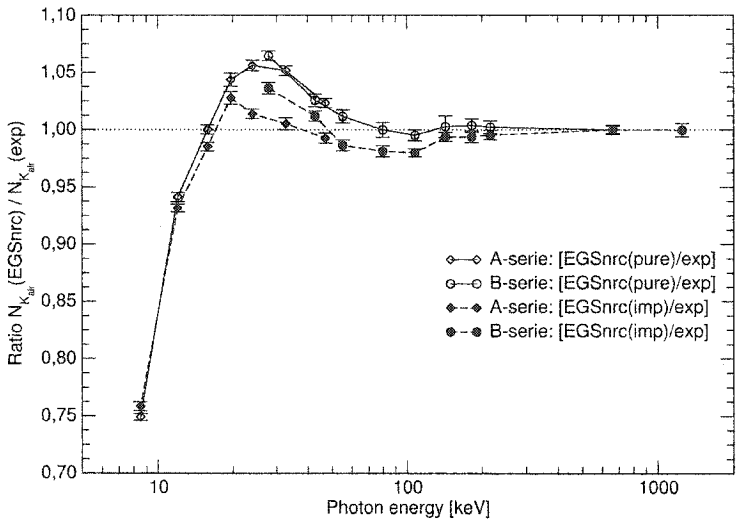

Figure 6-11. Ratios of air kerma calibration factors $N_K(EGSnrc)/N_K(exp)$.

5. Conclusion

XCOM photoeffect cross-sections were implemented in the EGSnrc Monte-Carlo system. We have shown that this implementation modifies EGSnrc calculated results of various low energy dosimetric quantities. Realistic calculations of ion chamber response were undertaken using the EGSnrc Monte Carlo code with the new XCOM implementation. The results show good agreement with the measurements at the ±4% level at average spectra energies as low as 30 keV. Given these results, the EGSnrc Monte Carlo system seems suitable for ion chamber response in low energy x-ray spectra of average energy around 50 keV at the ±1% level. Although these results improve on

previous studies, improvements can still be made. These improvements can be made in several fields: (1) the simulation geometry, such as a detailed description of the chamber stem; (2) the low energy photo-electron physics, such as a more realistic simulation of the photo-electron angular distribution.

6. References

[1] Kawrakow, I., Accurate condensed history Monte Carlo simulation of electron transport. I. EGSnrc, the new EGS4 version, Med Phys 27 3 (2000) 485-98.

[2] Nahum, A.E., *Simulation of dosimeter response and interface effects*, in *Monte Carlo Transport of Electrons and Photons*, T.M. Jenkins, W.R. Nelson, Editors. 1988, Plenum: New York. p. 523-547.

[3] Kawrakow, I., Accurate condensed history Monte Carlo simulation of electron transport. II. Application to ion chamber response simulations, Med Phys 27 3 (2000) 499-513.

[4] Seuntjens, J.P., et al. *Calculated and measured air-kerma response of ionization chambers in low and medium energy photon beams*. Proceedings of the International Workshop on Recent Developments in Accurate Radiation Dosimetry. 2002. Montreal, Quebec, Canada: Medical Physics Publishing, Madison [in print].

[5] Borg, J., et al., Monte Carlo study of correction factors for Spencer--Attix cavity theory at photon energies at or above 100 keV, Med. Phys. 27 (2000) 1804 – 1813.

[6] Hubbell, J.H., Seltzer, S.M., Tables of x-ray mass attenuation coefficients and mass energy-absorption coefficients 1 keV to 20 MeV for elements Z=1 to 92 and 48 additional substances of dosimetric interest, Rep. NISTIR 5632, NIST, Gaithersburg, MD (1995).

[7] Storm, E., Israel, H.I., Photon cross sections from 1 keV to 100 MeV for elements Z=1 to Z=100, Atomic Data and Nuclear Data Tables 7 (1970) 565-681.

[8] Berger, M.J., Hubbell, J.H., XCOM: photon cross-sections on a personal computer, Rep. NBSIR 87-3597, National Bureau of Standards, (1987).

[9] Berger, M.J., et al., *XCOM: Photon cross section database*. 1999.

[10] Icru, Stopping powers for electrons and positrons, Rep. ICRU Report 37, International Commission on Radiation Units and Measurements, Bethesda, Maryland (1984).

[11] Barnard, G.P., et al., On the Congruity of N.P.L. Exposure Standards, Phys. Med. Biol. 9 (1964) 333-344.

Chapter 7

Conclusion

1. Summary

The main objective of this thesis was to study the accuracy of Monte Carlo simulation as a method to calculate response for low energy photon beams and to assess its usefulness for commercial parallel-plate chambers in low energy photon air kerma measurements.

Because the EGSnrc Monte Carlo system's photoeffect was based on out of date cross-sections, XCOM photoeffect cross-sections were implemented in EGSnrc. We have shown that this implementation modifies EGSnrc calculated results of various low energy dosimetric quantities. Realistic calculations of ion chamber response were undertaken using the EGSnrc Monte Carlo code with the new XCOM implementation. The results show good agreement with the measurements at the ±4% level at average spectra energies as low as 30 keV. Given these results, the EGSnrc Monte Carlo system seems suitable for ion chamber response in low energy x-ray spectra of average energy around 50 keV at the ±1% level. Although these results improve on previous studies, improvements can still be made.

2. Future work

To improve the agreement of calculations with measurements, the simulation geometry could be modified to include a detailed description of the chamber stem. The study of ion chamber response will be expanded to include other commercially available

parallel-plate ionization chambers. A better understanding of ion chamber response in low-energy photon beams leads to more accurate measurement capabilities of these devices and improves our understanding of detailed Monte Carlo radiation transport calculations.

Appendix A

PHOTXsection

This appendix contains a description of the operations, the source code and an input file template of the EGSnrc user code PHOTXsection. PHOTXsection calculates mass attenuation coefficients for the different photon interactions available in EGSnrc namely photoeffect, Compton effect, Rayleigh scattering and pair production.

1. PHOTXsection's origin

PHOTXsection is loosely based on the *Tutor5* user code by D.W.O. Rogers distributed as a user code example with EGSnrc. Tutor5 scores the number of primary (and their average energy), Rayleigh scattered and Compton scattered photons passing through a 5 mm thick slab of water for a 50 keV incident pencil beam of photons. The Tutor5 code uses a very narrow logic which allows relaxation photons created after a Compton interaction to be scored as Compton scattered photons. This logic is acceptable when using a PCUT>10 keV for low Z materials like water but will give erroneous results for low PCUT cases and/or high Z materials when the fluorescence yield is greater (see p.13). Tutor5 also does not count photoeffect and pair production interactions, does not allow the use of other energies and does not allow the use of different slab thicknesses. Tutor5 was not written as a general purpose code and as such was not suited for this study.

2. PHOTXsection

PHOTXsection borrows the slab geometry of Tutor5 but uses a completely rewritten counting logic, allows calculation of coefficients for a list of energies, uses different slab thicknesses for different photon energies, allows the use of an input file and outputs the results to a file. In this section, we will present the main methods used in PHOTXsection to calculate mass attenuation coefficients.

2.1. Calculation of mass attenuation coefficient

Mass attenuation coefficients for each type of photon interactions are calculated by multiplying the total mass attenuation coefficient by the branching ratio specific to a given photon interaction:

$$\left(\frac{\mu}{\rho}\right)_{X,med} = BR_X \cdot \left(\frac{\mu}{\rho}\right)_{total,med} . \tag{1.1}$$

The total mass attenuation coefficient of the slab medium is calculated using this equation:

$$\left(\frac{\mu}{\rho}\right)_{total,med} = \frac{1}{\Delta T}\ln\left(\frac{N_0}{N}\right) \tag{1.2}$$

where ΔT is the slab thickness, N_o is the number of incident photons onto the slab and N is the number of primary photons which passed through the slab without interacting. The branching ratio for a specific photon interaction is given by:

$$BR_X = \frac{N_X}{N_{PHOTO} + N_{Rayl} + N_{Comp} + N_{pair}} \tag{1.3}$$

where BR_X and N_X are the branching ratio and the number of interactions of type X occurring in the slab of medium. This method is implemented in PHOTXsection at "STEP 8 OUTPUT-OF-RESULTS" (p.110).

As seen, the calculation of mass attenuation coefficients for each type of specific photon interactions is straightforward but needs accurate counting capability by the user code. A new counting logic has been coded to address the issues of the Tutor5 counting algorithm.

2.2. Counting logic

The new logic takes into account the basic photon interactions (Rayleigh. Compton, photoeffect and pair production) and the fictitious cross-section method used by EGSnrc for Compton interactions (in effect negating the relaxation problems of Tutor5). The counting logic can be found in the AUSGAB routine (p.113) of the PHOTXsection source code.

PHOTXsection only counts the interactions undergone in the slab by primary photons. To ensure that a photon is a primary, use is made of the LATCH variable. LATCH is a variable which value is passed from a parent particle to all its daughter particles. In PHOTXsection, primary photons are given a LATCH=0. Once a particle is about to undergo an interaction (a call is about to be made to an interaction subroutine), it is given a LATCH=1 and discarded (IDISC=1). This system is pretty solid since the parent particle is discarded *before* the interaction occurs (before the call to the interaction subroutine is executed), so no daughter particles should be produced, but if the interaction still occurs, the daughter particles are given LATCH=1 and cannot be counted as primary photons subsequently. Each primary photon interaction in the slab is counted and

increments the variable associated with the specific interaction, e.g. the variable NPHOTO is the photoeffect count variable. The counting logic is represented in Figure A-1.

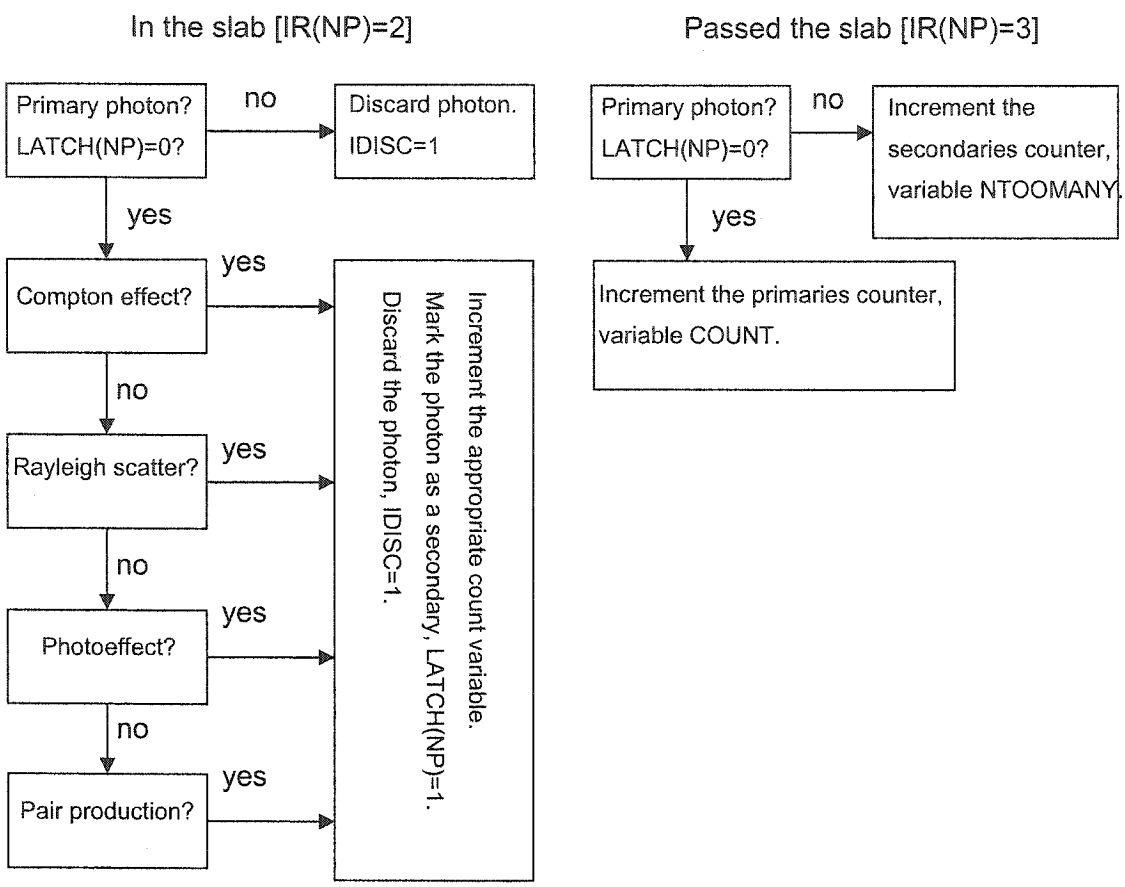

Figure A-1. PHOTXsection counting logic flowchart.

2.3. Compton scatter counting logic

Bound Compton scattering was implemented in EGSnrc by using a fictitious cross-section method. This was done to keep the same general structure as the one used in EGS4. To adequately count the *real* Compton interactions and not *fictitious* Compton events, the counting of Compton interactions has to be done in several steps :

(1) When a call is made to the Compton interaction subroutine, a counter (NCOMP) is incremented.

(2) The Compton subroutine than checks if a Compton interaction occurs or not.

(3) If a Compton event occurs, we set LATCH(NP)=1 and discard the photon.

(4) If a Compton event does not occur, a second counter is incremented (NOCOMP).

This method differs from the one used for the other types of photon interactions where a call to the interaction subroutine implies that an interaction occurs, while the use of the fictitious cross-section method for Compton interactions implies that a call to the Compton subroutine does not necessarily equate to the occurance of a Compton event. Because of that, we have to verify the output of the Compton subroutine. The number of *real* Compton events (NCOMPINT in the code) is given by NCOMPINT=NCOMP-NOCOMP.

2.4. Energy dependent slab thickness

The statistical uncertainty of a mass attenuation coefficient depends on the statistical uncertainties associated with the counting of the primary photons passed the slab and the number of photon interactions in the slab. The thickness of the slab of medium will influence the counting statistical uncertainties, e.g. a thicker slab will result in a higher number of in-slab photon interactions but lower number of primaries passing through, with a consequence of a lower uncertainty for in-slab interactions and higher a uncertainty for primary counting. A thinner slab will give the inverse effects. Since the attenuation coefficient is dependent on both the in-slab interaction counts (through the

branching ratio) and the number of primary photons that travelled through the slab, optimal uncertainties can not be attained by using a fixed slab thickness for all energies.

We have implemented a method which specifies the slab thickness as a function of the gamma mean free-path (GMFP). The GMFP is the mean distance a photon will travel before undergoing an interaction. We have empirically determined that a slab thickness equal to the fourth of the GMFP yields optimal attenuation coefficient uncertainties, i.e. yields the lowest uncertainties for all in-slab interactions as well as traversing photons.

The advantages of this slab thickness specification method are that: (1) the uncertainties are optimal for all energies, (2) a user does not have to find an optimal thickness, the code does it automatically and (3) it permits the calculations of attenuation coefficients for a list of energies automatically. The implementation of the variable slab thickness can be found p.109 in the section entitled "STEP7 SHOWER-CALL".

3. PHOTXsection source code

```
%L
%E    "PHOTXsection.mortran (SID 1.3 last edited 10/05/01)"

!INDENT M 4;   "indent MORTRAN listing 4 per nesting level"
!INDENT F 2;   "indent FORTRAN output 2 per nesting level"

"***************************************************************************"
"                                                                           "
"                    ************************                               "
"                    *                      *                               "
"                    * PHOTXsection.mortran *                               "
"                    *        v0.4          *                               "
"                    ************************                               "
"                                                                           "
"                                                                           "
" An EGSnrc user code which calculates the attenuation coefficient         "
" of different photon interactions. Specifically:                          "
"   Photoelectric interaction                                              "
"   Rayleigh Scattering                                                    "
"   Compton interaction (KN or bound)                                      "
"   Pair Production                                                        "
"      Fadi Hobeila   March 2002                                           "
"                                                                           "
"             -loosely based on tutor5.mortran by D.W.O. Rogers, NRCC "
"***************************************************************************"
$IMPLICIT-NONE;
$INTEGER I,J,k,l,IQIN,IRIN,NCASE,LGLE,LGE,n_energies;
$REAL XIN,YIN,ZIN,UIN,VIN,WIN,WTIN,EIN;
$REAL ANORM,XPHOTO(30),XCOMP(30),
      XRAYL(30),XPAIR(30),XCOMPINT(30),
      BRPHOTO,BRCOMP,BRCOMPINT,BRRAYL,BRPAIR,BRTOT,BRTOTINT,NNORATIO,
      MU,MUTOT(30),MRHO,MRHOINPUT;
real*8 NCROSS,NCROSSINT,NDUPLICATES;
$REAL max_uncertainty;
$REAL GMFP,GE,COHFAC,RAYCOR;
CHARACTER*60 medium_name;

"---------------------------------------------------------------------------"
"STEP 1:  USER-OVERRIDE-OF-EGSnrc-MACROS                                    "
"---------------------------------------------------------------------------"
REPLACE {$MXMED} WITH {1}   "only 1 medium in the problem(default 10)"
REPLACE {$MXREG} WITH {3}   "only 3 geometric regions (default 2000)"
REPLACE {$MXSTACK} WITH {50}"less than 50 particles on stack at once"
REPLACE {$MXENER} WITH {200}"max number of energies available"

$REAL avxphoto($MXENER),avxcomp($MXENER),avxrayl($MXENER),
      avxpair($MXENER),avmutot($MXENER),avxcompint($MXENER),
      sxphoto($MXENER),sxcomp($MXENER),sxrayl($MXENER),
      sxpair($MXENER),smutot($MXENER),sxcompint($MXENER),
      psxphoto($MXENER),psxcomp($MXENER),psxcompint($MXENER),
      psxrayl($MXENER),psxpair($MXENER),
      psmutot($MXENER);
```

```
" Used to calculate correct GMFP. Fadi"
REPLACE {$RAYLEIGH-CORRECTION;} WITH {
     ;IF(IRAYLR(2).EQ.1) [$EVALUATE COHFAC USING COHE(GLE);
    GMFP=GMFP*COHFAC];}

"Define a common to pass information to the geometry routine HOWFAR"
REPLACE {;COMIN/GEOM/;} WITH {;COMMON/GEOM/ZBOUND,ZBOUNDINPUT;
                               $REAL ZBOUND,ZBOUNDINPUT;}

"Define a common for scoring in AUSGAB"
REPLACE {;COMIN/SCORE/;} WITH {
   ;COMMON/SCORE/COUNT,NPHOTO,NCOMP,NRAYL,NPAIR,NSLAB,NAFTER,NTOOMANY,
    NCOMPINT,NOCOMP,EPHOT($MXENER),NCASEINPUT,NE;
   real*8 NPHOTO,NCOMP,COUNT,NRAYL,NPAIR,NSLAB,NAFTER,
    NTOOMANY,NCOMPINT,NOCOMP;
   $REAL EPHOT,NCASEINPUT;
   $INTEGER NE;}

REPLACE {$CALL-HOWNEAR(#);} WITH {
   ;CALL HOWNEAR({P1},X(NP),Y(NP),Z(NP),IRL);}

;COMIN/BOUNDS,EPCONT,GEOM,MEDIA,MISC,EDGE,
       SCORE,STACK,THRESH,USEFUL,COMPTON-DATA,PHOTIN/;
"       the above expands into a series of COMMON statements"

%E   "xsection.mortran"
"-------------------------------------------------------------------------"
"STEP 2 PRE-HATCH-CALL-INITIALIZATION                                     "
"-------------------------------------------------------------------------"

nmed = 1;   "use just one medium"
dunit = 1;  "i.e. we work in cm"

DO k=1,nmed [
  OUTPUT k; (/' Input name of medium ',I3,':',$);
  INPUT medium_name; (A);
  DO l=1,24 [ media(l,1) = medium_name(1:1); ]
]

/MED(1),MED(3)/=0;MED(2)=1; "regions 1 and 3 are vacuum, region 2 is
medium"
MEDIUM=MED(2);" MEDIUM is used in GMFP calculations. Fadi"

LOOP [
  OUTPUT; (/' Atomic relaxations on (1) or off (0)? ',$);
  INPUT iedgfl(1); (I5);
] UNTIL ( iedgfl(1) = 1 | iedgfl(1) = 0 );
"Now set iedgfl for all regions to the value input by the user"
DO i=1,$MXREG [ iedgfl(i) = iedgfl(1); ]

LOOP [
  OUTPUT; (/' Binding effects for Compton scattering on (1) or off (0)?
',$);
  INPUT ibcmp(1); (I5);
] UNTIL ( ibcmp(1) = 1 | ibcmp(1) = 0 );
"Now set ibcmp for all regions to the value input by the user"
DO i=1,$MXREG [ ibcmp(i) = ibcmp(1); ]
```

```
ECUT(2)=0.512;"   terminate electron histories at 0.512 MeV in the slab"
PCUT(2)=0.001;"   terminate   photon histories at 0.001 MeV in the slab"
IRAYLR(2)=1;"     turn on Rayleigh scattering in the slab "
"NOTE, above three parameters need to be set for all regions in which "
"there is particle transport - just region 2 in this case              "

"-----------------------------------------------------------------------"
"STEP 3   HATCH-CALL                                                    "
"-----------------------------------------------------------------------"

;OUTPUT;(/'   Start  PHOTXsection'//' Call  HATCH  to  get  cross-section
data'/);
CALL HATCH;"    pick up cross section data for medium"
"               data file must be assigned to unit 12"

;OUTPUT AE(1)-0.511, AP(1);
(/' Knock-on electrons can be created and any electron followed down to'
  /T40,F8.3,' MeV kinetic energy'/
' Brem photons can be created and any photon followed down to      '
  /T40,F8.3,' MeV ');"NOTE, AE values can over-ride ECUT values"

"-----------------------------------------------------------------------"
"STEP 4  INITIALIZATION-FOR-HOWFAR and HOWNEAR                          "
"-----------------------------------------------------------------------"

"This step is taken care of in STEP 7 through GMFP, Fadi.               "

"-----------------------------------------------------------------------"
"STEP 5  INITIALIZATION-FOR-AUSGAB                                      "
"-----------------------------------------------------------------------"

"  We want to set flags in AUSGAB every time a Rayleigh or Compton    "
"  or Photoelectric or Pair interaction occurs. Set the flags in IAUSFL
"
"   (COMIN EPCONT) to signal the  EGS system to make the appropriate
calls "

/IAUSFL(18),IAUSFL(19),IAUSFL(20),IAUSFL(24),IAUSFL(16)/=1;

"-----------------------------------------------------------------------"
"STEP 6   DETERMINATION-OF-INICIDENT-PARTICLE-PARAMETERS                "
"-----------------------------------------------------------------------"
" define initial variables for photon beam incident                     "
" perpendicular to the slab                                             "

mrho=rho(1);
write(6,*) ' Rho [g/cm3] of medium: ',mrho;
```

```
%E   "xsection.mortran"
"-------------------------------------------------------------------------"
"STEP 7   SHOWER-CALL                                                     "
"-------------------------------------------------------------------------"

OUTPUT;(/' Enter maximum uncertainty sought: ',$)
INPUT max_uncertainty;(F10.0);

OUTPUT;(/' Enter number of histories to be used: ',$)
INPUT NCASEINPUT;(F10.0);

;
OUTPUT;(/' Number of energies to calculate for: ',$);
INPUT n_energies;(I3);

IF (n_energies.gt.$MXENER) [
   write(6,*) 'too many energies';
   stop;]

DO l=1,n_energies [
 OUTPUT;(/' Enter energy in MeV: ',$);
 INPUT EPHOT(l);(F10.3)
]

open(unit=99,status='NEW');
write(99,'(A,A21,A,F5.3,A,//A,4X,A,6x,A,4X,A,4X,A,6X,A,
   3X,A,6X,A,7X,A,6X,A,6X,A)')
 ' Photon cross-sections in ',medium_name,' with PCUT=',PCUT(2),' MeV',
 ' MeV','PhotoE','s_photo','Compton','s_comp','Rayleigh','s_rayl',
 'Pair','s_pair','Total','s_tot';

"---------------Start of Energy Loop-------------------"
" cross-sections are calculated for a list of energies "
"------------------------------------------------------"

DO NE=1,n_energies [
   ECUT(2)=EPHOT(NE)+RM;   "  no  electron  transport  in  the  medium
"
   IRAYLR(2)=1;
   MEDIUM=MED(2);
   OUTPUT EPHOT(NE)*1000,medium_name,PCUT(2);
   (//' For',F8.1,' keV photons in ',A17,' with PCUT=',F5.3,' MeV'/);
```

```
"-------------------------------------------------------------------------"
" Here I define slab thickness through gamma mean free path (GMFP).      "
" This allows for automatic and optimal, or so I hope, slab thickness    "
" at any photon energy. Fadi                                             "
"-------------------------------------------------------------------------"

   GE= EPHOT(NE);" GE= gamma energy, used by GMFP"
   GLE=LOG(GE);" GLE is natural log of GE, used by GMFP"
   OUTPUT GLE;(' GLE=',F15.6);
   $SET INTERVAL GLE,GE;
   GMFP= 1.0;
"   $RAYLEIGH-CORRECTION; because IRAYLR=1, Fadi"
"   OUTPUT COHFAC;(' COHFAC= ',F15.6);
"   OUTPUT GMFP;(' GMFP avant = ',F15.6);
"   RAYCOR=GMFP;
   $EVALUATE GMFP USING GMFP(GLE); "--GAMMA MEAN FREE PATH IN CM"
"   $RAYLEIGH-CORRECTION;
   OUTPUT GMFP;(' GMFP= ',F15.6,' cm');
   ZBOUND= GMFP/4;
   OUTPUT ZBOUND;(' Slab thickness is: ',F8.6,' cm'/);

LOOP[  "----- % uncertainty loop ------"

   NCASE=NCASEINPUT/30;  "initiate the shower NCASE times"
   OUTPUT NCASE;(' NCASE per batch= ', I10);

   OUTPUT;('********* Cross-sections in cm2/g *****************');
   OUTPUT;(' BATCH #',3X,'Photoelectric',3x,'Compton',5X,'Rayleigh',6X,
   'Pair',10X,'Total');

   DO J=1,30 [

  "----------------setting incident particle parameters----------------"
      IQIN=0;"                incident photons"
      EIN= EPHOT(NE);"        Photon energy"
      /XIN,YIN,ZIN/=0.0;"     incident at origin"
      /UIN,VIN/=0.0;WIN=1.0;" moving along z axis"
      IRIN=1;"                starts in region 1"
      WTIN=1.0;"            weight = 1 since no variance reduction used"

   "----------------setting counting parameters to zero----------------"
      /NCOMP,NPHOTO,NRAYL,NPAIR,NCOMPINT,NOCOMP/=0.0;
      /COUNT,NSLAB,NAFTER,NTOOMANY/=0.0;
      LATCHI=0;
      /xphoto(j),xcomp(j),xrayl(j),xpair(j),mutot(j),xcompint(j)/=0.0;
      /BRPHOTO,BRCOMP,BRCOMPINT,BRRAYL,BRPAIR/=0.0;
      /NCROSS,NCROSSINT,NDUPLICATES/=0.0;
      /NNORATIO,MU,MUTOT(j)/=0.0;

      DO                          I=1,NCASE                          [CALL
SHOWER(IQIN,EIN,XIN,YIN,ZIN,UIN,VIN,WIN,IRIN,WTIN);]
```

```
"-------------------------------------------------------------------------"
"STEP 8   OUTPUT-OF-RESULTS                                               "
"-------------------------------------------------------------------------"

      NNORATIO = FLOAT(NCASE)/COUNT;   "normalize to photon number"
      MU=LOG(NNoRATIO)/ZBOUND;"   mu in cm-1"
      MUTOT(j)=MU/MRHO;"  mu in cm2/g, i.e. the total cross section"
      NCOMPINT=NCOMP-NOCOMP;

      " Branching ratios for the different interactions "
      BRPHOTO = NPHOTO/(NCOMPINT+NPHOTO+NRAYL+NPAIR);
      BRCOMP = NCOMP/(NCOMP+NPHOTO+NRAYL+NPAIR);
      BRCOMPINT = NCOMPINT/(NCOMPINT+NPHOTO+NRAYL+NPAIR);
      BRRAYL = NRAYL/(NCOMPINT+NPHOTO+NRAYL+NPAIR);
      BRPAIR = NPAIR/(NCOMPINT+NPHOTO+NRAYL+NPAIR);
      BRTOT = BRPHOTO+BRCOMP+BRRAYL+BRPAIR;
      BRTOTINT = BRPHOTO+BRCOMPINT+BRRAYL+BRPAIR;

      NCROSS=NPHOTO+NCOMP+NRAYL+NPAIR;
      NCROSSINT=NPHOTO+NCOMPINT+NRAYL+NPAIR;
      NDUPLICATES=NCASE-NCROSSINT-COUNT;

      " Cross-sections for the different interactions "
      XPHOTO(j) = MUTOT(j)*BRPHOTO;
      XCOMP(j) = MUTOT(j)*BRCOMP;
      XRAYL(j) = MUTOT(j)*BRRAYL;
      XPAIR(j) = MUTOT(j)*BRPAIR;
      XCOMPINT(j) = MUTOT(j)*BRCOMPINT;

OUTPUT NCASE,Count,nphoto,nphoto/ncase,count/ncase;
('  No                  Nthrough               Nphoto              nphoto/No
Nthrough/No'/
  ,I7,'       ',F8.1,'      ',F8.1,'      ',F10.6,'      ',F10.6)

      OUTPUT J,XPHOTO(j),XCOMP(j),XRAYL(j),XPAIR(j),MUTOT(j);
      (3X,I3,5X,E10.5,5X,E10.5,3X,E10.5,3X,E10.5,3X,E10.5,3X);
   ]

   /avxphoto(NE),avxcomp(NE),avxrayl(NE)/=0.0;
   /avxpair(NE),avmutot(NE),avxcompint(NE)/=0.0;

   DO I=1,30 [
      avxphoto(NE) = avxphoto(NE) + xphoto(i);
      avxcomp(NE) = avxcomp(NE) + xcomp(i);
      avxcompint(NE) = avxcompint(NE) + xcompint(i);
      avxrayl(NE) = avxrayl(NE) + xrayl(i);
      avxpair(NE) = avxpair(NE) + xpair(i);
      avmutot(NE) = avmutot(NE) + mutot(i);
   ]

   avxphoto(NE)=avxphoto(NE)/30.0;
   avxcomp(NE)=avxcomp(NE)/30.0;
   avxcompint(NE)=avxcompint(NE)/30.0;
   avxrayl(NE)=avxrayl(NE)/30.0;
   avxpair(NE)=avxpair(NE)/30.0;
   avmutot(NE)=avmutot(NE)/30.0;
```

```
/sxphoto(NE),sxcomp(NE),sxrayl(NE),sxpair(NE),smutot(NE),sxcompint(NE)/=
0.0;

   DO I=1,30 [
      sxphoto(NE) = sxphoto(NE) + (avxphoto(NE) - xphoto(i))**2;
      sxcomp(NE) = sxcomp(NE) + (avxcomp(NE) - xcomp(i))**2;
      sxcompint(NE) = sxcompint(NE) + (avxcompint(NE) - xcompint(i))**2;
      sxrayl(NE) = sxrayl(NE) + (avxrayl(NE) - xrayl(i))**2;
      sxpair(NE) = sxpair(NE) + (avxpair(NE) - xpair(i))**2;
      smutot(NE) = smutot(NE) + (avmutot(NE) - mutot(i))**2;
   ]

   sxphoto(NE) = sqrt(sxphoto(NE)/30.0/29.0);
   sxcomp(NE) = sqrt(sxcomp(NE)/30.0/29.0);
   sxcompint(NE) = sqrt(sxcompint(NE)/30.0/29.0);
   sxrayl(NE) = sqrt(sxrayl(NE)/30.0/29.0);
   sxpair(NE) = sqrt(sxpair(NE)/30.0/29.0);
   smutot(NE) = sqrt(smutot(NE)/30.0/29.0);

   /psxphoto(NE), psxcomp(NE),psxcompint(NE),psxrayl(NE)/=0.0;
   /psxpair(NE),psmutot(NE)/=0.0;

   psxphoto(NE) = 100*sxphoto(NE)/avxphoto(NE);
   psxcomp(NE) = 100*sxcomp(NE)/avxcomp(NE);
   psxcompint(NE) = 100*sxcompint(NE)/avxcompint(NE);
   psxrayl(NE) = 100*sxrayl(NE)/avxrayl(NE);
   psxpair(NE) = 100*sxpair(NE)/avxpair(NE);
   psmutot(NE) = 100*smutot(NE)/avmutot(NE);


   IF psxphoto(NE).gt.max_uncertainty[
      NCASEINPUT=NCASEINPUT*(psxphoto(NE)*1.10/max_uncertainty)**2;
      OUTPUT psxphoto(NE);
      (/' Photoelectric uncertainty %:',E10.5);
      ]
   ELSE[NCASEINPUT=1000000;EXIT;]

   OUTPUT NCASEINPUT;
   (/'Total # of histories of next iteration= ',E10.5,/);

]"-------------end of % loop-----------"

   OUTPUT EIN*1000,medium_name,PCUT(2),avxphoto(NE),sxphoto(NE),
          "avxcomp(NE),sxcomp(NE),"
          avxcompint(NE),sxcompint(NE),
          avxrayl(NE),sxrayl(NE),avxpair(NE),sxpair(NE),avmutot(NE),
          smutot(NE),
          psxphoto(NE),psxcomp(NE),psxrayl(NE),psxpair(NE),psmutot(NE);
   (//' For',F10.1,' keV photons in ',A17,' with PCUT=',F5.3,' MeV'//
   '****************      Final      Cross-sections      in      cm2/g
**********************'/
   '
PhotoE',3x,'s_photo',3X,'Compton',2X,'s_comp',4X,'Rayleigh',1X,'s_rayl'
   ,4X,'Pair',5X,'s_pair',4X,'Total',4X,'s_tot'/
   1X,F8.6,1X,F8.6,2X,F8.6,1X,F8.6,2X,F8.6,1X,F8.6,2X,F8.6,1X,F8.6,
   2X,F8.6,1X,F8.6/
```

```
   10X,F8.6,'%',10X,F8.6,'%',10X,F8.6,'%',10X,F8.6,'%',10X,F8.6,'%'//)

write(99,'(1X,F5.3,2X,E10.5,1X,E10.5,2X,E10.5,1X,E10.5,2X,E10.5,1X,E10.5
,2X,
               E10.5,1X,E10.5,2X,E10.5,1X,E10.5)')
     EPHOT(NE),avxphoto(NE),sxphoto(NE),avxcompint(NE),sxcompint(NE),
           "avxcomp(NE),sxcomp(NE),"
            avxrayl(NE),sxrayl(NE),avxpair(NE),sxpair(NE),avmutot(NE),
            smutot(NE);

] "-- end of energy loop --"
;

 OUTPUT medium_name,PCUT(2);
 (//' Photon cross-sections in ',A17,' with PCUT=',F5.3,' MeV'//
 '***************** Final Cross-sections in cm2/g *********************'/
 ' MeV',4X,'PhotoE',3x,'s_photo',3X,'Compton',2X,'s_comp',4X,'Rayleigh',
   1X,'s_rayl',4X,'Pair',5X,'s_pair',4X,'Total',4X,'s_tot'/);

 DO NE=1,n_energies [
    OUTPUT
EPHOT(NE),avxphoto(NE),psxphoto(NE),"avxcomp(NE),psxcomp(NE),"
            avxcompint(NE),psxcompint(NE),
            avxrayl(NE),psxrayl(NE),avxpair(NE),psxpair(NE),avmutot(NE),
            psmutot(NE);

(1X,F5.3,2X,F8.6,1X,F7.4,'%',2X,F8.6,1X,F7.4,'%',2X,F8.6,1X,F7.4,'%',
     2X,F8.6,1X,F7.4,'%',2X,F8.6,1X,F7.4,'%');
 ]
;
 OUTPUT medium_name,PCUT(2);
 (//' Photon cross-sections in ',A17,' with PCUT=',F5.3,' MeV'//
 '***************** Final Cross-sections in cm2/g *********************'/
 ' MeV',4X,'PhotoE',6x,'s_photo',4X,'Compton',4X,'s_comp',6X,'Rayleigh',
   3X,'s_rayl',6X,'Pair',7X,'s_pair',6X,'Total',6X,'s_tot'/);

 DO NE=1,n_energies [
    OUTPUT EPHOT(NE),avxphoto(NE),sxphoto(NE),"avxcomp(NE),sxcomp(NE),"
            avxcompint(NE),sxcompint(NE),
            avxrayl(NE),sxrayl(NE),avxpair(NE),sxpair(NE),avmutot(NE),
            smutot(NE);
     (1X,F5.3,2X,E10.5,1X,E10.5,2X,E10.5,1X,E10.5,2X,E10.5,1X,E10.5,2X,
      E10.5,1X,E10.5,2X,E10.5,1X,E10.5);
 ]
;

 OUTPUT;(/' Completed execution of PHOTXsection'/' Have a nice day'/);

STOP;END;"end of xsection main routine"
```

```
%E   "xsection.mortran"
"*************************************************************************"
"                                                                         "
SUBROUTINE AUSGAB(IARG);
"                                                                         "
" In AUSGAB for xsection we both set flags whenever there is             "
" a scattering event and then count histories when they have come        "
" through the slab , according to what kind of scattering they have     "
" undergone.                                                            "
" The logic is as follows                                               "
" set FLAG1 if a compton event occurs                                   "
" set FLAG2 if a Rayleigh event occurs                                  "
" The FLAGS are the units and thousands digits in the parameter LATCH   "
"                                                                       "
" When a history is terminated, increment various counters according    "
" to whether no flags are set - i.e. its a primary, FLAG2 is set,       "
" i.e. it has Rayleigh scattered or FLAG1 is set and FLAG2 is not set   "
" i.e. only  compton scattering has occured.                            "
"                                                                       "
" First a few macros are defined to make the logic simpler to read and  "
" therefore verify                                                      "
"                                                                       "
"*************************************************************************"
$IMPLICIT-NONE;
$INTEGER IARG;

REPLACE {$SET-FLAG1;} WITH {NCOMP=NCOMP+1;}
REPLACE {$SET-FLAG2;} WITH {NPHOTO=NPHOTO+1;NSLAB=NSLAB+1;LATCH(NP)=1;}
REPLACE {$SET-FLAG3;} WITH {NRAYL=NRAYL+1;NSLAB=NSLAB+1;LATCH(NP)=1;}
REPLACE {$SET-FLAG4;} WITH {NPAIR=NPAIR+1;NSLAB=NSLAB+1;LATCH(NP)=1;}


;COMIN/SCORE,STACK,EPCONT/; "we use IR(NP) from STACK"

"   first set flags when scattering events occur - IAUSFL was set "
"   in step 5 of main to ensure AUSGAB was called at these points "

IF(IR(NP)=2)[
   IF (LATCH(NP)=0)[ "if it's a primary particle"
       IF(E(NP).NE.EPHOT(NE))[ LATCH(NP)=1;IDISC=1;]
       IF(IARG=17) [ "a compton is about to occur" $SET-FLAG1;]

       IF(IARG=18) [ "return from compton call"
            IF(NPold=NP)[ "compton int. did not occur" NOCOMP=NOCOMP+1;]
            ELSE[ "compton int. has occured" NSLAB=NSLAB+1;
                    LATCH(NP)=1;IDISC=1;]
       ]

       ELSEIF(IARG=23)[ "a rayleigh is about to occur" IDISC=1;$SET-
FLAG3;]
       ELSEIF(IARG=19)[ "a photoeffect is about to occur" IDISC=1;$SET-
FLAG2;]
       ELSEIF(IARG=15)[ "a pair is about to occur" IDISC=1;$SET-FLAG4;]
   ]
   ELSEIF (LATCH(NP)~=0)[ IDISC=1;]
]
```

```
IF (IR(NP)=3)["particle has passed through the slab"
   IF  (LATCH(NP)=0)[COUNT=COUNT+1.;IDISC=1;"counting the primaries in
3"]
   ELSEIF    (LATCH(NP)~=0)[NTOOMANY=NTOOMANY+1;IDISC=1;]"counting    the
secondaries in region 3"
   ]

RETURN;
END;"end of AUSGAB"


%E   "xsection.mortran"
"*****************************************************************"
"                                                                 "
SUBROUTINE HOWFAR;
"                                                                 "
"    HOWFAR for a semi-infinite homogeneous medium slab           "
"*****************************************************************"
$IMPLICIT-NONE;
$REAL TVAL;
COMIN/STACK,EPCONT,GEOM,SCORE/;

IF(IR(NP) = 3)[NAFTER=NAFTER+1;IDISC=1;
               RETURN;"terminate this history: it is past the slab"]

ELSEIF(IR(NP) = 2)["we are in the Ta slab - check the geometry"

   IF(W(NP) > 0.0)[
   "going forward -consider first since it is most frequent"
   TVAL=(ZBOUND-Z(NP))/W(NP); "tval is dist to "
   "                          boundary in this direction"
   IF(TVAL > USTEP)[RETURN;"CAN TAKE CURRENTLY REQUESTED STEP"]
   ELSE[USTEP=TVAL;IRNEW=3;RETURN;]
   ]"END OF W(NP)>0 CASE"

   ELSEIF(W(NP) <  0.0)["going back towards origin"
      TVAL = -Z(NP)/W(NP);     "distance to plane at origin"
      IF(TVAL > USTEP)[RETURN; "can take currently requested step"]
      ELSE[USTEP=TVAL;IRNEW=1;RETURN;]
   ]"end W(NP)<0 case"

   ELSEIF(W(NP) = 0.0)["CANNOT HIT BOUNDARY"RETURN;]
]"END OF REGION 2 CASE"

ELSEIF(IR(NP) = 1)["in regon with source"
   IF(W(NP) > 0.0)["THIS MUST BE A SOURCE PARTICLE ON Z=0 BOUNDARY"
      USTEP=0.0;IRNEW=2;RETURN;
   ]
   ELSE[ "must be a reflected particle - discard it" IDISC=1;RETURN;]
]"end region 1 case"

RETURN;
END;"end of subroutine HOWFAR"
```

```
%E  "xsection.mortran"
"*************************************************************************"
"                                                                         "
SUBROUTINE HOWNEAR(tperp, x, y, z, irl);
"                                                                         "
" The following is a general specification of HOWNEAR                     "
"   Given a particle at (x,y,z) in region irl, HOWNEAR answers the        "
"   question, What is the distance to the closest boundary?               "
"                                                                         "
"  In general this can be a complex subroutine.                           "
"  Note that this subroutine must be linked to $CALL-HOWNEAR(#)           "
"                                                                         "
"*************************************************************************"
$IMPLICIT-NONE;
$REAL tperp, x,y,z;
$INTEGER irl;

;COMIN/GEOM/;
"       COMMON GEOM contains ZBOUND"
IF(irl = 3) [OUTPUT;('Called HOWNEAR in region 3'); RETURN;]

ELSEIF(irl = 2)["We are in the medium plate - check the geometry"
    tperp = min(z, (ZBOUND - z) );
]

ELSEIF(irl = 1)[OUTPUT;('Called HOWNEAR in region 1'); RETURN;]

END;"end of subroutine hownear"
```

4. PHOTXsection input file template

```
CICRU512XCOM_2MeV              ,medium_name
1                              ,atomic_relaxation
1                              ,bound_Compton
0.2                            ,max_uncertainty_allowed
10000000                       ,histories
14                             ,n_energies
0.010                          ,photon_energy
0.020
0.030
0.040
0.050
0.060
0.070
0.080
0.090
0.100
0.150
0.200
0.250
0.300

/------------- end of input file --------------\
```

4.1. Input file explanations

Medium_name is the name of the name of the medium present in the slab. The *atomic_relaxation* and *bound_Compton* switches can be turned on (1) or off (0). The *max_uncertainty_allowed* variable tells PHOTXsection what uncertainty the user is aiming for (0.2 = 0,2%). The *histories* variable gives the initial number of histories to be used by PHOTXsection. The variable *n_energies* tells the code that a list of energies containing a number *n_energies* of energies will be inputted. The subsequent lines give the list of energies (one per line) for which PHOTXsection will calculate attenuation coefficients.

Appendix B

PTB X-ray spectra

This appendix contains graphs of the different PTB kilovoltage X-ray spectra used in this study as listed in Table 1 (Chapter 6). Each graph includes the name of the spectrum and its mean photon energy as an insert.

1. PTB X-ray spectra

1.1. A-series spectra

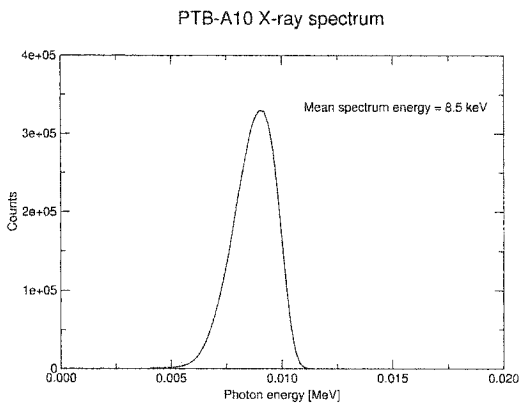

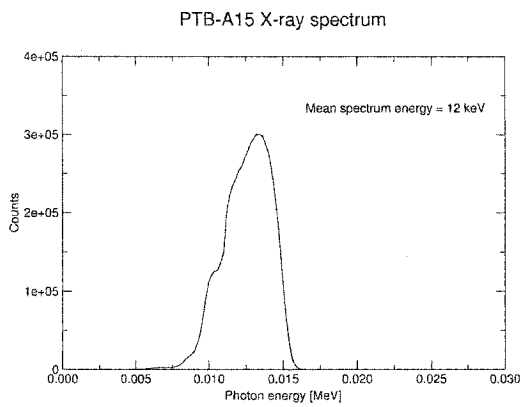

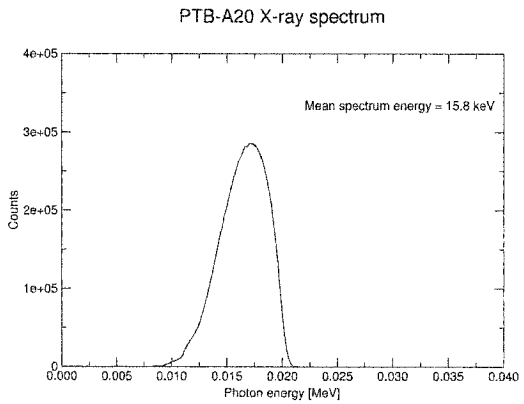

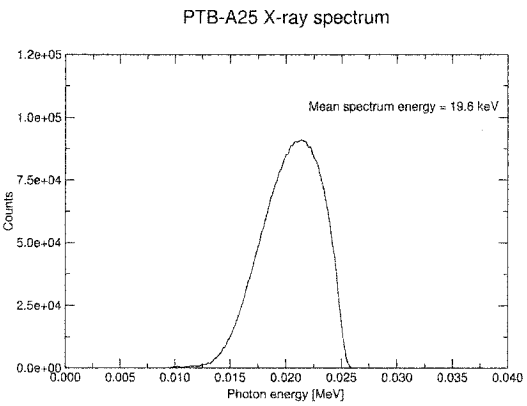

PTB-A30 X-ray spectrum

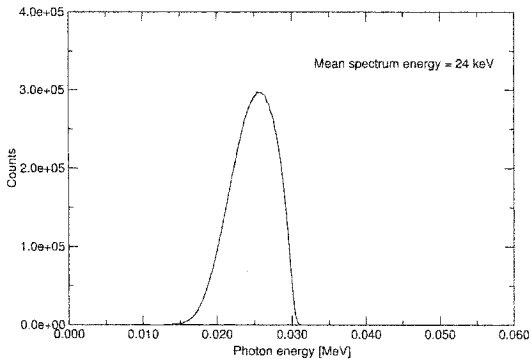

PTB-A40 X-ray spectrum

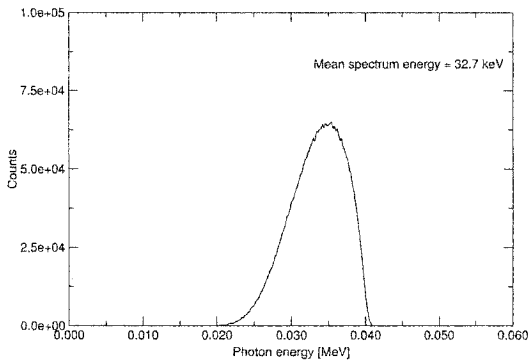

PTB-A50 X-ray spectrum

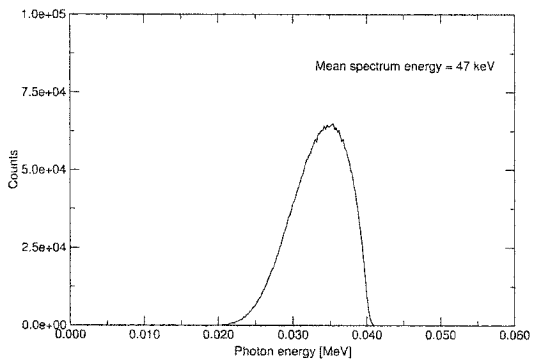

PTB-A60 X-ray spectrum

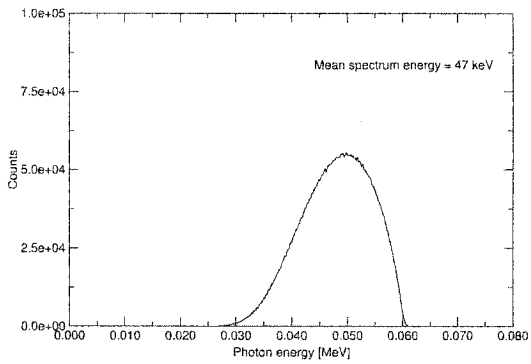

1.2. B-series spectra

PTB-B40 X-ray spectrum

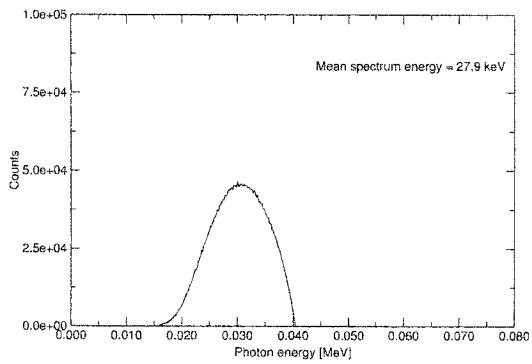

PTB-B60 X-ray spectrum

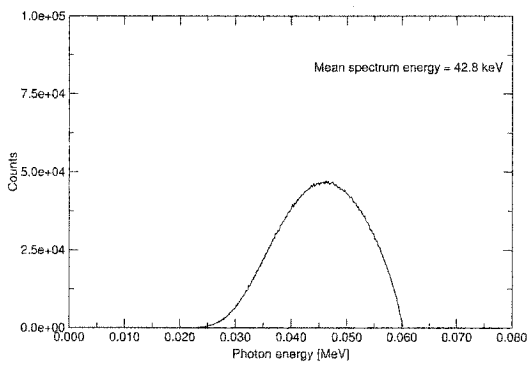

PTB-B80 X-ray spectrum

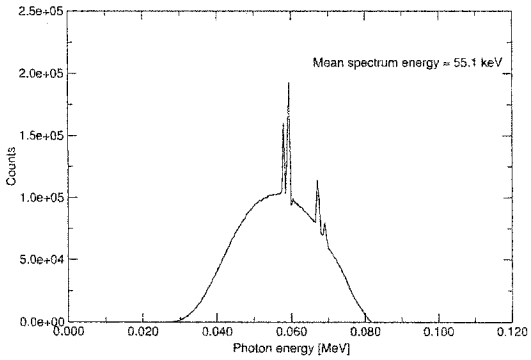

PTB-B110 X-ray spectrum

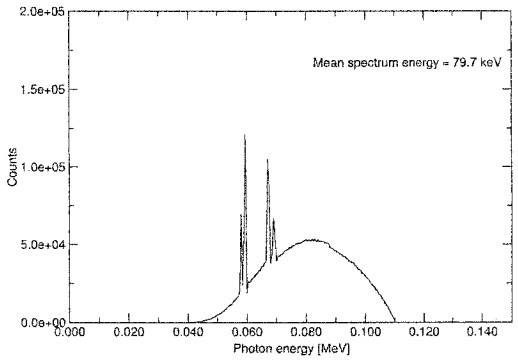

PTB-B150 X-ray spectrum

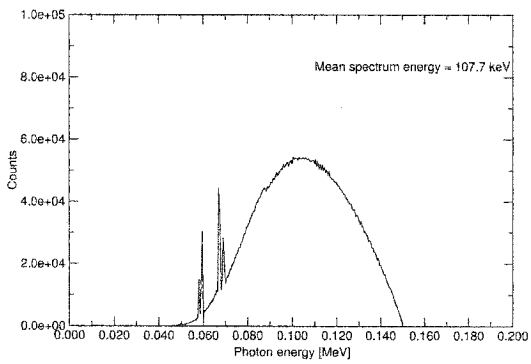

PTB-B200 X-ray spectrum

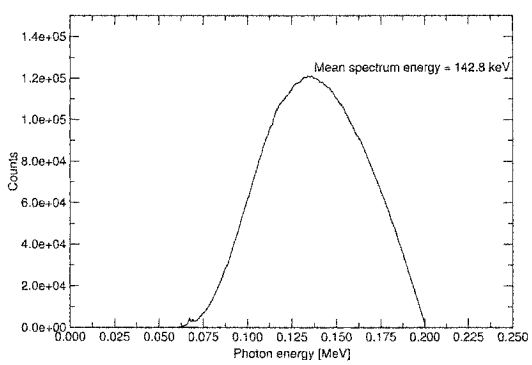

PTB-B250 X-ray spectrum

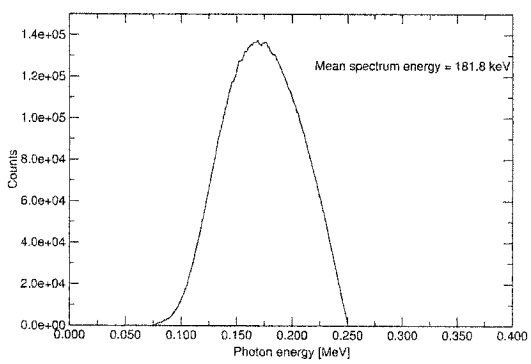

PTB-B300 X-ray spectrum